

THESTS

3 1293 10065 7992

LIBRARY
Michigan State
University



# OVERDUE FINES: 25¢ per day per item

#### RETURNING LIBRARY MATERIALS:

Place in book return to remove charge from circulation records

# DETERMINATION OF THE COULOMB CORRECTION AND ISOVECTOR TERMS OF THE NUCLEON-NUCLEUS OPTICAL MODEL POTENTIAL FROM NEUTRON ELASTIC SCATTERING AT 30.3 AND 40 MEV

BY

Raymond Peter DeVito

#### A DISSERTATION

Submitted to

Michigan State University
in partial fulfillment of the requirements
for the degree of

DOCTOR OF PHILOSOPHY

Department of Physics

#### ABSTRACT

OF THE NUCLEON-NUCLEUS OPTICAL MODEL POTENTIAL FROM

NEUTRON ELASTIC SCATTERING AT 30.3 AND 40 MEV

BY

# Raymond Peter DeVito

Elastic scattering angular distributions  $(15^{\circ} \le \theta_{lab} \le 130^{\circ})$  for scattering of 30.3 and 40 MeV neutrons from targets of  $^{12}$ C,  $^{28}$ Si,  $^{32}$ S,  $^{40}$ Ca and  $^{208}$ Pb have been measured using the MSU beam swinger Time of Flight system. The  $^{7}$ Li(p,n) $^{7}$ Be reaction served as a neutron source. Overall energy resolution was typically 500-1000 keV FWHM. Relative and normalization errors are both typically <3%. Optical model potentials are deduced by comparing the observed cross sections with optical model predictions smeared to account for the effects of multiple scattering, attenuation, and finite angular resolution.

Comparison of deduced neutron potentials with existing proton potentials at the same incident energy for N=Z nuclei yields directly the Coulomb correction term. The magnitude and energy dependence of the isovector part of the nucleon-nucleus potential is deduced by comparison of neutron and proton potentials for N≠Z nuclei. Comparisons are made both in terms of volume integrals and potentials for fixed geometry.

#### **ACKNOWLEDGEMENTS**

I would like to thank my thesis advisor, Professor

Sam Austin, for suggesting this project. His encouragement is deeply appreciated. His advice and assistance
were indispensable to the completion of this work.

I thank my wife, Mary Lynn for her patience and encouragement and for typing this manuscript.

I gratefully acknowledge the assistance of Dr. Ulrich Berg, Dr. Wim Sterrenburg and Dr. Larry Young in taking the data.

For their assistance in construction of experimental apparatus and in running the cyclotron, I thank the cyclotron technical staff. In particular I thank Dr. Peter Miller, Mr. Norval Mercer and Mr. Bill Harder.

I would also like to thank the National Science Foundation and Michigan State University for their financial support.

# TABLE OF CONTENTS

LIS	r of	TABLES	v							
LIST	r of	FIGURES	vi							
ı.	INT	NTRODUCTION								
	A.	Nucleon-Nucleus Optical Model	1							
	B. Phenomenological Potentials									
	C.	Present Work								
II.	NEUTRON SCATTERING APPARATUS									
	A.	Beam and Beam Transport	14							
	В.	Scattering Apparatus  1. Beam Swinger  2. Neutron Production  3. Scattering Targets	15 15 18 25							
	c.	Detectors 1. Neutron Detectors 2. Monitor Detector	31 31 33							
	D.	Electronics 1. Time of Flight Signal 2. Pulse Shape Discrimination Signal 3. Light Pulsers	34 34 35 35							
III.	DATA	A ACQUISITION PROCEDURE								
	A.	Computer and Spectrum Accumulation	40							
	В.	Time of Flight Spectrum	41							
	c.	Normalization Procedure	42							
	D.	Background	45							
IV.	DATA	A REDUCTION								
	A.	Peak Areas	47							
	в.	Cross Sections	47							

	C.	Neutron Detection Efficiency	50				
	D.	Experimental Errors	50				
v.	OPT	CICAL MODEL ANALYSIS					
	A.	Optical Model Parameter Search Code	55				
	В.	Center of Mass Cross Sections	58				
	c.	Parameter Search Procedure	61				
	D.	Volume Integrals					
	E.	Coulomb Correction Term	70				
	F.	Isovector Term					
	G.	Imaginary Potential	84				
VI.	SUM	<b>IMA</b> RY	91				
APPENDIX							
LIST OF REFERENCES 1							

# LIST OF TABLES

1.	30 MeV Run Parameters	21
2.	40 MeV Run Parameters	22
3.	Scattering Sample Dimensions	27
4.	Target Nuclei	28
5.	Experimental Errors	54
6.	$\chi^2/N$ of Global Parameter Sets	62
7.	Optical Model Parameters E <sub>n</sub> =30.3 MeV	66
8.	Optical Model Parameters E <sub>n</sub> =40.0 MeV	67
9.	Volume Integrals	69
LO.	J/A for Protons and Neutrons on Calcium Enucleon =30.3 MeV	77
11.	J/A for Protons and Neutrons on Calcium E <sub>nucleon</sub> =40.0 MeV	78
L2.	J/A for Protons and Neutrons on Lead Enucleon =30.3 MeV	85
L3.	J/A for Protons and Neutrons on Lead $E_{nucleon} = 40.0 \text{ MeV}$	86
L4.	Tabulated Data	126

# LIST OF FIGURES

1.	Experimental Area of MSU Cyclotron Laboratory	16
2.	Navy Magnet and Beam Swinger	17
3.	Lithium Target Chamber	23
4.	(n,n) Apparatus	24
5.	<sup>7</sup> Li(p,n) near 0 <sup>0</sup>	26
6.	Vault Electronics	37
7.	Data Room Electronics	38
8.	Neutron-Gamma Pulse Shape Discrimination Spectrum	39
9.	TOF Spectra 40 MeV, Si, 60° Target In, Target Out, Subtracted	43
10.	Monitor Spectrum 40 MeV Lithium Target In, Li Target Out	44
11.	Neutron Detector Efficiency	51
12.	Flow Chart for GIBSCAT	5 <b>7</b>
13.	Search Procedure	63
14.	Energy Dependence of Calcium Volume Integrals, Best Fit Values	73
15.	Energy Dependence of Calcium Real Potential Strength with Fixed Geometry	74
16.	Energy Dependence of Lead Real Potential Strength with Fixed Geometry	81
17.	Energy Dependence of Lead Volume Integrals, Best Fit Values	83
18.	Energy Dependence of Calcium Imaginary Potential Strength with Fixed Geometry	89
19.	Energy Dependence of Lead Imaginary Potential Strength with Fixed Geometry	90
20.	TOF Spectrum 40°, S, 30 MeV	95

21.	TOF Spectrum 40°, Si, 30 MeV	96
22.	TOF Spectrum 40°, Ca, 30 MeV	97
23.	TOF Spectrum 42°, Pb, 30 MeV	98
24.	TOF Spectrum 40°, S, 40 MeV	99
25.	TOF Spectrum 40°, Ca, 40 MeV	100
26.	TOF Spectrum 42°, Pb, 40 MeV	101
27.	Monitor TOF Spectrum 30 MeV	102
28.	TOF Spectrum of Neutron Source, <sup>7</sup> Li(p,n) at 0°	103
29.	Laboratory Cross Section, <sup>28</sup> Si, 30 MeV	104
30.	Laboratory Cross Section, 32S, 30 MeV	105
31.	Laboratory Cross Section, 40Ca, 30 MeV	106
32.	Laboratory Cross Section, 208Pb, 30 MeV	107
33.	Laboratory Cross Section, <sup>12</sup> C, 40 MeV	108
34.	Laboratory Cross Section, <sup>28</sup> Si, 40 MeV	109
35.	Laboratory Cross Section, <sup>32</sup> S, 40 MeV	110
36.	Laboratory Cross Section, 40 Ca, 40 MeV	111
37.	Laboratory Cross Section, 208Pb, 40 MeV	112
38.	Center of Mass Cross Section, <sup>28</sup> Si, 30 MeV	113
39.	Center of Mass Cross Section, 32S, 30 MeV	114
40.	Center of Mass Cross Section, Best Fit $^{40}$ Ca, 30 MeV	115
41.	Center of Mass Cross Section, Fixed Geometry $^{40}\mathrm{Ca}$ , 30 MeV	116
42.	Center of Mass Cross Section, Best Fit 208 <sub>Pb</sub> , 30 MeV	117
43.	Center of Mass Cross Section, Fixed Geometry 208 <sub>Pb</sub> . 30 MeV	118

44.	Center of	Mass	Cross	Section,	<sup>12</sup> C, 40 MeV	119
45.	Center of	Mass	Cross	Section,	<sup>28</sup> Si, 40 MeV	120
46.	Center of	Mass	Cross	Section,	<sup>32</sup> s, 40 MeV	121
47.	Center of 40 MeV	Mass	Cross	Section,	Best Fit <sup>40</sup> Ca,	122
48.	Center of <sup>40</sup> Ca, 40 l		Cross	Section,	Fixed Geometry	123
49.	Center of 40 MeV	Mass	Cross	Section,	Best Fit 208Pb,	124
50.	Center of 208 <sub>Pb</sub> , 40		Cross	Section,	Fixed Geometry	125

#### I. Introduction

## A. Nuclear Optical Model

The nucleon-nucleus interaction is a complex many body process that can not be solved exactly. In order to begin to understand the physics of the atomic nucleus, approximations and simplifications must be employed. As more and more information and experience is gained these simplifications and approximations will possibly lead us toward a more accurate and complete knowledge of the nucleus. It is the aim of this present work to add to that experience.

Nucleons incident upon an atomic nucleus may be scattered elastically, leaving the nucleus unchanged except for some translational energy, or may react with the nucleus, altering its internal structure in some way. Thus the incident wave packet may be scattered or absorbed. In optics, light incident on some medium may undergo refraction and absorption. This process for light is described by the complex index of refraction of the medium. The actual microscopic interaction of the incident photons with the material is very complicated. In describing the nucleon scattering, we can think of the incident particle being scattered by a complex potential well. The imaginary part would account for all nonelastic reactions. By analogy to the case in optics we call this potential the Optical Model Potential (OMP).

This idea was applied semi-classically by Fernbach et al. They treated the scattering and absorption (Fe49) in 1949. of 90 MeV neutrons by a range of nuclei. The elastic and inelastic total cross sections could be accounted for by their process. Later, in 1952, LeLevier and Saxon (Le52) did a full quantum mechanical calculation for 17 MeV protons on Aluminum. In 1954 Feshbach (Fe54) showed that the energy averaged variation of low energy neutron cross sections with atomic weight could be represented by a complex neutron-nucleus potential. With the advent of electronic computers, wave functions could easily be calculated from the Schroedinger equation for arbitrary potentials. As the precision of the data increased the model was refined to a point where it can account for differential and reaction cross sections as well as polarization to a high degree of accuracy.

The study of the Nuclear Optical Model involves two categories of work. One is phenomenological, whereby one empirically determines the parameters of an OMP by fitting experimental elastic scattering data. The other is theoretical in nature and involves computing the effective potential from considerations of the many-body problem (Je77, Br77).

Aside from its intrinsic interest the study of the OMP is motivated by the important role it plays in the interpretation of many nuclear reactions (Au70). The calculated incident and outgoing waves in a reaction undergo reflections and absorptions due to the potential determined by elastic scattering.

Consider the system comprised of A+1 nucleons (Pe74), where there is a nucleon incident on a target nucleus, described by a wave function  $\Psi$ . The wave function for a state i of the target nucleus is described by  $\phi_i(r_1,\ldots,r_A)$  with corresponding energy  $\varepsilon_i$ . The variables  $r_k$  indicate position, spin and isospin of the nucleons. We expand using the complete orthonormal set  $\phi_i$  with amplitudes  $\chi_i$ ,

$$\Psi = \sum_{i} \phi_{i}(r_{1}, \dots, r_{A}) \chi_{i}(r_{0}). \qquad (I-1)$$

The Schroedinger equation that describes this system is

$$\mathbf{H}\Psi = \mathbf{E}\Psi \tag{I-2}$$

where

$$\mathcal{H} = H_{A}(r_{1}, \dots, r_{A}) + T_{0} + V(r_{0}, r_{1}, \dots, r_{A}).$$
 (I-3)

 $H_A$  is the Hamiltonian for the A particles of the target nucleus,  $T_0$  is the kinetic energy for the incident nucleon while V is the potential energy of that nucleon in the field of the target nucleus. We note that  $\phi$  satisfies

$$H_{A}\phi_{i} = \varepsilon_{i}\phi_{i} . \qquad (I-4)$$

Thus using the orthonormal properties of the set  $\phi_{\dot{\mathbf{1}}}$  we obtain a set of coupled equations for the amplitudes

$$(T_0 + V_{ii} + \epsilon_i - E) \chi_i = -\sum_{i \neq j} V_{ij} \chi_j$$
 (I-5)

where

$$v_{ij} = (\phi_i, V\phi_j),$$

$$v_{ij} = v_{ji}^*.$$
(1-6)

We define the matrices

$$\underline{X} = \begin{pmatrix} \chi_1 \\ \chi_2 \\ \chi_3 \\ \vdots \end{pmatrix}$$
 (I-7)

and

$$\underline{\mathbf{v}}_0 = (\mathbf{v}_{01}, \mathbf{v}_{02}, \cdots)$$
.

The matrix operator  $\underline{H}$  is defined by

$$\underline{H}_{ij} = T_0 \delta_{ij} + V_{ij} + \varepsilon_i \delta_{ij}$$
 i,  $j \neq 0$  . (I-8)

In matrix notation equation I-5 becomes

$$(T_0 + V_{00} - E)\chi_0 = -\underline{V}_0\underline{X}$$
  
 $(\underline{H} - E)\underline{X} = -\underline{V}_0^{\dagger}$  (1-9)

Solving formally we find

$$\underline{X} = \frac{1}{E^{(+)} - \underline{H}} \underline{V}_0^{\dagger} \qquad (I-10)$$

where  $E^{(+)}$ =E+i $\eta$  with  $\eta$ ++0. Within the Green's function in specifies that only outgoing waves are present in  $\chi_i$  for i>0. Using equation I-10 in equation I-9 we obtain the one body Schroedinger equation

$$\left(\begin{array}{cc} T_0^{+V} & \frac{1}{E^{(+)} - \underline{H}} & \underline{V}_0^{+} - E \end{array}\right) \chi_0^{=0} \quad . \tag{I-11}$$

We therefore obtain the "generalized Optical Model Potential"

$$V = V_{00} + \underline{V}_{0} \frac{1}{E^{(+)}-H} \underline{V}_{0}^{\dagger}$$
 (I-12)

The potential V is not the optical model potential, it is the exact potential operator for elastic scattering. The OMP is the simple effective potential that replaces the true potential operator V. With an appropriate choice of replacement for V the Schroedinger equation becomes more simply solvable. The new wave function is not exactly  $\chi_0$  since the replacement potential does not exactly represent V. In elastic scattering the details of the wavefunction are not important, but rather the asympototic behavior of  $\chi_0$  is important, i.e. the potentials must be phase equivalent.

The choice of an OMP is guided by intuitive physical ideas, but must incorporate some of the properties that can be deduced from equation I-12. The potential operator V is not Hermitian, due to the imaginary term in the Green's function. The second term in I-12 is responsible for the imaginary part of the OMP, but it also contributes to the real part. This term is nonlocal and explicitly energy dependent. The spacial nonlocality in this term arises physically by removal of flux from the entrance channel due to  $\underline{V}_0^{\dagger}$ . This flux can propagate in reaction channels, then some flux will reappear in the entrance channel at some other point by the  $\underline{V}_0$  interaction. The term  $V_{00}$  also yields a nonlocal potential due to explicit exchange forces in the

two body interaction and from antisymmetrization. The spatial nonlocality of the generalized OMP appears as a momentum dependence if a local replacement potential is used. It is not possible to distinguish between the explicit energy dependence and the energy dependence due to the spatial nonlocality of the potential operator when  $\checkmark$  is replaced by a local potential.

Recent theoretical analyses have yielded good calculations of the basic properties of the nucleon-nucleus OMP (Je77, Ma79, Br77, Br78) starting from the nucleon-nucleon interaction. Within the framework of Brueckner's theory a density dependent potential is derived from a two nucleon interaction e.g. Reid hard core (Re68) or Hamada-Johnston (Ha62). The simple radial shape of the phenomenological OMP suggests that it is mainly dependent on the matter density of the nucleus. Thus it is feasible to study the OMP in a finite nucleus by studying nuclear matter at various densities and applying a Local Density Approximation (LDA). A simple LDA, one that assumes that the OMP at a given location in the nucleus is equal to the same value as in a uniform medium with the same local density, is able to yield semi-quantitative conclusions on the global properties of the OMP: depth, energy dependence, non-locality, small components and main features of the form factors. Good agreement between volume integrals calculated using a simple LDA and those observed experimentally is achieved. However root-mean-square (rms) radii are in general too small. An improved LDA,

which takes into account the finite range of the effective interaction yields improved agreement between calculated and phenomenological rms radii without affecting volume integrals.

Theoretical OMP are able to render properties of the observed average OMP with an accuracy of about 10%. Agreement between the calculated and observed imaginary potentials is worse, about 30%, due to the inability of nuclear matter based theories to take into account shell effects.

# B. Phenomenological Optical Model Potentials

There is no apriori reason to believe that the generalized OMP admits any equivalent simple local potentials of the type typically used to analyze data. But, from the great body of data analyzed over the past 25 years there exists a simple potential which describes very well most of the features of elastic scattering of nucleons and other projectiles. It is the purpose of OM analysis to determine the various terms of this potential and to study their behavior as a function of energy and target nucleus.

A typical phenomenological OMP is a local multi-parameter potential usually written as

$$-U(E,r) = V(E,r) + iW(E,r)$$
 (I-13)

In the present analysis, the real part of the potential is written as

as  

$$V(E,r) = V_{C}(r) + V(E) f(x_{R}) - V_{SO}(\vec{\sigma} \cdot \vec{l}) \left(\frac{\hbar}{m_{\pi}c}\right)^{2} \frac{1}{r} \frac{d}{dr} f(x_{SO})$$
(I-14)

The form factor  $f(x_i)$  is taken to be a Woods-Saxon shape defined as

$$f(x_i) = (1+e^{x_i})^{-1}$$
;  $x_i = (r-r_iA^{1/3})/a_i$ .

This shape is chosen for convenience and because nuclear matter densities are closely described by such forms (Ne70).

The first term of equation I-14,  $V_{_{\hbox{\scriptsize C}}}(r)$ , is the Coulomb potential due to a uniformly charged sphere of radius  $R_{_{\hbox{\scriptsize C}}}$ ,

$$V_{c} = \begin{cases} (Zze^{2}/2R_{c}) \{3-r^{2}/R_{c}^{2}\} & \text{for } r \leq R_{c} \\ (Zze^{2}/r) & \text{for } r \geq R_{c} \end{cases}$$
(I-15)

where  $R_c = r_c A^{1/3}$ , Z is the target charge and z is the projectile charge. This term vanishes for the neutron potential since the neutron charge is zero.

The last term in equation I-14 is the spin-orbit potential. The explicit Thomas form of the potential was chosen by analogy to the atomic spin-orbit potential and has been substantiated experimentally.

The central real term from equation I-14 can be written, following the suggestion of Lane (La62), as

$$V(E) = V_0(E) + \frac{4}{A}V_1(E) \overrightarrow{t} \cdot \overrightarrow{T} + \Delta V_c$$
 (I-16)

Here  $V_0(E)$  is the isoscalar part of the potential and  $V_1(E)$  the isovector part;  $\vec{t}$  and  $\vec{T}$  are the isospins of the incident nucleon and target, respectively. The isovector interaction  $\vec{t} \cdot \vec{T}$ , splits the central part of the potential into diagonal terms which are responsible for proton and neutron scattering

and a non-diagonal term that mediates the (p,n) or (n,p) quasi-elastic scattering. For nucleon scattering we can evaluate  $\vec{t} \cdot \vec{T}$  to give

$$V(E) = V_0(E) \pm \varepsilon V_1(E) + \Delta V_C . \qquad (I-17)$$

Where  $\varepsilon=(N-Z)/A$  represents the nuclear asymmetry. The + sign applies for protons and the - sign for neutrons. The isovector strength  $V_1(E)$  comes about because of the properties of nucleon-nucleon interactions,  $V^{\mathrm{pp}}=V^{\mathrm{nn}}\neq V^{\mathrm{pn}}$ . This effect comes about because the Pauli exclusion principle restricts states between like nucleons but not states between unlike nucleons. The term  $\Delta V_{\mathrm{C}}$  is the Coulomb correction term, first suggested by Lane (La57), and is usually paramerized by

$$\Delta V_c = \beta z Z/A^{1/3}$$
.

In addition to the Coulomb potential (equation I-15) the charge of the nucleus has the effect of reducing the mean kinetic energy of incident charged particles interacting with the nucleus. This effect is accounted for by adding to the proton potential the Coulomb correction term.

The imaginary part of the OMP is not expected to have the same shape as the real part. Absorption takes place throughout the nucleus, but especially at low energies various factors such as the Pauli principle and surface excitations should enhance surface contributions. As the

incident energy increases, both these effects should decrease causing the absorption to be distributed more uniformly throughout the nucleus. OM analysis confirms this. In the present analysis a Woods-Saxon form factor together with a derivative Woods-Saxon form factor are used. As energy increases the strength of the surface potential decreases and that of the volume absorption increases. We therefore write the imaginary part of the phenomenological potential as

$$W(E,r) = W_V(E) f(x_V) - 4W_D(E) \frac{d}{dx_D} f(x_D)$$
 (I-18)

Just as for the real part, the imaginary part can be parameterized by Coulomb correction, isovector and spin-orbit terms. Jeukenne et al. (Je77) have calculated the imaginary Coulomb correction and isovector terms starting from the Brueckner-Hartree-Fock approximation and Reid's hard core nucleon-nucleon interaction. The imaginary spin-orbit term is calculated by Brieva and Rook (Br78) to be substantially smaller than the real spin-orbit term ( $W_{so}/V_{so}$ -0.05 for 20 MeV nucleons) and is set equal to zero in the present analysis.

# C. Present Work

A large collection of precise proton scattering data already exists in the literature. There is a lack however, of precision neutron data, expecially for incident neutron energies greater than 15 MeV. The extensive neutron scattering program of Rapaport et al. at Ohio University has con-

tributed good neutron data at 11, 20 and 26 MeV for a wide range of nuclei (Ra77, Fe77, Ra78). Most of the best proton scattering data are for incident proton energies greater than 26 MeV, notably at 30.3 MeV (Ri64) and at 40 MeV (B166). The isovector strength of the nucleonnucleus OMP can be extracted by comparison of proton and neutron potentials. There are two ways to compare these potentials, at the same energies or at energies shifted to account for the Coulomb correction. The former method yields the Coulomb correction from comparison of N=Z nuclei while the latter method requires either prior knowledge of the Coulomb correction or the measurement of angular distributions over a range of energies. The Coulomb correction is not known very precisely and due to the amount of cyclotron time required to complete one angular distribution, measuring several angular distributions for each nucleus was impracti-Thus we have measured neutron elastic scattering angular distributions at incident energies of 30.3 and 40 MeV on targets of  $^{12}$ C (40 MeV only),  $^{28}$ Si,  $^{32}$ S,  $^{40}$ Ca,  $^{208}$ Pb, and <sup>209</sup>Bi. Comparison between N=Z nuclei yields the Coulomb correction term and then comparison between N≠Z nuclei yields the isovector term.

Since neutrons have no net charge and all particle accelerators use electromagnetic forces, no direct beam of monoenergetic neutrons exists. To produce a monoenergetic neutron flux at our scattering target a charge exchange reaction is used. A proton beam accelerated by the MSU cyclotron

strikes a target of <sup>7</sup>Li and the reaction <sup>7</sup>Li(p,n) <sup>7</sup>Be is used as the neutron source. This reaction is strongly forward peaked which reduces background. High energy neutrons are produced that are well separated in energy from neutrons produced by other reactions. To produce a neutron flux large enough to complete an angular distribution measurement in about 1-2 days an energy loss due to Li target thickness of about 500 keV was used.

To achieve a large enough counting rate large scattering samples (~l mole) of cylindrical geometry are used. Since the neutrons will not interact with the Coulomb field within the target, a large scattering sample could be tolerated.

To detect the scattered neutrons another nuclear interaction must take place in the form of (n,p) scattering within an organic scintillator. The energy of the neutron cannot be directly determined since directional information on the (n,p) scattering angle is not available. The neutron velocity can be determined however, by measuring its time-of-flight (TOF) over a fixed flight path. Once the velocity is known the energy can be calculated.

One advantage of the neutron scattering measurements compared to charged particle work is that absolute cross sections can be measured with little uncertainty. After measuring the sequence: source reaction-scattering-detection reaction, one can remove the scattering sample and look at  $0^{\circ}$  to measure the sequence: source reaction-detection reaction.

By comparison of these two measurements the majority of the uncertainty in the  $^{7}\text{Li}(p,n)$  cross section, Li target thickness, detector efficiency, neutron attenuation along the flight path and solid angle of the detector are removed.

The beam swinger built at MSU and used in these experiments simplified the shielding and detector positioning requirements. The incident proton beam is rotated to vary the scattering angle instead of moving the neutron detector. For long flight paths this is an important advantage.

## II. Neutron Scattering Apparatus

# A. Beam and Beam Transport

A beam of nearly monoenergetic neutrons is produced by bombarding a thin foil of metallic  $^7\text{Li}$ . The  $^7\text{Li}(p,n)^7\text{Be}$  (g.s.) and  $^7\text{Li}(p,n)^7\text{Be}(0.429 \text{ MeV})$  reactions at zero degrees are used to generate the neutron beam. The scattering target is located on the swinger axis thereby allowing neutron elastic scattering angular distributions to be measured by rotating the beam swinger.

The particle beams produced by the Michigan State University Cyclotron are very well suited for time-of-flight (TOF) experiments. The beam is sharply bunched in time, with a typical burst width of  $\approx 300 \, \mathrm{ps}$  and a burst interval between 50 and 67 ns depending upon particle energy. For the experiments described herein the cyclotron was used to produce 32 and 42 MeV proton beams. The energy resolution  $\Delta E/E$  of the cyclotron beam is  $< 10^{-3}$ ; compared to the overall energy resolution of this experiment, this energy spread is negligible.

After extraction from the cyclotron, the transport of the beam to the experimental area is controlled by a series of bending magnets, focusing magnets (quadrupoles) and position defining slits. The beam is defined spatially by slits in Boxes 1, 3 and 4 (see Figure 1). After being focused at slit 3 by a quadrupole doublet Q1 and Q2, the beam passes through slit 4 and undeflected through M3 into the neutron TOF beam line.

In vault 5 the beam is refocused at a point just before the Navy magnet by a quadrupole triplet located near door 5. Beam position is checked here by using a TV monitored scintillator. The beam is centered through the quads by requiring that there is only focusing and no net translation when the setting of Q7 and Q8 are changed.

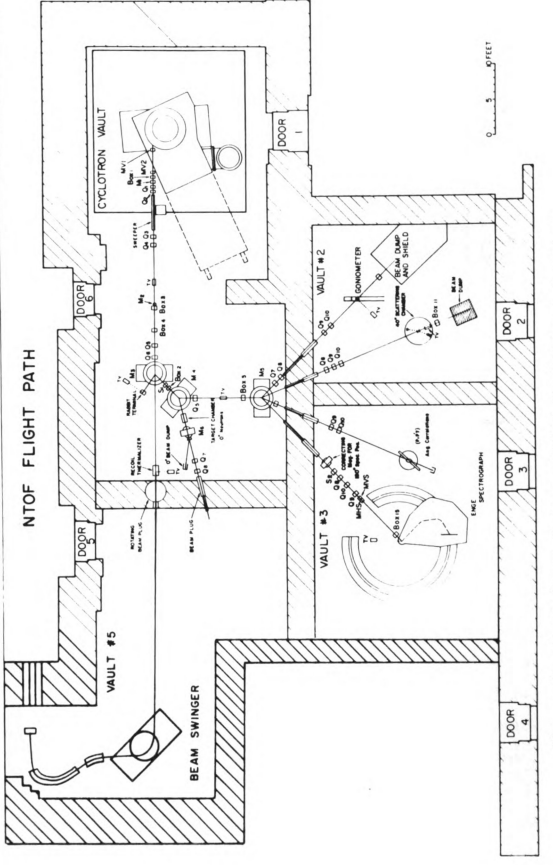
The layout of the beam swinger is shown in Figure 2. The beam is deflected through 90° by the Navy magnet prior to entering the swinger. In addition to the focus at the entrance to the Navy magnet, the system has a focus near the entrance to the swinger and at the target position.

### B. Scattering Apparatus

# Beam Swinger

The swinger consists of two magnets capable of rotating about the incident beam axis (Bh77). The beam is first deflected  $-45^{\circ}$  and then deflected  $+135^{\circ}$  with the net effect that the beam is perpendicular to its original direction.

The swinger magnets, of fully annealed 1010 steel, are of a H design with a bending radius of 76 cm. The poles are 10.2 cm wide with a 3.2 cm gap. A 36 minute taper on each pole tip makes the swinger magnets double focusing  $(n=\frac{1}{2})$ . The overall magnification of the swinger system is about one. The current carrying coils are flat pancakes, three to a pole, of 1.2 cm square hollow copper conductor wrapped in fiberglass and vacuum potted in epoxy. Current and power consumption at a field of 1.4 Tesla is 450 Amps



Experimental Area of MSU Cyclotron Laboratory Figure 1.

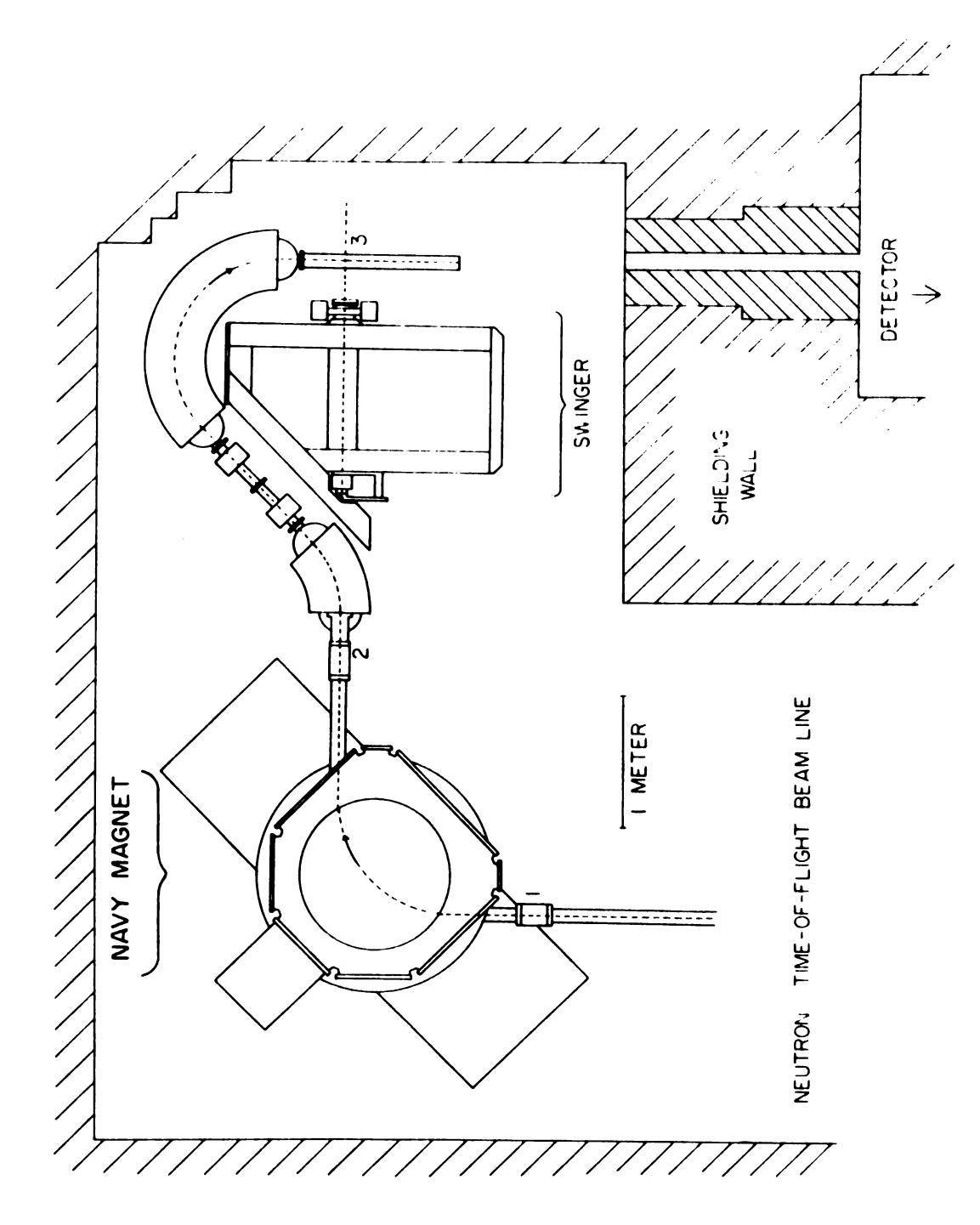


Figure 2. Navy Magnet and Beam Swinger

and 22 Kilowatts. An additional power supply was connected to the 135° magnet to balance the two swinger magnets.

The swinger's usable angular range was from  $0^{\circ}$  to  $160^{\circ}$  for the neutron scattering experiments. In general the angular distributions were measured out to  $130^{\circ}$ , beyond which point the cross sections become too small to measure in the available time.

The shielding walls of the swinger vault were stacked concrete blocks 1.8 meters thick. The wall, 2.15 meters from the scattering target, provides good isolation of the detectors from the high neutron and gamma-ray flux in the swinger vault. A hole along the target to the detector flight path allows transmission of the scattered neutrons. This hole is filled with steel bars and lead bricks except for an opening just sufficient to allow both detectors an unobstructed view of the scattering target. A 300 kg iron shadow bar is positioned so as to attenuate the direct flux of neutrons to the detector from the <sup>7</sup>Li(p,n) reaction.

#### 2. Neutron Production

To obtain a mean energy of 30.3 and 40.0 MeV for the neutron beam, proton beams of 32.2 and 41.9 MeV respectively were used. In practice proton beam energies were slightly different for each run on the cyclotron. The mean neutron energies, along with the spread due to production target thickness are presented in Table 1 for 30 MeV and Table 2 for 40.0 MeV. The effect on the cross sections of the energy variation and the energy spread due to the production target

thickness was estimated by OM calculation to be <0.1%.

The lithium targets used in the (p,n) reaction were made from high purity lithium enriched to 99.99% 7Li. The lithium was pressed into disks about 1 cm in diameter by a hydraulic press. The target thicknesses used in this experiment were 0.64 and 0.76 mm at 32 and 42 MeV proton energy respectively, corresponding to a total energy spread due to energy loss in the Li target of 500 keV. This energy spread had to be tolerated to obtain count rates sufficiently high to make the experiment practical. The contribution from the  $^{7}$ Li(p,n)  $^{7}$ Be(0.429 MeV) reaction was included in the neutron elastic scattering peak. The first excited state contribution was about 25% and 30% at 32 and 42 MeV proton energy respectively. The second excited state of <sup>7</sup>Be is at 4.57 MeV excitation, well removed from the high energy elastic peak. The neutron yield from three body final states (Q= -3.24 MeV) is measured to be very small in the energy range of interest (see Figure 28). The Li(p,n) Be (q.s.) reaction has a O value of -1.644 MeV.

Following the Li target is a 0.127 mm thick aluminum foil. The <sup>27</sup>Al(p,n) reaction has a Q value of -5.592 MeV, thus contributing no background at the elastic peak. This aluminum foil isolates the vacumn chamber from a water faraday cup, consisting of an aluminum chamber through which distilled water is constantly pumped. This provides cooling to the lithium target as well as a beam dump with

a large negative Q value (Q $_{\rm pn}$ =-16.2 MeV) for neutron production. The high energy neutron flux from the 0.2% of  $^{18}$ O (Q $_{\rm pn}$ =-2.4 MeV) and 0.04%  $^{17}$ O (Q $_{\rm pn}$ =-3.5 MeV) contributed negligibly to the measured spectra.

The neutron flux at the scattering target could be adjusted by varing the distance between the Li target and the scattering sample (see figures 3 and 4). This was done by changing the length of the plexiglass pipe that makes up part of the vacumn chamber. The Li target to scattering sample distance (d) could be set at 24.4, 18.4, or 11.0 cm. This range allowed beam intensities to vary by 1:1.76: 4.9. The largest practical distance was chosen for any given angular range since the closer is the neutron source to the scatterer, the larger is the angle subtended by the sample and thus the larger the finite angle correction to be made. The angular ranges are tabulated in Tables 1 and 2.

Two proton beam collimators were machined from graphite since  $^{12}\text{C}$  has a large negative Q value for neutron production  $(Q_{pn}=-18.1\text{ MeV})$ . The high energy neutron flux from the 1.11%  $^{13}\text{C}$   $(Q_{pn}=-3.0\text{ MeV})$  was neglible. Beam current on the collimators was monitored during the experiment and was usually negligable (<1 nA). In all cases the collimator current was kept to <0.1% of the target current.

The mean scattering geometry for the neutron scattering is determined by the position of the Li target, the position of the scattering sample and the position of the detector. The detector is never moved, the sample was repositioned

Table 1. 30 MeV Run Parameters

a) d=24.4 cm b) d=18.4 cm c) d=11.0 cm

does not include energy spread from production target £)

d) flux correction as defined in section IV-B

e) scattering sample to detector distance

Table 2. 40 MeV Run Parameters

Threshold Electron Energy (MeV)	7.14	9.52	7.14	9.52	7.14	9.52	7.14	9.52	7.30	7.14
(cm)	816	850	816	850	816	820	510	850	700	703
(d)	1.010	1.010	1.011	1.011	1.008	1.008	1.013 1.019 1.130	1.020	1.133	1.013 1.019 1.114
Angular Range (degrees)	a) 15-40 b) 40-65	a)15-40 c)60-130	a) 15-40 b) 40-65	a)15-40 c)60-130	a)15-40 b)40-65	a)15-40 c)60-130	a) 15-40 b) 40-70 c) 70-160	b) 45-60	c) 70-120	a)15-33 b)30-90 c)90-130
Detector Energy Resolution (KeV)	860	830	860	830	860	830	1400	830	1000	066
Energy Loss in Li target (KeV)	400	200	400	200	400	200	400	500	520	200
Neutron Energy (MeV)	40.24	40.37	40.24	40.37	40.24	40.37	40.24	40.37	40.28	39.95
Nuclide	$^{12}_{ m C}$	$^{12}_{ m c}$	28 <sub>S.i</sub>	28si	32 S	32 S	40 Ca	$^{40}$ Ca	40 <sub>Ca</sub>	$208_{ m Pb}$

a) 24.4 cm b) 18.4 cm c) 11.0 cm d) flux correction as defined in section IV-B

d) flux correction as defined in section IV-e) scattering sample to detector distance

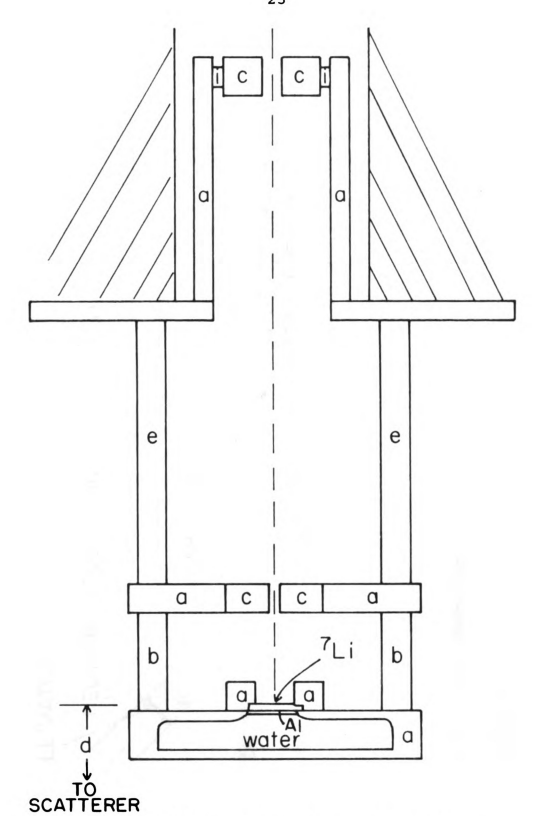


Figure 3. Lithium Target Chamber. a) aluminum b) plexiglass pipe c) graphite collimator e) interchangeable plexiglass pipe i) electrical insulator

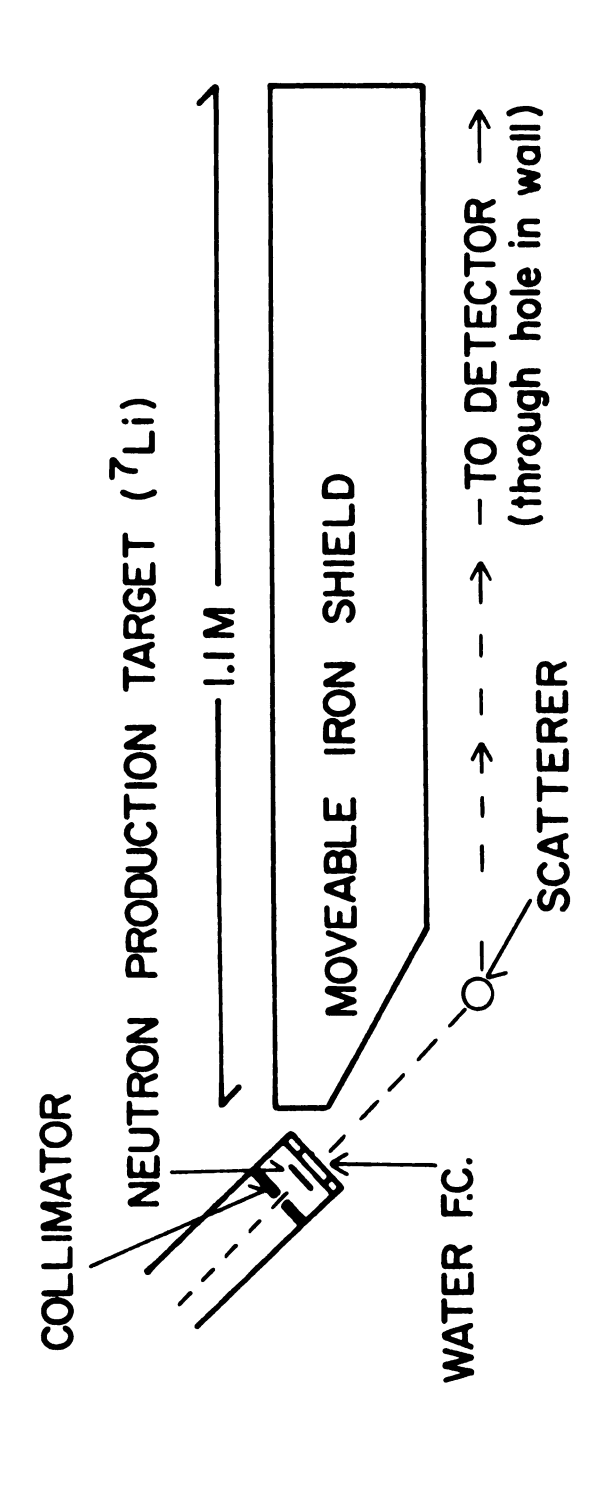


Figure 4. (n,n) Apparatus

to better than 1.0 mm and the Li target was rigidly held to the swinger. Thus the mean scattering angle was well known, and did not depend on the angle that the proton beam hit the Li target. The cross section for neutrons scattered in the direction of the target however does depend on the angle the proton beam hits the Li target. The  $^{7}$ Li(p,n) cross section is forward peaked with a slight flat region around  $0^{\circ}$ . The proton beam was collimated to  $\pm 2.50^{\circ}$  FW for C, Si, S and Ca and  $\pm 1.0^{\circ}$  FW for Pb. Figure 5 shows the angular distribution of  $^{7}$ Li(p,n)  $^{7}$ Be(g.s.+0.429 MeV) for scattering angles from  $0^{\circ}$  to  $15^{\circ}$ .

# 3. Scattering Targets

All scattering targets used were formed in solid right circular cylinders. The dimensions, mass, chemical purity and isotopic enrichment of these targets are listed in Table 3.

The best shape for each scattering target was determined by computer calculation of multiple scattering and finite angle effects. The sample must have a symmetry axis perpendicular to the beam direction. The multiple scattering effects are reduced as the target is elongated, but then the finite angle effects are increased. As the target is made more spherical finite angle effects are reduced but multiple scattering is increased. The best target shape was calculated for the various targets. Small variations about the best shape caused little increase in finite geometry effects. The actual target shape was not necessarily the calculated best shape but depended upon what materials were available.

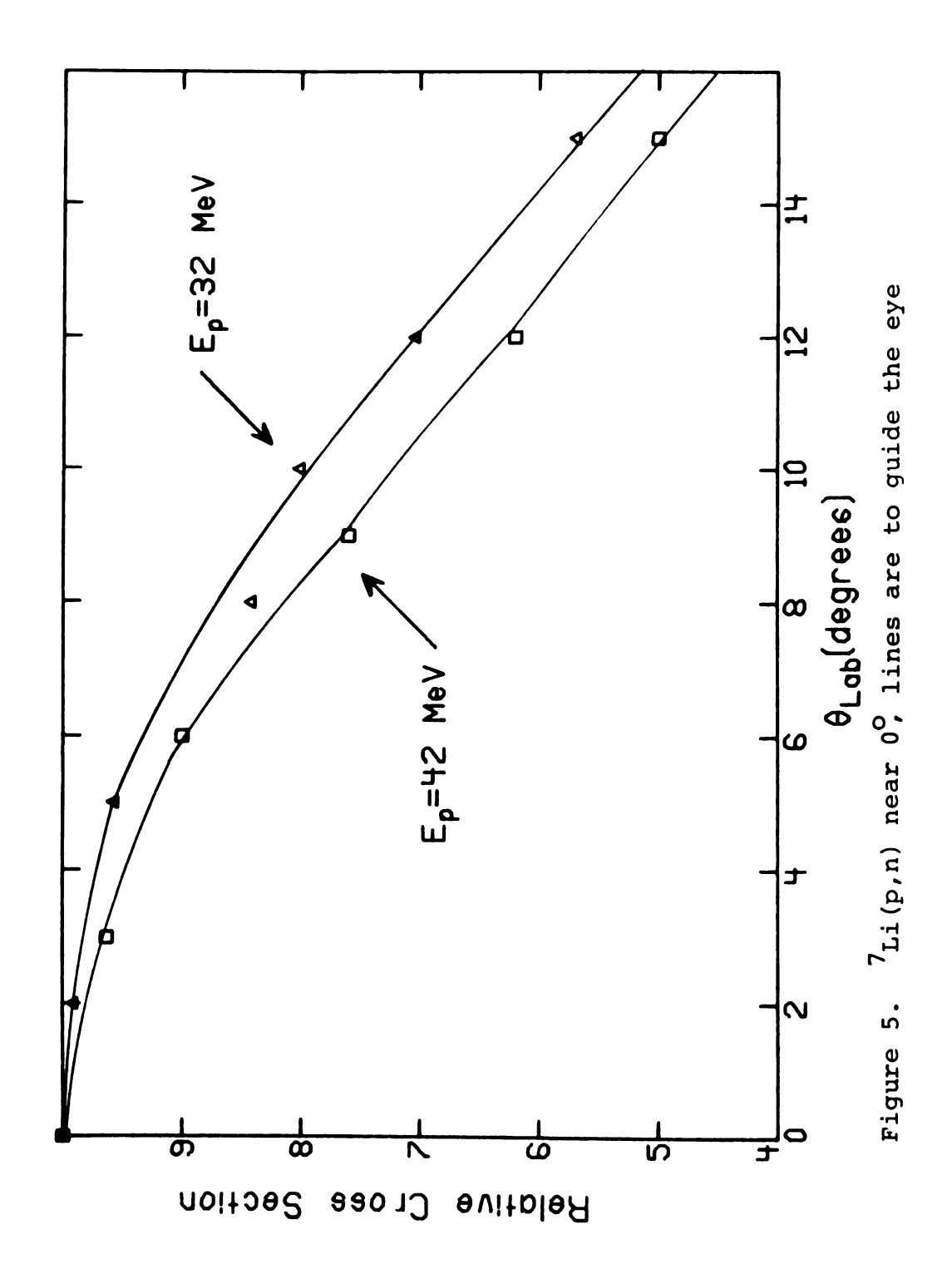


Table 3. Scattering Sample Dimensions

Sample	Dimensions Height x diam. (cm)	Chemica Purity (%)	Mass	Isotopic Enrichment (%)
12 <sub>C</sub>	3.40 x 2.64	98.+	33.077	natural(98.89)
28 <sub>Si</sub>	3.69 x 2.36	99.+	37.777	natural(92.2)
28 <sub>Si</sub>	7.09 x 2.36	99.+	72.559	natural(92.2)
<sup>32</sup> s	2.86 x 3.17	99.9	42.417	natural(95.0)
40 <sub>Ca</sub>	4.36 x 1.90	98.0 (b)	18.697	natural(96.94)
40 <sub>Ca</sub>	4.80 x 2.30	98.0 (b)	27.200	natural(96.94)
208 <sub>Pb</sub>	3.90 x 2.40	99.7+	200.640	98.69 <sup>(a)</sup>

- a) Borrowed from Darrell Drake, Los Alamos Scientific Laboratory
- b) Includes oxygen impurity measured as described in text page 29.

Table 4. Target Nuclei

Nuclei	lst excit Energy(MeV)		2nd excited state (MeV)	Remarks
12 <sub>C</sub>	4.44	2 <sup>+</sup>	7.66	$\beta(2_1^+)=0.60^{(a)}$
28 <sub>Si</sub>	1.78	2+	4.62	$\beta(2_1^+)=0.40^{(a)}$
32 <sub>S</sub>	2.23	2+	3.78	$\beta(2_1^+)=0.37^{(a)}$
40 <sub>Ca</sub>	3.35	0+	3.74	≃spherical
208 <sub>Pb</sub>	2.61	3	3.20	≃spherical

a) reference (St65)

The <sup>208</sup>Pb target was prefabricated by Los Alamos to our specifications. The Si target was received as a cylinder of appropriate diameter and only needed to be cut by diamond saw to the desired length. The C and Ca targets were machined on a lathe from ingots.

The calcium targets were sealed inside thin aluminum cans as calcium is reactive in air. The cans were fabricated from 0.05 mm thick foil held together with epoxy. For each target can an identical empty can was fabricated from the same size and weight pieces of aluminum. The weight of the target can and the empty can were the same to <1%.

An estimate of the oxygen contamination in the calcium target was made by measuring the neutron scattering from the sample with sufficient energy resolution to separate the neutron groups elastically scattered from  $^{40}$ Ca and  $^{16}$ O at a few angles around  $70^{\circ}$ . An estimate of the cross section ratio combined with the ratio of scattered neutrons indicated the  $^{16}$ O contamination to be  $2\%\pm1\%$ .

The sulfur target fabrication was more difficult than the others. Molten sulfur was poured in layers into a pyrex beaker. The layers were thin enough so the solidification could be monitored to ensure no holes were being formed in the target. When the desired amount of material was solidified the glass was heated just enough to melt the outer surface of the sulfur target and then cooled. Best results were achieved with fast cooling in a water bath, with care taken to be sure no water splashed into the beaker. The

glass beaker usually had to be broken away from the sulfur target. Once the technique was mastered several targets were produced, all of which appeared to be of the same quality. All but two were then broken open and checked for voids. No voids were discovered. The target used in the experiment was broken open after the experiment was complete and no voids were discovered. The outer shell of sulfur was hard and did not rub off. Due to these farication procedures, the sulfur target was the only target where the diameter exceeded the height.

The scattering targets were all mounted with the symmetry axis along the swinger rotation axis. The targets rested on thin aluminum trays supported by thin stainless steel rods. The trays were made with the smallest amount of material that still gave rigid support. The rod, tray and target assembly was then supported from beneath by one of four rotatable arms of the target changer. These four arms allowed three targets to be mounted for one run. fourth position was taken by a blank target, i.e. a tray and rod only. A Geneva device was used to accurately rotate the target assembly thereby changing the scattering target. The targets were aligned by using a survey telescope and survey markings on the wall and swinger. Due to the magnification of the telescope, alignment with the survey markings could be done to within 1 mm. Accuracy of the survey markings was checked and found to be consistant with the swinger rotation axis. The Geneva device was rotated in

one direction only. The reproducability checked to within the accuracy of the survey scope.

#### C. Detectors

#### 1. Neutron detectors

Unlike charged particle detection, neutrons are not detected directly, but rather, the recoil of a charged particle is detected if the neutron undergoes an appropriate nuclear scattering within the detector. The charged recoil causes the detector material to scintillate and this light is detected by a photomultiplier.

We used two 12.7 cm diameter x 7.62 cm thick NE213 liquid organic scintillator detectors, produced by Nuclear Enterprises. These detectors each contain 965 cm<sup>3</sup> of scintillator. The liquid is encapsulated in a glass cylinder painted with white reflective paint. Each has a teflon expansion chamber to relieve pressure caused by temperature variations. The light is carried to the photo multiplier by a conical light pipe 7 cm thick, one end 12.7 cm diameter and the other 5.08 cm diameter. The light pipe is coupled to the scintillator and the photomultiplier by Dow Corning Optical Silicon grease.

Either a RCA 8575 or a RCA 8850 phototube was used in an Ortec 265 phototube base. These phototubes contain 12 dynodes and the base provides signals from the 9th dynode and the anode. The amplified signal from the 9th dynode provides a measure of the total light produced by an event.

The scintillator Ne213 was chosen because it allows one to distinguish between events caused by neutrons and gamma rays. This discrimination is possible because the recoils for neutrons are mostly protons while the recoils for gamma rays are electrons. The shape of the light pulse for protons and electrons is different and can be distinguished. This Pulse-Shape Discrimination (PSD) is very important in eliminating gamma ray background.

The photomultiplier assembly for each detector was wrapped in several layers of magnetic shielding. This magnetic shielding was necessary because fringe fields from the Superconducting Cyclotron magnet being built at MSU were sometimes present during experimental runs.

To have a continuous check on the gain of the detectors a pulsed light-emitting-dynode (LED) giving a constant number of photons was fed into the photomultiplier during data collection. The position of this LED peak thus gave an on-line gain stability check.

The detector and associated electronics provide a timing pulse with a finite uncertainty. The detector thickness provides a time spread due to the uncertainty in where the event took place in the detector. The transit time for the 7.62 cm thick detector is 0.9 ns for 40 MeV neutrons and 1.0 ns for 30 MeV neutrons. The energy uncertainty due to time uncertainty is given by the nonrelativistic equation

$$\Delta E = (.0277) E^{3/2} \underline{\Delta t}$$
 (II-1)

where E is in MeV,  $\Delta t$  is in nsec, and d is in meters.

The energy resolution for each run is tabulated in Table 1 and Table 2. The time resolution  $\Delta t$  for all runs was about 1 ns for  $\gamma$ -rays from the production target.

## 2. Monitor Detector

A detector is mounted rigidly to the swinger to monitor the neutron flux from the  $^{7}\text{Li}(p,n)$  reaction at a scattering angle ranging from  $21^{\circ}$  to  $24^{\circ}$  depending on production target to scattering target distance. A flight path of 140.0 cm provided sufficient energy resolution to separate the  $^{7}\text{Li}(p,n)$  (g.s.+0.429)  $^{7}\text{Be}$  neutrons from the neutrons produced by  $^{27}\text{Al}(p,n)$  and other background sources.

The detector consisted of a cylinder of NE102 plastic scintillator 2.54 cm diameter by 1.9 cm height coupled directly to a RCA 8575 phototube and Ortec 265 base by Dow Corning Optical grease. The detector was wrapped in several layers of magnetic shielding and then mounted inside a soft iron cylinder with 1.75 cm thick walls. Since this detector was rotated in the fringe field from the Navy magnet located 4 m away, extra magnetic shielding was necessary.

A stability check of the monitor detector gain was made by measuring the Compton edge for gamma rays from  $^{228}$ Th at several swinger angles with full current in the Navy magnet. The detector was stable to better than 1%.

Lead shielding 10.0 cm thick was placed between the detector and the source. The Pb attenuates gamma rays, especially those of low energy (<1 MeV) more than high energy

neutrons, thus reducing the overall count rate to a manageable level.

The anode signal was fed into a constant fraction discriminator (CFD) whose output was used for the timing signal (see Figure 6). The dynode signal was fed into a preamp and then to a Spectroscopy Amplifier. The NE102 does not produce PSD information therefore a Spectroscopy Amp was used for its convenience. The monitor detector also had an LED pulser fed directly to the phototube to monitor possible gain shifts.

Due to the mounting position of the monitor it had to be removed and repositioned on the opposite side of the swinger when the swinger was rotated through  $90^{\circ}$ .

#### D. Electronics

## 1. Time of Flight Signal

The anode of the photomultiplier produces a fast negative voltage pulse when a neutron event occurs in the scintillator. This pulse is fed into a CFD from which a fast negative pulse is produced that is timed from the point where the leading edge reaches 50% of the maximum pulse height (see Figure 6). This method provides minimal variation of triggering time for pulses covering a wide dynamic range. The negative output of the CFD was used to start a Time to Amplitude Converter (TAC) (see Figure 7). The stop signal originates from the zero crossing of the Cyclotron RF, which is detected by a Zero Crossing Discriminator. The TAC provides a voltage pulse whose height is proportional to the time between start and stop. Since we start with the event pulse and stop with

the cyclotron pulse we get a time spectra that gives a "normal" spectrum with increasing energy going from left to right.

# 2. Pulse Shape Discrimination Signal

The decay of the light pulse from electrons, protons or heavier charged particles is different in a way that allows us to distinguish these events. Proton (neutron) events have a longer decay time than electron (gamma) events.

A signal from the fast negative output of the CFD is delayed for about lusec either by a long length of cable or a Gate and Delay generator and then starts a TAC (see Figure 6). The double delay line(DDL) output from the amplifier is fed into a Timing Single Channel Analyser (TSCA) run in the zero crossing mode. A signal timed from the zero crossing is then sent to stop the TAC.

The zero crossing of the DDL output from neutron events will be delayed longer relative to that for electrons because of the longer decay time. A typical PSD spectrum is shown in Figure 8. A gate can be set around the neutron events so only neutron events are recorded in the TOF spectra. This PSD system is based on the technique of Alexander and Goulding (A161).

## 3. Light Pulsers

A temperature compensating current pump to drive an LED was built, based on the design by Hagen and Eklund (Ha76).

This LED pulser gave a stable source of photons to act as a gain drift monitor. By comparison with a monoenergetic gamma

ray source the LED light signal was found to drift <1% over a temperature range of  $\pm 10^{\circ}$  C from room temperature and over many hours. The LED was mounted on the current pump circuit board next to the thermistor that gives the device its temperature stability. A small light pipe consisting of a bundle of fiber optics was then used to transport the light to the photocathode. The light pipe of the neutron detector prevented direct access to the photocathode so the LED pulse was directed into the detector light pipe. This caused the signal to be greatly attenuated but it was still usable in the low light region of the spectra.

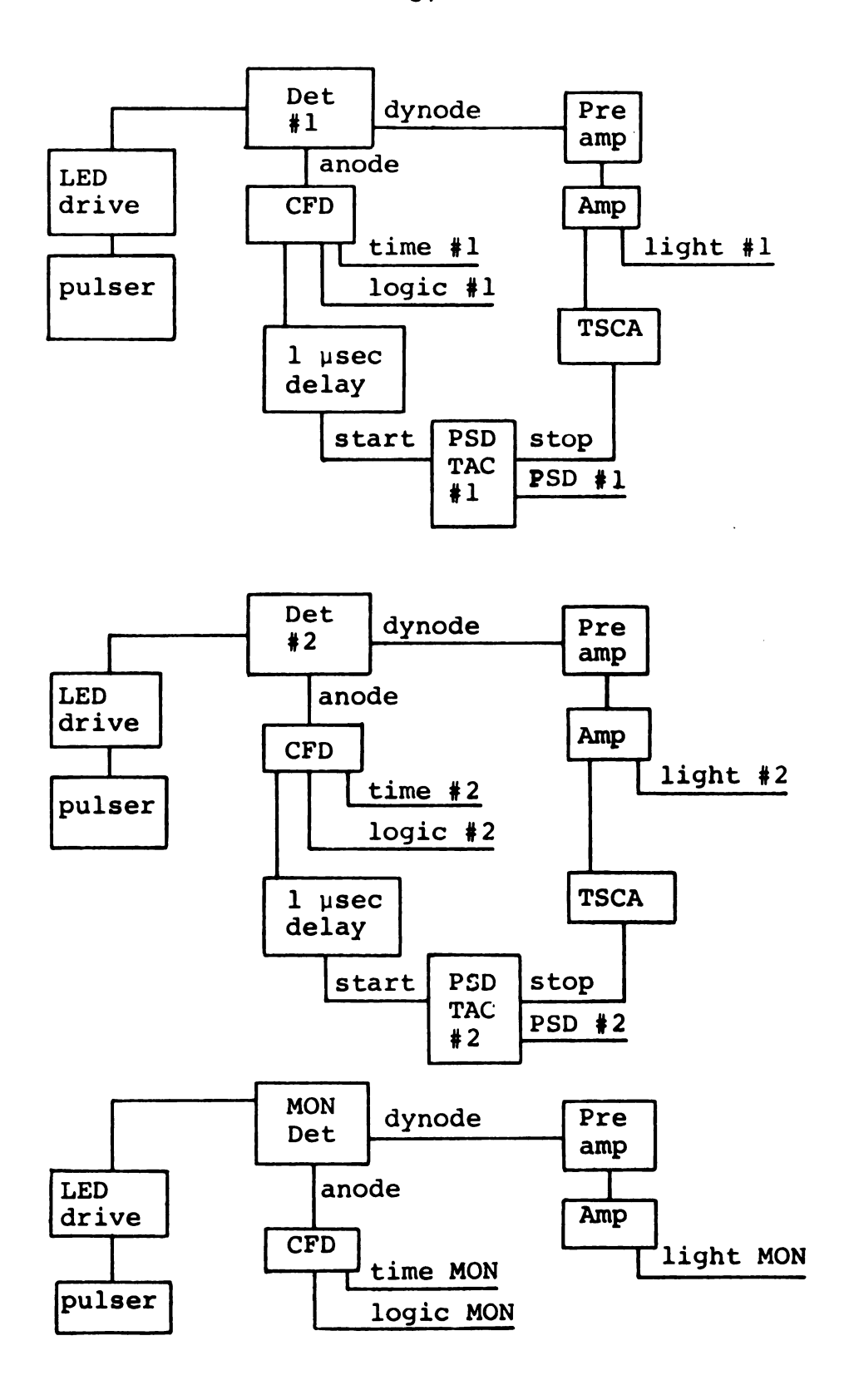


Figure 6. Vault Electronics

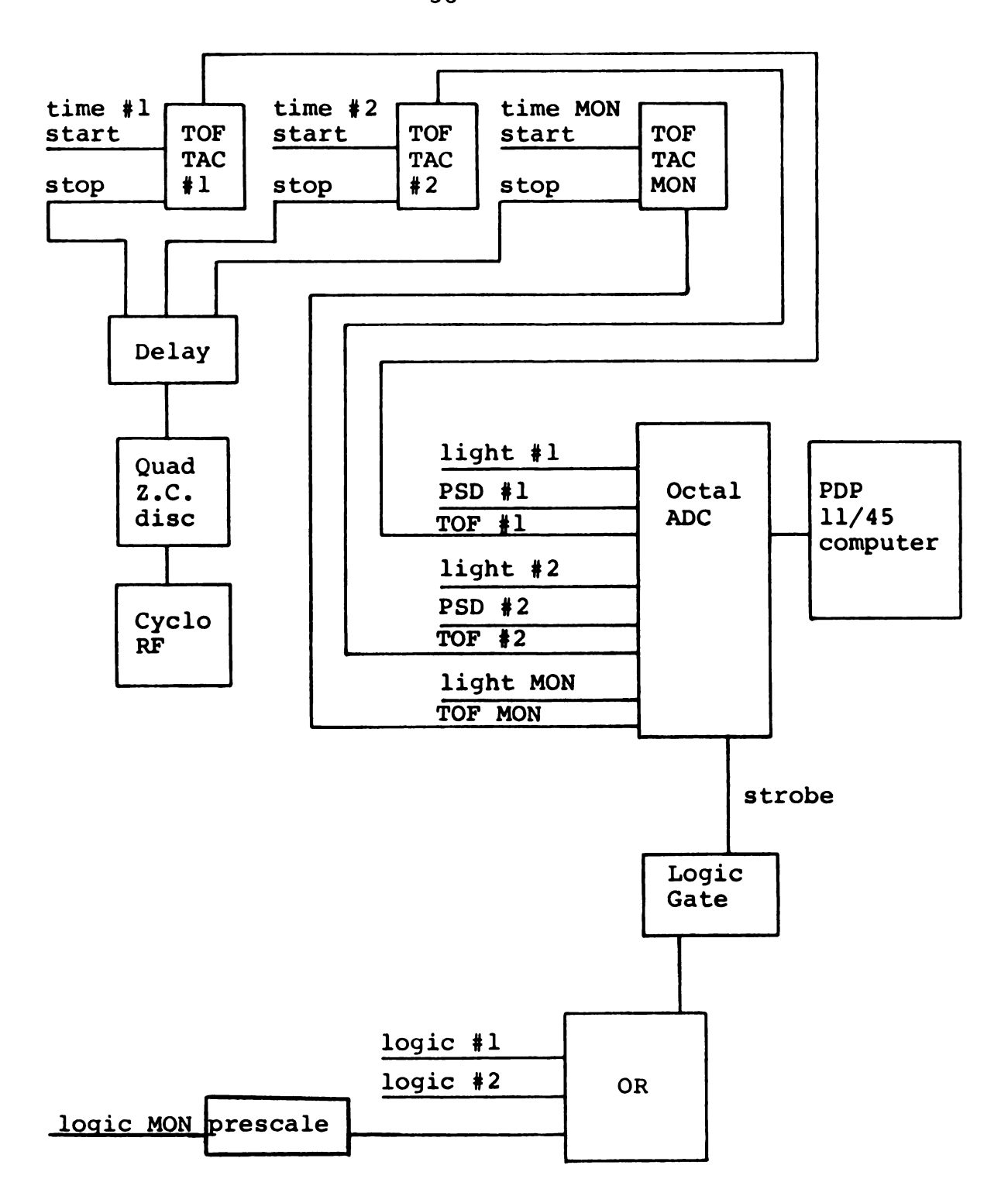
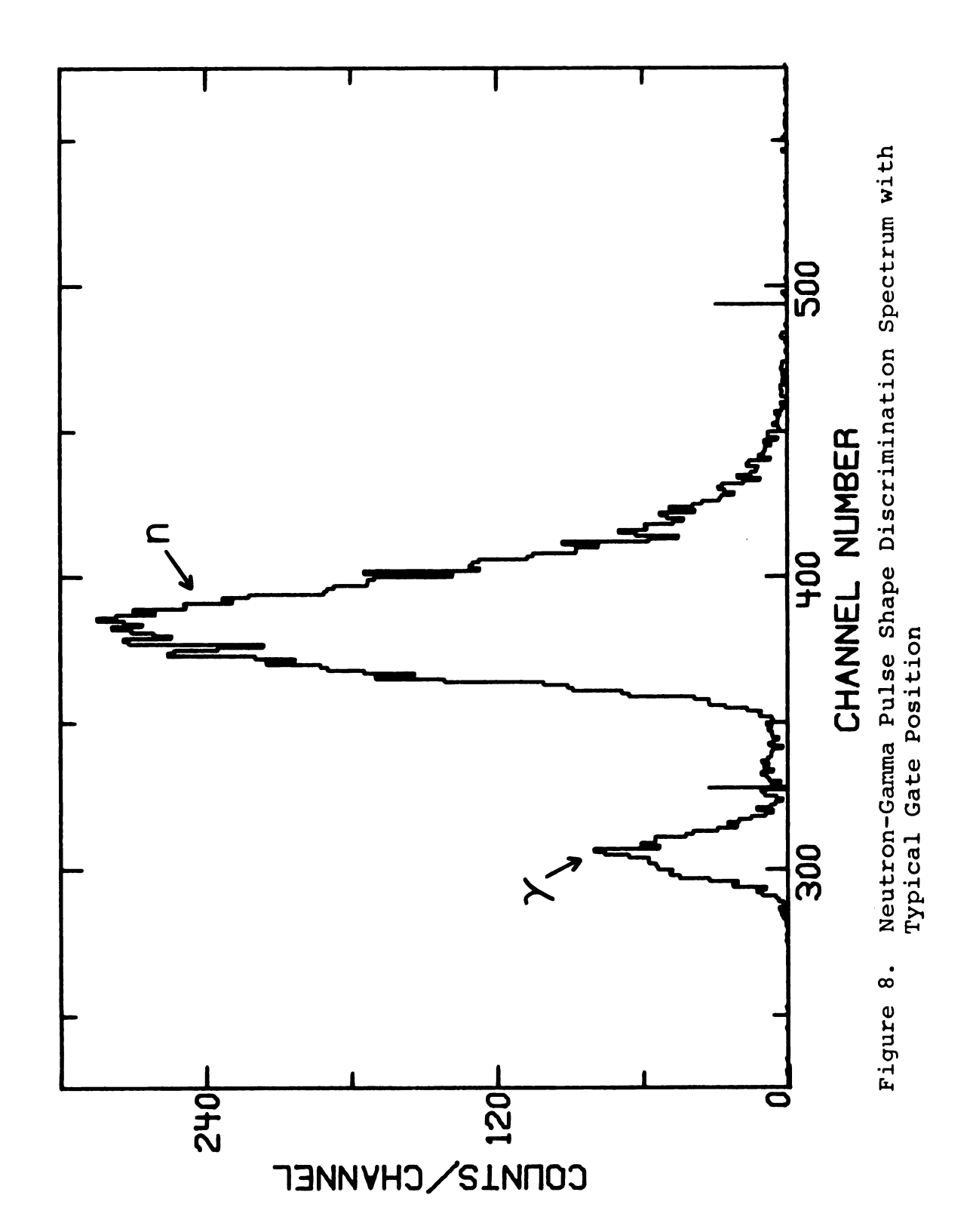


Figure 7. Data Room Electronics



## III. Data Acquisition Procedure

# A. Computer and Spectra Accumulation

The TAC, light and PSD signals from both neutron detectors along with TAC and light signal from the monitor detector are fed into an EG&G AD811 octal Amplitude to Digital Converter (ADC) as shown in Figure 7. The signals of each detector arrive at the ADC in coincidence with a strobe signal generated by the logic output of the relevent CFD. This Strobe activates the ADC which converts the voltage pulse height into digital format. This ADC is linked to a PDP 11/45 computer which reads the digitized values of the event and then performs the defined gating and data storage. Up to 8 spectra can be stored using the data taking program BKNTOF, which was used in all data runs. This program allows up to two gates on each spectrum. For example one could record the TOF spectra for a detector gated by PSD to require a neutron event and light to establish a known threshold.

The strobes from each detector were ORed in a Universal Coincidence box. The output of this Coincidence box was sent to a 4-Fold Logic Gate where it was transformed to the proper negative voltage to act as a strobe for the ADC.

The program records nine scalers; one internal that counted the number of processed ADC strobes and 8 more read from two quad scalers that recorded the total number of strobes sent to the ADC, the charge accumulated, the total

active time of the run, and the number of LED events for each detector.

During the time the computer is processing an event it is not sensitive to any other events that might reach the ADC. A measure of the computer dead time is obtained by comparing the number of events recorded by the ADC to the number of strobes recorded by the scaler for the same time span. For comparison of neutron detector yield to monitor yield the computer dead times for each detector are the same. The dead time due to the reset time of the electronics, with the TACs being the dominant source, was measured to be usually <0.1%. This agrees with dead times calculated from the reset time of the TACs. The 0° normalization runs had the largest dead time uncertainties, introducing a normalization error of <1%.

# B. Time of Flight Spectrum

For both main detectors and the monitor a TOF spectrum is recorded. This spectrum is gated by the light signal, accumulating only those events that produce a recoil in the scintillator with energy above a certain threshold. These thresholds are listed in Tables 1 and 2. In all but a few cases the main detector TOF spectra are also gated by the neutron part of the PSD spectrum. The monitor TOF spectrum is never gated by PSD as no PSD information is available for it. Figure 9 shows a typical TOF spectrum for 40 MeV neutrons scattered from silicon at  $\theta=65^{\circ}$ . The target-in,

target-out and subtracted spectra are shown. The first excited state of <sup>28</sup>Si at 1.76 MeV can be seen next to the larger elastic peak. Additional target-in TOF spectra are shown in Figure 37 thru Figure 43. Figure 10 shows the monitor TOF spectrum for a 40 MeV run. Spectra with the lithium target in place and without the lithium target are shown. The monitor spectrum for a 30 MeV run with the lithium target in place is shown in Figure 44.

## C. Normalization Procedure

The absolute normalization of the neutron elastic scattering cross sections was obtained by a ratio technique that removes dependence on some of the least well known quantities in the cross section calculation. This procedure involved measuring the yield of the  $^7\text{Li}(p,n)$  reaction at  $0^\circ$  with the same parameters as the scattering runs for each source to scatterer distance and each monitor position. The yield formula for the normalization run is discussed below (IV-B).

The experimental system was designed to accomodate the 10<sup>4</sup> difference in counts/charge experienced in the normalization runs compared to the angular distribution runs. The data acquisition program generated unacceptable dead times when the data rate above the electronic threshold was greater than about 700/sec. The computer count rate is the sum of the strobe rates from both detectors and the monitor. During the angular distribution measurements, the strobe rate in the monitor was prescaled by a factor of 10 and the detectors

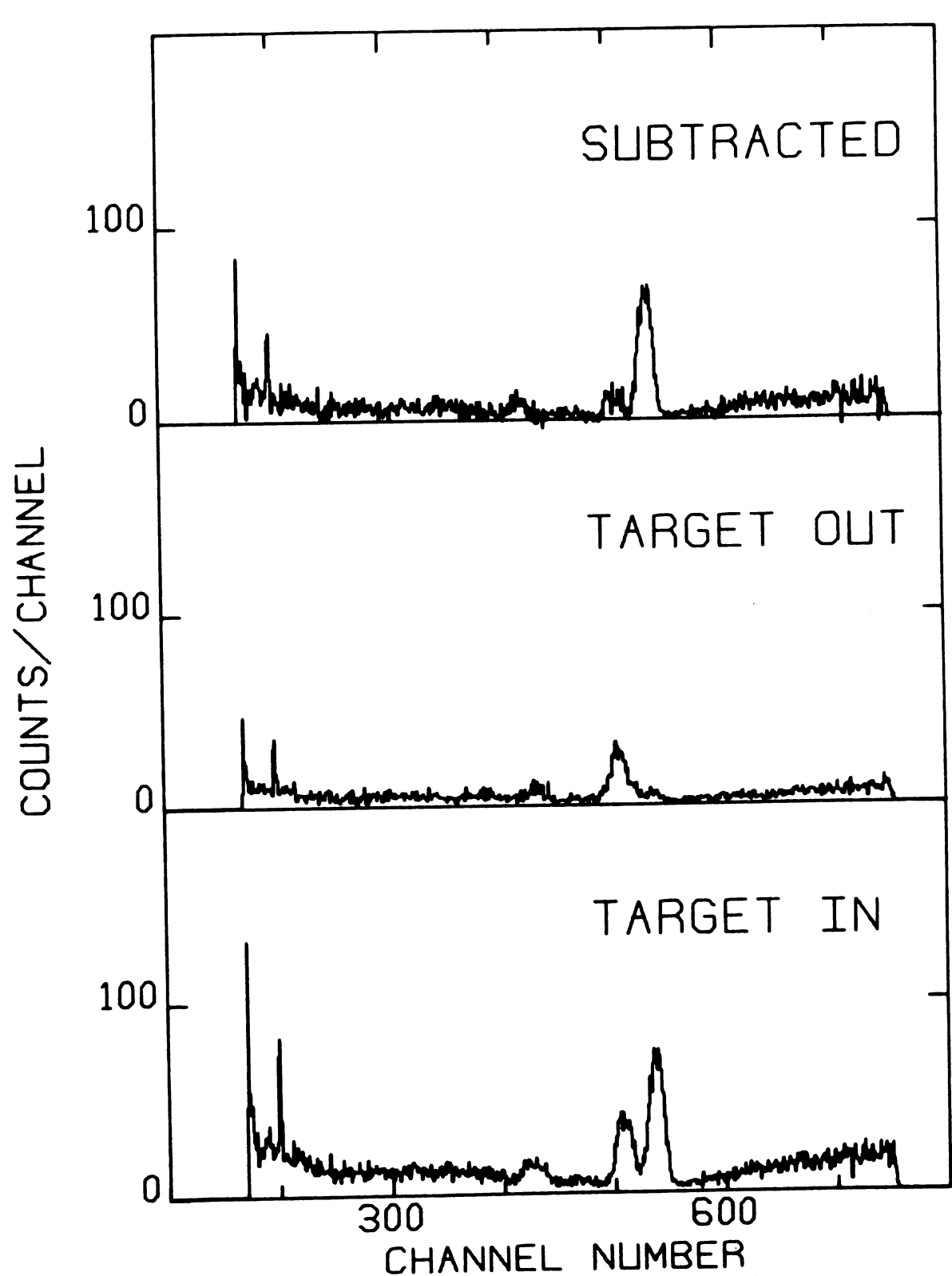


Figure 9. TOF Spectra 40 MeV, Si, 60° Target In, Target Out, Subtracted

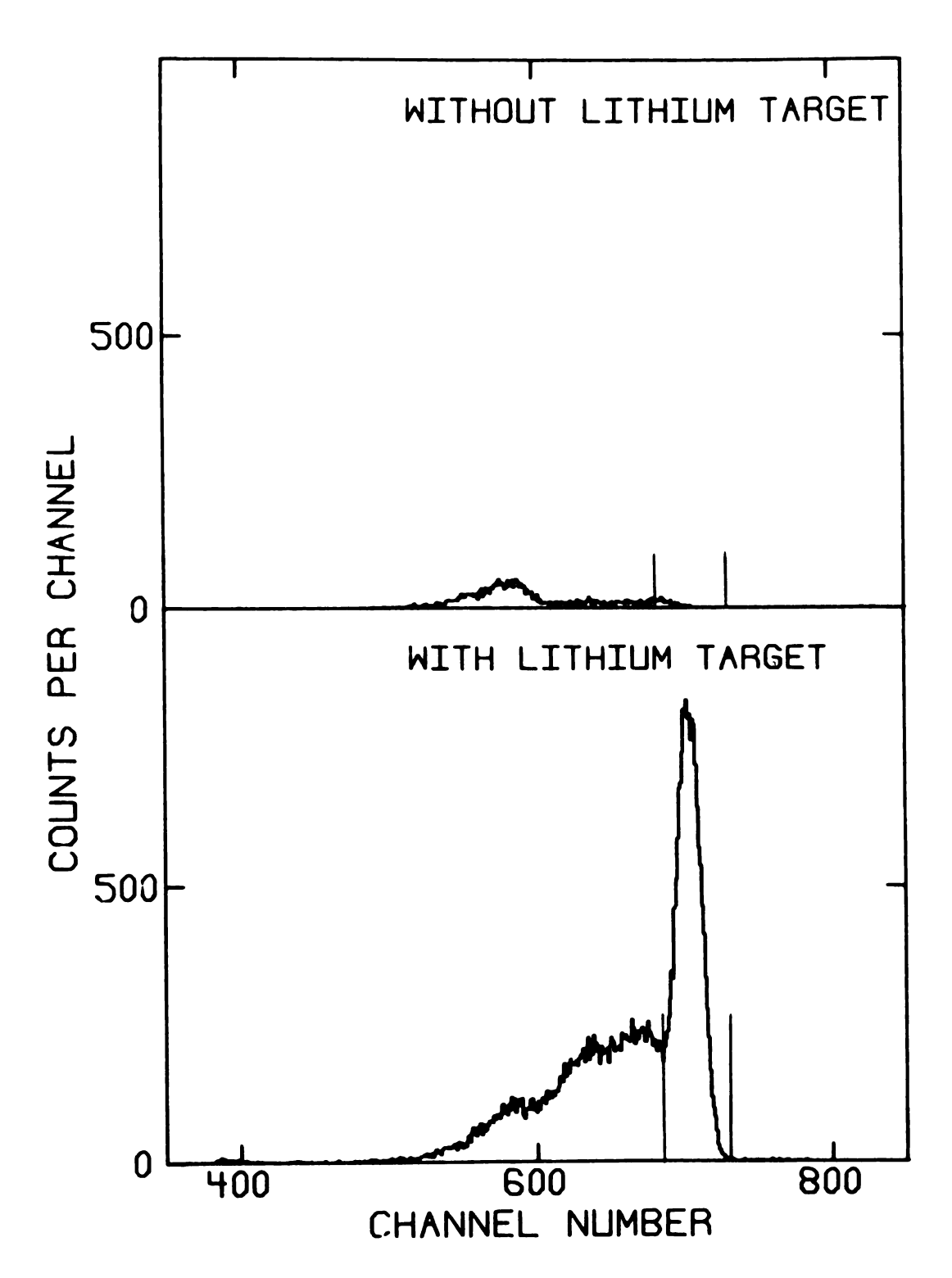


Figure 10. Monitor Spectrum 40 MeV Lithium Target In, Li Target Out

were not prescaled. During a 0°normalization run, the beam current was reduced to a few nA. The prescaler was removed from the monitor and the strobes for the two detectors were prescaled by a factor of 10. This procedure bridges the count rate gap between these two measurements, allowing the 0° runs to be done in an hour or two with 1.7% statistics. It was necessary to make a zero degree run whenever the monitor detector was changed or the source target to scattering target distance was changed.

## D. Background

Upon examining the sources of background we found that the nearby air produced about 90% of the background around the sample elastic peak. The contributions to air scattering were mapped using a scattering target of Mylar  $(C_{10}^{\rm H}_8^{\rm O}_4)$ . This target was positioned at various points in the scattering area and the yields recorded, thus determining the relative contributions. These measurements indicated that the air scatter dropped off rapidly as one moves away from the central scattering region, except for the forward direction where the fall off was slower. The holder produced the remaining background apart from a very small residual caused by many bounce paths.

The background causes a peak in the NTOF spectrum that lies under the elastic peak at the smallest angles and shifts to lower energy with increasing scattering angle.

The background yield becomes less intense, relative to target

yields, with increasing angle. Typically by 80° the air peak was no longer noticed in the TOF spectrum, except for \$^{12}\$C where the kinematics keeps the air peak and target peak inseparable. When the scattering sample is in place the background due to non-sample scattering will be slightly less than when the sample is removed because of flux attenuation by the sample. Based on the air scattering measurements and absorption of the samples this correction can be estimated. There is <1% effect on the deduced cross section for all cases except for lead at the forward angles where there was at most a 3.5% effect on the cross section.

A Helium bag was used during some of the early runs in an attempt to reduce this air scattering background. A large plastic bag that enclosed the scattering targets was filled with helium to a pressure that expanded the walls of the bag away from the scattering sample area. The concept did not work well in practice. Because of mechanical considerations and leakage problems it was eventually discarded.

#### IV. Data Reduction

#### A. Peak Areas

For all angles and for each run both target in and target out spectra were measured. To extract the target yield, the target out run of each detector was normalized by scaling it according to the ratio of monitor yields. Then the target out spectrum is subtracted channel by channel from the target in spectrum. This defines the elastic peak very well, and its area is obtained with no additional background subtracted.

The monitor yield is determined by defining specific channels around the large peak in the TOF spectrum as seen in Figure 10. The peak area is extracted with no background subtracted. From run to run the same limits of integration are used and a check of the resultant centroid is made. If the centroid varies by more than ±1 channel the limits are redefined so that the difference, centroid - lower limit, is constant to ±1 channel.

#### B. Cross Sections

The detector neutron yield for neutron scattering is given by

$$Y_{n,n}(\theta) = \left[\frac{d\sigma}{d\Omega}Li(0^{\circ})\frac{T\rho QN}{7d^{2}}A\right] \times \left[\frac{d\sigma}{d\Omega}exp(\theta)NN_{A}\epsilon(E)\frac{AR}{D^{2}}\right] \quad (IV-1)$$

where,  $N_A = Avogadro's number$ 

D= scatterer to detector distance

T= 7Li target thickness

Q= number of incident protons

 $\epsilon$  (E) = detector efficiency at E<sub>n</sub>=E

A= area of detector

 $\rho$ = Li target density

d= Li to scatterer distance

N= moles of scatterer

R= finite angle correction for incident neutron
 intensity.

The intensity correction R is given by

$$R = \frac{\int_{\text{scatterer}} \frac{d\sigma}{d\Omega} \operatorname{Li}^{(\theta)} d\Omega}{\int_{\text{detector}} \frac{d\sigma}{d\Omega} \operatorname{Li}^{(\theta)} d\Omega} .$$

The detector yield for the  $0^{\circ}$  (p,n) reaction is given by

$$Y_{p,n}(0^{O}) = \frac{d\sigma}{d\Omega} L_{i}(0^{O}) \frac{TQ' \varepsilon (E') A\rho N_{A}}{7 (d+D)^{2}}$$
(IV-2)

where, Q'= number of incident protons E'= energy of  $0^{\circ}$  neutrons.

Incorporating equation IV-2 into equation IV-1 we find

$$\frac{Y_{n,n}(\theta)}{Q'} = \frac{Y_{p,n}(0^{\circ})}{Q} \frac{(d+D)^{2} \varepsilon(E)}{d^{2} p^{2} \varepsilon(E')} NN_{A} \frac{d\sigma}{d\Omega} \exp(\theta) R. \quad (IV-3)$$

Solving for the differential cross section we find

$$\frac{d\sigma}{d\Omega} \exp^{(\theta) = \frac{Y}{n, n} (\theta)} \frac{Q}{Q}, \quad \frac{d^2D^2 \epsilon(E')}{(d+D)^2 \epsilon(E)} \frac{1661}{NR}, \quad (IV-4)$$

where the cross section is in mb/sr and the distances D and d are measured in cm. In terms of monitor yields the cross section is given by

$$\frac{d\sigma}{d\Omega} \exp^{(\theta)} = \frac{Y_{n,n}(\theta)}{Y_{p,n}(0^{\circ})M(\theta)} \frac{M(0^{\circ})}{(d+D)^{2} \varepsilon(E)} \frac{1661}{NR}, \quad (IV-5)$$

where  $M(0^{\circ})$  is the monitor yield for the  $0^{\circ}(p,n)$  run and  $M(\theta)$  the monitor yield for the neutron scattering run. In this formulation the pairs  $Y_{n,n}(\theta)$  with  $M(\theta)$  and  $Y_{p,n}$  $(0^{\circ})$  with  $M(0^{\circ})$  can be the raw yields with no computer dead time correction, as it is the same for Y and M. results of equations IV-5 and IV-4 were almost always the same as the monitor to charge ratio was nearly always constant 1%. The cross section obtained from equation IV-5 is the experimentally measured cross section,  $\boldsymbol{\sigma}_{\mbox{\footnotesize{exp'}}}$  tabulated in Table 14 as the uncorrected laboratory It has not been corrected for finite angle, cross section. multiple scattering or attenuation effects and is not corrected for these effects prior to optical model searches. Instead the calculated OM cross sections in the Lab frame are themselves smeared to mimic the experimentally determined cross sections by incorporating a Monte-Carlo subroutine in the OM search code.

#### C. Neutron Detection Efficiency

The efficiency of the neutron detectors has been calculated using the program TOTEFF as modified by Doering (Do74). A set of calculated efficiency curves are shown in Figure 11 for three different thresholds. The light from the scintillator is calibrated in equivalent electron These electron energies are measured by Compton recoil electrons due to gamma ray sources. The maximum electron energy corresponds to the Compton edge and is the distinguishing feature in these low Z detectors. The  $^{228}$ Th source (E $_{v}$ =2.615 MeV) was our standard and thresholds were set in terms of the equivalent number of Th Compton edges. The Compton edge peak and half height were measured and the edge extracted based on a study of these quantities in relation to the true edge by Galonsky and Doering (Ga78).

The calculated efficiencies are accurate to about 10%, but efficiency enters the cross section calculation only in ratios of efficiencies. The relative effeciencies depend only weakly on the efficiency curve. For carbon some uncertainty is introduced in the back angles because of the large kinematic shift of the scattered neutrons. As the targets get heavier this effect becomes less important.

## D. Experimental Errors

The major source of error in the measured experimental cross sections is statistics. The fractional error for the (target in)-(target out) yield is

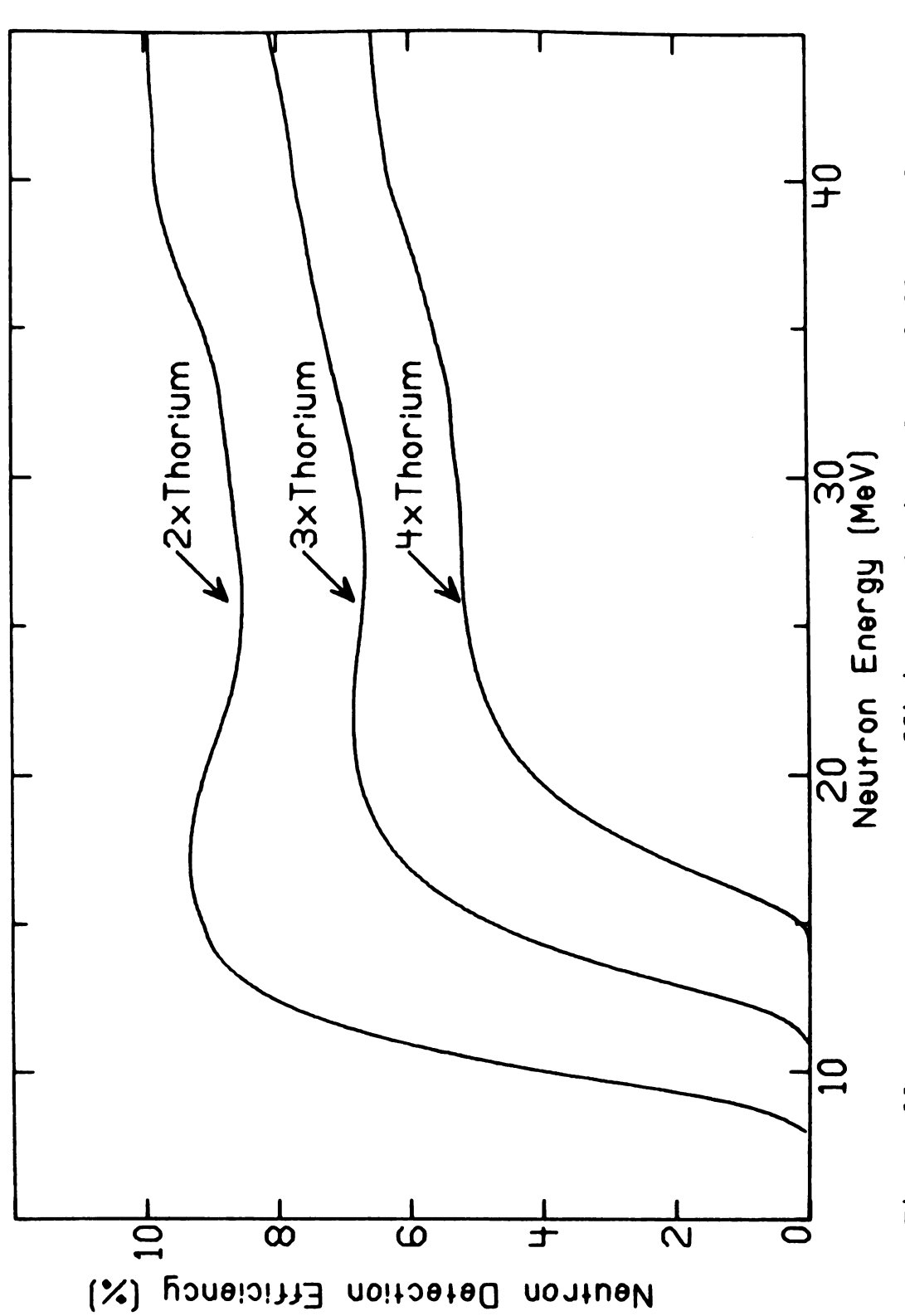


Figure 11. Neutron Detector Efficiency, Thorium edge = 2.38 MeV electron energy

$$\frac{\Delta Y}{V} = (Y_{in} + Y_{out})^{1/2} / (Y_{in} - Y_{out})$$

where  $\Delta Y$  is the error in the target yield,  $Y_{in}$  is the yield for the target in run (this includes target yield + back-ground) and  $Y_{out}$  is the normalized yield for the target out run (see Table 5).

Compound nuclear contributions to the cross sections are not reproduced by simple Optical Model Calculations. Thus before fitting data with a simple OMP it is necessary to subtract out any contributions due to compound nuclear elastic scattering. Rapaport et al. (Ra77) have estimated this effect by a Hauser-Feshbach calculation for neutron scattering at lower bombarding energies. They find the correction to be ±1% for 20 and 26 MeV scattering. Since this contribution to the elastic scattering decreases with increasing bombarding energy, we did not repeat their calculation but rather assumed compound nuclear elastic scattering contributions to be negligible.

Since calcium is reactive in air, during the brief time it was exposed to air during the canning process it invariably absorbed some oxygen. Elastic scattering from this absorbed contaminant would contribute at the forward angles. Beyond about 60° the neutrons elastically scattered from oxygen will be shifted in energy away from the calcium scattered neutrons due to the kinematics. The oxygen contamination also caused a small uncertainty in the absolute normalization since the sample's composition was not exactly known.

The Lithium target to scattering target distance (d) is known to  $\pm 1$  mm causing an error ranging from 2% for d=11.0 cm to <1% for d=24.4 cm. The mean scattering angle is known to about  $\pm 0.5^{\circ}$  for d=11.0 cm,  $\pm 0.3^{\circ}$  for d=18.4 cm and  $\pm 0.2^{\circ}$  for d=24.4 cm.

During each run, before the Li target to scattering target distance was changed the yield measurement at one or two angles was repeated. After the Li target to scattering target distance was changed, or if the monitor position was changed the yield measurement was repeated at one or two angles. These checks gave results consistent within the experimental error.

Table 5. Experimental Errors

# Relative Uncertainties(%)

Statistics in Yields:	15 <sup>0</sup> -90 <sup>0</sup> 95 <sup>0</sup> -160 <sup>0</sup>	<1-5 3-25
Monitor Statistics		<1
Finite Geometry		1-8 <sup>(a)</sup>
Compound Nuclear Contribution		<1
Contaminants		1 <sup>(c)</sup>
Background Attenuation Due to Samp	le	<1-3.5
Detector Efficiency		<1-2 <sup>(b)</sup>
Incident Angle of Proton Beam		1
Scattering Target Position		<1-2
Mean Scattering Angle		0.2°-0.5°

# Normalization Uncertainties(%)

Statistics in Yields, 0°flux	<1
Monitor Statistics, 0° flux	1.7
Dead Time Correction	<1
Flux Anisotrophy Correction	<u>≤</u> 1
Number of Target Nuclei	<1

Total 2.6

- a) Applicable only to center-of-mass cross sections
- b) Applicable only to C, Si, S, and Ca
- c) Ca only at forward angles

## V. Data Analysis

# A. Optical Model Parameter Search Code

The cross section determined by equation IV-5 is uncorrected for multiple scattering, finite angle or attenuation effects. The multiple scattering cross section depends on the entire single scattering angular distribution. The finite angle correction depends on the slope of the cross section around the mean scattering angle. To treat these effects we have chosen to smear the predicted Optical Model cross sections instead of attempting to correct the experimental data. Correcting lower energy data (Ki70) is acceptable because the cross sections do not vary so fast and smaller samples are used so multiple scattering effects are not as great. From equation II-1 we see that as the energy increases, flight paths must become longer to maintain the same energy resolution. Thus larger targets are needed to maintain a good data rate. Also, as the energy increases, the cross section slope tends to increase, making the finite angle correction larger.

Thus the Optical Model search code GIBELUMP (Pe66) has been modified and this new version of the code is called GIBSCAT. The code GIBELUMP calculates the c.m. elastic scattering cross section from a given set of OM parameters. It established the relation between a decrease in  $\chi^2$  and parameter variation where

$$\chi^{2} = \sum_{i=1}^{N} \left[ \frac{\frac{d\sigma}{d\Omega} \operatorname{calc}^{(\theta_{i})} - \frac{d\sigma}{d\Omega} \exp^{(\theta_{i})}}{\frac{d\sigma}{d\Omega} \exp^{(\theta_{i})}} \right]^{2} \qquad (V-1)$$

GIBSCAT differs from GIBELUMP in that prior to comparison with experimental data the c.m. cross section is converted into the lab cross section and transformed to include multiple scattering, finite angle and attenuation effects by the subroutine MULSCAT. The subroutine MULSCAT is based on the Monte Carlo code developed by Kinney (Ki70).

This code proceeds as shown in the flow chart in Figure 12. The initial OM parameters, geometry and experimental cross sections are read in. The code calculates the center of mass cross sections from the Optical Model potential then converts these cross sections to the lab frame. Then the Monte Carlo routine calculates the smeared cross section  $\sigma_{\rm calc}(\theta)$  that includes multiple scattering, finite geometry and attenuation. This smeared cross section is compared to the experimental one by equation V-1. The gradient in  $\chi^2$  space is determined by first varying the OM parameters. Then a revised smeared cross section is calculated by

$$\sigma_{\text{calc}}^{(\theta)} = \frac{\sigma_{\text{OM}}^{\text{new}}(\theta)}{\sigma_{\text{OM}}^{\text{old}}(\theta)} \sigma_{\text{calc}}^{(\theta)}$$
 (V-2)

where  $\sigma_{\text{calc}}(\theta)$  is the smeared cross section determined by Monte Carlo,  $\sigma_{\text{OM}}^{\text{old}}(\theta)$  is the laboratory cross section calculated by the original set of Optical Model parameters,

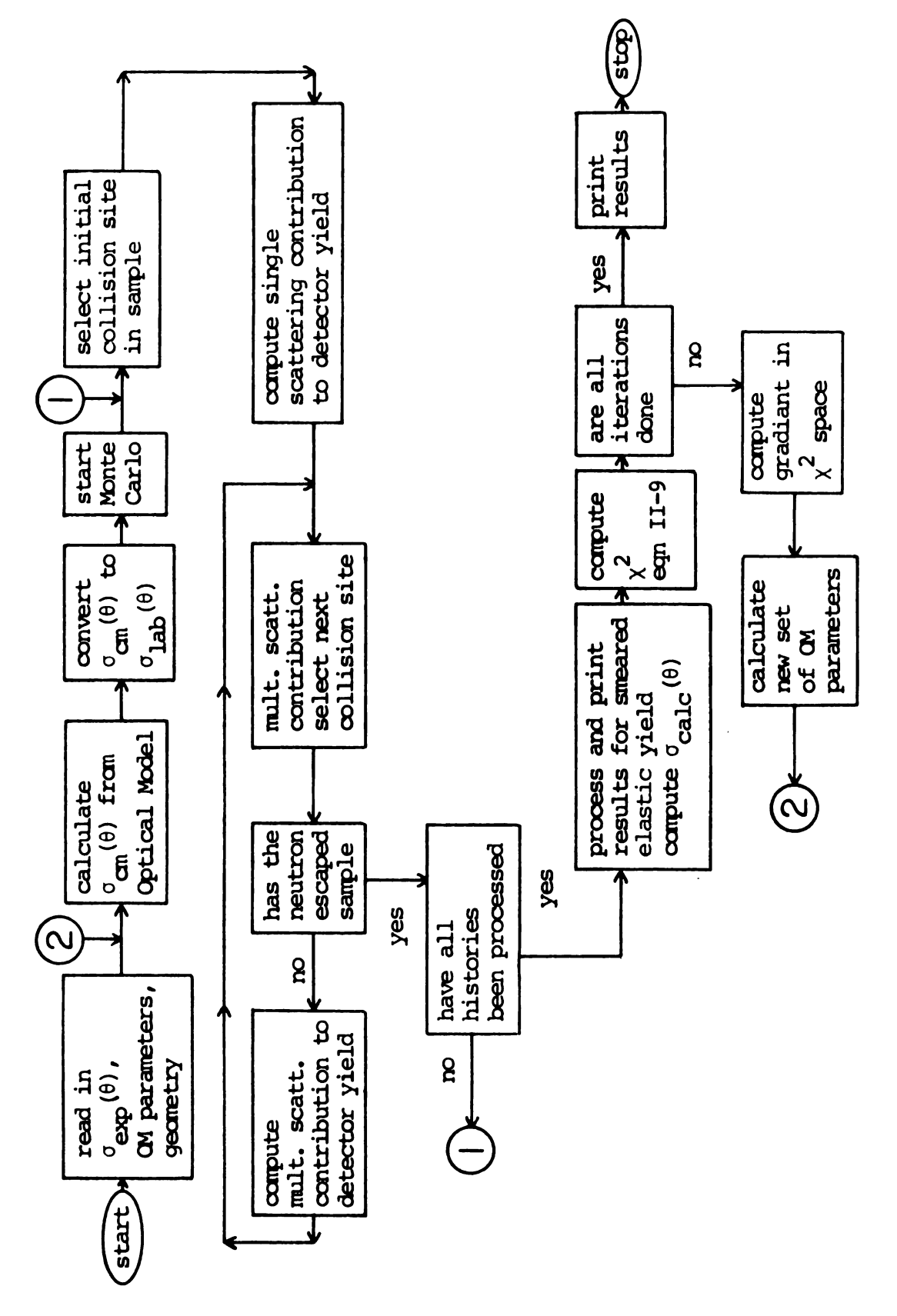


Figure 12. Fow chart for GIBSCAT

 $\sigma_{\rm OM}^{\rm new}(\theta)$  is the laboratory cross section calculated by the varied OM parameters, and  $\sigma_{\rm calc}(\theta)$  is the revised smeared cross section which is to be used in calculating the  $\chi^2$  gradient. Then guided by this gradient a new set of OM parameters is determined. The program then recalculates  $\sigma_{\rm calc}(\theta)$  from these new OM parameters until the predetermined number of iterations is reached.

Due to the nonexact calculation of  $\chi^2$  gradient, the procedure did not always converge. In practice the program was only allowed to proceed a few iterations per run. Then the best set of OM parameters was used as input for the next run.

The vast majority of computer time in these searches is spent in the Monte Carlo routine. The calculation of cross sections from OM parameters for 21 data points uses about 0.1 minutes of computer time. To correct these data points by the Monte Carlo routine using 3000 histories takes about 11.3 minutes.

## B. Center of Mass Cross Sections

The measured cross section  $\sigma_{\mbox{exp}}$  can be divided into two components, the single scattering and the multiple scattering contributions by,

$$\sigma_{\text{exp}}(\theta) = \sigma_{\text{LAB}}(\theta) \left[ \frac{\sigma_{\text{s}}^{\prime}}{\sigma_{\text{LAB}}} \right] + \sigma_{\text{MS}}^{\prime}$$
 (V-3)

 $\sigma_{LAB}(\theta)$ =true laboratory cross sections

 $\sigma_s' = \text{single scattering contribution to the measured cross section}$ 

 $\sigma_{MS}^{\prime}=$  multiple scattering contribution to the measured cross section.

The calculated smeared cross section  $\sigma_{\mbox{calc}}$  is also separated into single and multiple scattering compounds by

$$\sigma_{\text{calc}}(\theta) = \sigma_{\text{OM}} \left( \frac{\sigma_{\text{S}}}{\sigma_{\text{OM}}} \right) + \sigma_{\text{MS}}$$
 (V-4)

where

 $\sigma_{\mbox{\scriptsize OM}}^{} =$  calculated OM laboratory cross section

 $\sigma_s$  = single scattering contribution to the smeared calculated cross section

 $\sigma_{MS}^{}\text{=}$  multiple scattering contribution to the smeared calculated cross section

The multiple scattering contribution depends on the entire angular distribution and not on the value at one angle. If local fluctuations between  $\sigma_{\rm exp}(\theta)$  and  $\sigma_{\rm calc}(\theta)$  have random signs and the deviations are small we can extract  $\sigma_{\rm LAB}(\theta)$ . We assume the multiple scattering contribution is determined since, if the fluctuations are random and small, then the average cross section is well determined. Also we assume that the finite angle and attenuation effects are accurately determined from the Monte Carlo routine, i.e.

$$\left(\frac{\sigma_{\mathbf{S}}^{\prime}}{\sigma_{\mathbf{LAB}}}\right) = \left(\frac{\sigma_{\mathbf{S}}}{\sigma_{\mathbf{OM}}}\right) .$$
(V-5)

Then the true cross section  $\boldsymbol{\sigma}_{\mathbf{LAB}}$  is given by

$$\sigma_{LAB} = (\sigma_{exp} - \sigma_{calc}) \left( \frac{\sigma_{OM}}{\sigma_{s}} \right)^{+\sigma_{OM}}$$
 (V-6)

From this the true center of mass cross sections are deduced by directly converting to the center of mass frame.

In all but one case the conditions leading to equation V-6 are fulfilled by the final best fit OM prediction.

The deduced center of mass cross sections are tabulated in Table 14 and shown in Figures 38 to 50.

In the case of 40 MeV scattering on lead the conditions for equation V-6 break down. As seen in Figure 37 in the angular range  $75^{\circ}$  to  $115^{\circ}$  the smeared calculated cross section  $\sigma_{\rm calc}(\theta)$  is larger than  $\sigma_{\rm exp}(\theta)$ . In this region a scale factor seems more appropriate to correct the difference between  $\sigma_{\rm calc}(\theta)$  and  $\sigma_{\rm exp}(\theta)$ . In the region  $(81^{\circ}-110^{\circ})$  the true laboratory cross section is determined by

 $\sigma_{LAB} = \sigma_{OM} \left( \frac{\sigma_{exp}}{\sigma_{calc}} \right) . \qquad (V-7)$ 

For the final determination of the true center of mass cross section, the Monte Carlo routine with 10,000 histories was run at least twice. The results were compared and found to be in excellent agreement. The uncertainty in the deduced center of mass cross sections due to the finite geometry correction is estimated to be between 1 to 8% depending on the target. The largest correction errors are for Pb near the first cross section minimum. All other targets had correction errors <2%. The corrected center of mass cross sections are tabulated in Table 14 under the heading Corrected Center of Mass.

#### C. Parameter Search Procedure

For each angular distribution a set of OM parameters was determined. These parameters represent the best fit in terms of  $\chi^2$  minimization. The search procedure was guided to help eliminate ambiguities in related parameters. One search sequence was to vary first V,  $W_D$ ,  $W_V$  and obtain the best fit then V,  $a_R$ ,  $W_D$ ,  $W_V$ ,  $r_I$ : and then V,  $r_R$ ,  $a_R$ ,  $W_D$ ,  $W_V$ ,  $r_I$ ,  $a_I$ . The other search sequence used was to vary only uncoupled parameters such as V,  $r_I$  or  $r_R$ ,  $r_I$  or  $r_I$ ,  $r_I$ ,  $r_I$  or  $r_I$ ,  $r_$ 

Several global OM parameter sets were used for starting parameters. Namely those of Becchetti and Greenlees (Be69) (BG); Patterson, Doering and Galonsky (Pa76) (PDG); Rapaport (Ra79) set A (RAPA) and Rapaport (Ra79) set B (RAPB). Table 6 lists the  $\chi^2/N$  for each of these parameter sets.

The initial search uses the program GIBSCAT and searches until a "good" fit to  $\sigma_{\rm exp}$  is achieved. A "good" fit is one that meets the conditions for applying equation V-6. From this fit the center of mass cross sections are determined by equation V-6. GIBELUMP is used to search on

Table 6.  $\chi^2/N$  of Global Parameter sets (a)

<u>Nuclei</u>	Neutron Energy (MeV)	2 N B.G.	X N PDG	X N Rap A	X N Rap B
12 <sub>C</sub>	40.0	54.	280.	200.	120.
28 <sub>Si</sub>	30.3	26.	140.	21.	20.
28 <sub>Si</sub>	40.0	34.	200.	22.	20.
32 <sub>S</sub>	30.3	21.	84.	21.	40.
32 <sub>S</sub>	40.0	71.	173.	70.	22.
40 <sub>Ca</sub>	30.3	19.	43.	42.	26.
40 <sub>Ca</sub>	40.0	21.	111.	40.	40.
208 <sub>Pb</sub>	30.3	82.	87.	140.	140.
208 <sub>Pb</sub>	40.0	73.	27.	180.	180.

a) as given by equation V-1

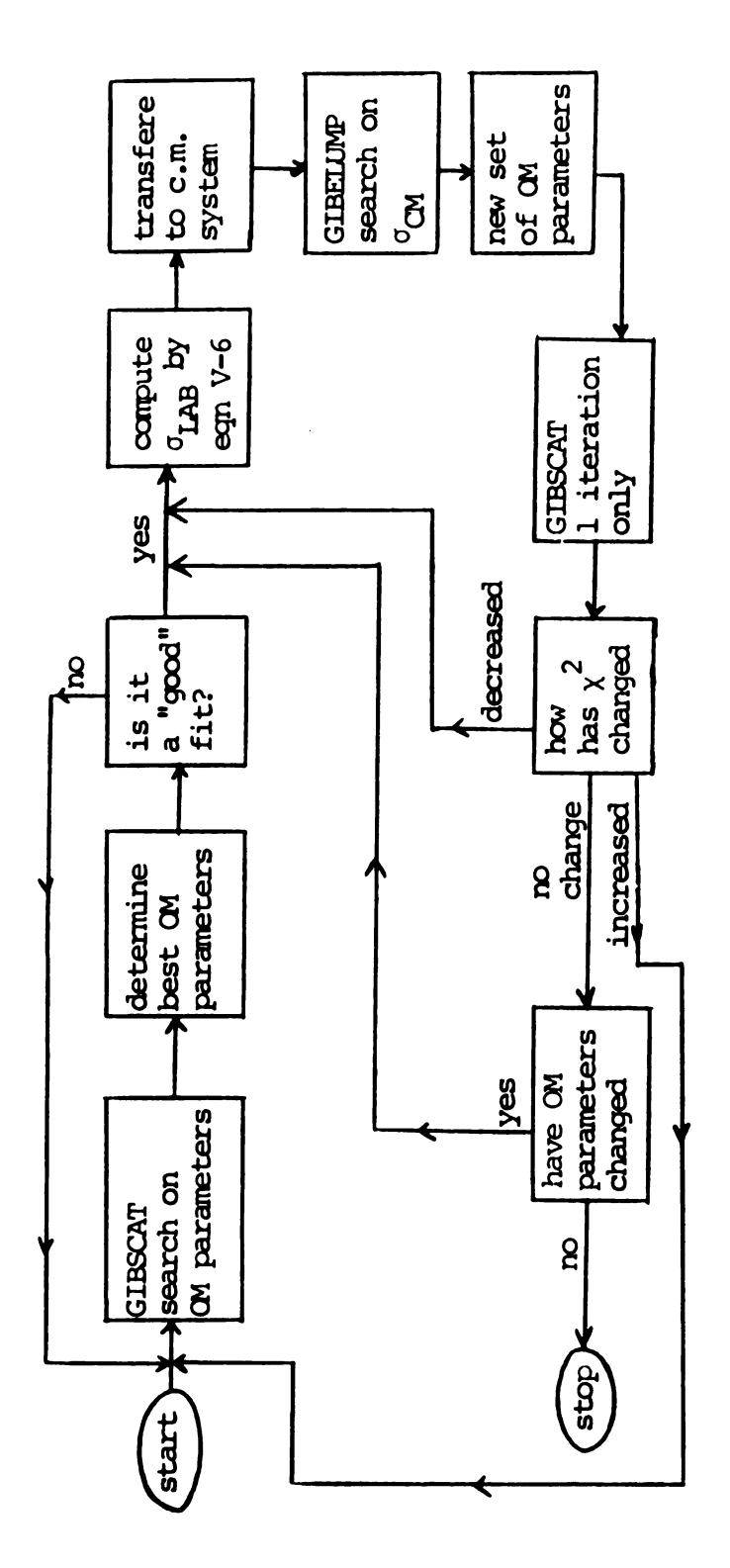


Figure 13. Search Procedure

 $\sigma_{CM}$  and a new set of OM parameters are determined. GIBSCAT is run for 1 iteration using this new OMP. The change in  $\chi^2$  is then checked compared to the previous run of GIBSCAT. If the  $\chi^2$  decreases the procedure iterates as shown in Figure 13. If the  $\chi^2$  has increased we go back to searching on  $\sigma_{exp}$  using GIBSCAT. The search procedure is terminated when no further decrease in  $\chi^2$  is achieved and the OM parameters remain constant. The OMP derived from this search procedure are tabulated in Table 7 for 30 MeV neutrons and in Table 8 for 40 MeV neutrons.

The absolute normalizations of the final results are those values determined experimentally. For each angular distribution a search on the absolute normalization was conducted. These searches gave either no improvement or minimally improved  $\chi^2$  for normalization changes on the order of a few per cent. For those samples that were of natural abundance, no correction was introduced for the small admixture of other isotopes. A calculation assuming the Becchetti and Greenlees Optical Model potential (Be69) show that the correction is less than 0.1% in the potential depths.

## D. Volume Integrals

The determination of a set of potential parameters always entails a certain amount of ambiguity. The nature of a multiparameter search procedure, the slightly different results for various starting values of the potential parameters and interrelationships between parameters make

Table 7. Optical Model Parameters

MeV
m
30.
II
ᇤ

V (MeV)	r <sub>R</sub> V) (fm)	a <sub>R</sub> (fm)	${\sf W}_{\sf V}$	W <sub>D</sub> (MeV)	r <sub>I</sub> (fm)	a <sub>I</sub> (fm)	$^{\mathrm{N}}$
							Ì
42.06	203	0.679	11.81	0.948	1.280	0.605	6.2
45.33 1	1.176	902.0	0.249	8.486	1.280	0.531 4.6	4.6
47.26 1	.145		2.273	5.081	1.381	0.567	2.5
	.152 <sup>b</sup>		0.142	7.749	1.309 <sup>b</sup>	0.549 <sup>b</sup>	3.6
43.30 1.	1.171	0.699	3.777	3.570	1.270	0.650 9.0	0.6
	.183 <sup>c</sup>		4.244	2.938	1.273 <sup>c</sup>	0.699	11.0

 $^{\rm V}_{\rm s.o.}$  =6.2 MeV,  $^{\rm r}_{\rm s.o.}$  =1.01 fm, and  $^{\rm a}_{\rm s.o.}$  =0.75 fm were kept constant

- Laboratory cross section, relative errors only, equation V-1 a)
- Kept constant during search, average geometry of van Oers (Va71) Q Q
  - Kept constant during search, average geometry of van Oers (Va74) ΰ

Table 8. Optical Model Parameters

MeV
40.0
11
E L

Nuclei	V (MeV)	r <sub>R</sub> (fm)	a <sub>R</sub> (fm)	W <sub>V</sub> (MeV)	W <sub>D</sub> (MeV)	r <sub>I</sub> (fm)	a <sub>I</sub> (fm)	N×2 (a)
12 <sub>C</sub>	41.30	1.127	0.637	1.829	3.609	1.143	0.892	5.1
28 <sub>Si</sub>	39.19	1.158	0.732	9.780	0.363	1.292	0.675	7.6
32 <sub>S</sub>	41.91	1.170	0.712	7.793	1.531	1.368	0.577	7.7
40 <sub>Ca</sub>	38.02	1.184	0.726	5.890	1.461	1.352	0.616	2.7
40 <sub>Ca</sub>	40.73	1.152 <sup>b</sup>	0.692 <sup>b</sup>	3.731	3.738	1.309 <sup>b</sup>	0.549 <sup>b</sup>	5.4
$208_{ m Pb}$	41.00	1.155	0.751	6.054	0.0	1.406	0.641	8.5
$208_{ m Pb}$	39.59	1.183	0.724 <sup>c</sup>	6.590	1.542	1.273 <sup>C</sup>	0.699	27. (6.7) <sup>d</sup>

 $V_{s.o.}=6.2$  MeV,  $r_{s.o.}=1.01$  fm, and a<sub>s.o.</sub>=0.75 fm were kept constant

Laboratory cross sections, relative errors only a)

Kept constant during search, average geometry of van Oers (Va71) Q Q

Kept constant during search, average geometry of van Oers (Va74)  $\widehat{\mathbf{c}}$ 

 $<sup>\</sup>theta < 115^{\circ}$ 

comparison between different nuclei and energies difficult. Feshbach in 1958 (Fe58) suggested that the volume integral of the potential,

$$J = \int V(r) d^{3}r$$
 (V-8)

is a better measure of the strength of the potential and it is now well verified that J is determined better than V,  $r_R$  and  $a_R$  separately. Another well determined quantity is the mean-square radius defined as

$$\langle r^2 \rangle = \int \frac{V(r) r^2 d^3 \dot{r}}{\int V(r) d^3 \dot{r}}$$
 (V-9)

For each nucleus at each energy we have determined the volume integral per nucleon as well as the root-mean-square radii for both the real and imaginary potentials. For the volume terms  $(V_R, W_V)$  in the parameterization one finds that the volume integral per nucleon is (approximately)

$$\frac{J_{\text{vol}}}{A} = \frac{4\pi}{3} \text{ Vr}^{3} \left[ 1 + \left( \frac{\pi a}{rA^{1/3}} \right)^{2} \right] , \qquad (V-10)$$

while the mean-square radius is given by

$$r_{\text{vol}}^2 = \frac{1}{5} (3r^2 A^{2/3} + 7\pi^2 a^2).$$
 (V-11)

for the derivative Woods-Saxon term the volume integral is (approximately)

$$\frac{J_{D}}{A} = \frac{16\pi r^{2} aW_{D}}{A^{1/3}} \left[ 1 + \frac{1}{3} \left( \frac{\pi a}{rA^{1/3}} \right)^{2} \right]$$
 (V-12)

Table 9. Volume Integrals and rms Radii

Nuclei	Neutron Energy (MeV)	(J/A) real (MeV·fm <sup>3</sup> )	$r^2 > \frac{1/2}{\text{real}}$	(J/A) imag (MeV•fm <sup>3</sup> )	<r<sup>2&gt;1/2 imag (fm)</r<sup>
<sup>12</sup> C	40.0	396.4	3.10	152.	3.37
28 <sub>Si</sub>	30.3	410.9	3.79	145.4	3.81
28 <sub>Si</sub>	40.0	355.6	3.78	121.6	3.96
32 <sub>S</sub>	30.3	427.8	3.81	125.2	4.26
<sup>32</sup> s	40.0	383.0	3.91	125.7	4.13
40 <sub>Ca</sub>	30.3	412.7	4.17	113.2	5.02
40 <sub>Ca</sub> a	30.3	395.3	3.99	114.0	4.67
40 <sub>Ca</sub>	40.0	348.2	4.14	97.2	4.55
40 <sub>Ca</sub> a	40.0	340.3	3.99	94.5	4.62
208 <sub>Pb</sub>	30.3	320.6	5.97	67.3	7.17
208 <sub>Pb</sub> b	30.3	326.6	6.06	68.8	7.14
208 <sub>Pb</sub>	40.0	296.4	5.00	74.6	6.88
208 <sub>Pb</sub> b	40.0	303.5	6.06	77.0	6.76

a) fixed geometry(Va71)

b) fixed geometry(Va74)

and the mean-square radius by

$$r_D^2 = 12 \text{arA}^{1/3} \left[ 1 + \left( \frac{\text{a}\pi}{\text{rA}^{1/3}} \right)^2 \right] \frac{J_{\text{vol}}^C}{J_D^C}$$
 (V-13)

Where  $J_{\text{vol}}^{C}$  and  $J_{D}^{C}$  are the volume integrals for the volume and derivative form, respectively, with  $V_{\text{vol}} = V_{D} = 1$ .

When a combination volume and surface term is used the total volume integral is

$$\frac{J}{A} = \frac{J_{\text{vol}}}{A} + \frac{J_{\text{D}}}{A} \tag{V-14}$$

while the mean-square radius is

$$\langle r^2 \rangle = \langle r_{vol}^2 \rangle_{\overline{J}}^{\overline{J}vol} + \langle r_D^2 \rangle_{\overline{J}}^{\overline{J}D}$$
 (V-15)

The volume integrals and  $\langle r^2 \rangle^{1/2}$  of the present work are tabulated in Table 9.

#### E. Coulomb Correction Term

The charge of the nucleus has the effect of reducing the mean kinetic energy of incident charged particles interacting with the nucleus. Because the local real potential increases with decreasing energy, the effective real potential felt by protons is larger than that for neutrons of the same bombarding energy. This effect is accounted for by adding to the proton potential the Coulomb correction term,  $\Delta V_{\rm C}({\bf r})$ . The real potentials of the Lane formalism for proton and neutron scattering are

$$V^{(n)}(r,E) = (V_{0n} - \gamma E - \epsilon V_1(E)) f(r)$$

$$V^{(p)}(r,E) = (V_{0p}^{-\gamma E + \epsilon V_1(E)}) f(r) + \Delta V_c(r)$$
 (V-16)

where a linear energy dependence is assumed. Assuming a charge symmetric nucleon-nucleon interaction the terms  $V_{0n}$  and  $V_{0p}$  are equal. The subscripts n and p will be left off from here on. If we compare the potentials deduced for scattering from N=Z nuclei( $\varepsilon$ =0) at the same energy we find

$$V^{(p)}(r,E)-V^{(n)}(r,E)=\Delta V_{C}(r)$$
 (V-17)

The Coulomb correction term can now be obtained directly. The derived potentials from scattering over a range of energies can be fitted and these energy dependent potentials determined. In Figure 15 the real well depth from the average geometry is plotted for both neutrons and protons (the average geometry and proton data are from the work of Van Oers, (Va71) for  $^{40}$ Ca and (Va74) for  $^{208}$ Pb). Apart from a dip in the proton potentials near 20 MeV a linear trend is clearly established. The proton potential is  $V^{(p)}(E) = (59.2-0.35E) MeV$ 

v - (E) - (39.2-0.33E) Mev

and the neutron potential is

$$V^{(n)}$$
 (E) = (56.5-0.35E) MeV

where the energy dependence of the neutron potential is constrained to match that of the proton potential. Thus from equation V-17 the Coulomb correction for calcium is

$$\Delta V_c = 2.7 \pm 0.3 \text{ MeV}$$

where the form factor is Woods-Saxon shape with  $R=r_OA^{1/3}$ 

=1.152 $A^{1/3}$ fm and  $a_0$ =0.692fm. The error is estimated by noting that slope change of  $\pm 0.02$  is about the maximum allowed by the data. Using the form of Lane (La 57)

$$\Delta V_{C} = \beta z Z/A^{1/3} \qquad (V-18)$$

we establish the Coulomb correction for protons to be

$$\Delta V_{C} = (0.46 \pm 0.05) \text{ Z/A}^{1/3} \text{MeV}$$
.

In terms of volume integrals we need only change scale since the geometry is fixed. Thus,

$$J_p/A = (494.5-2.92E) \text{MeV fm}^3$$
,  
 $J_p/A = (472.0-2.92E) \text{MeV fm}^3$ ,

and

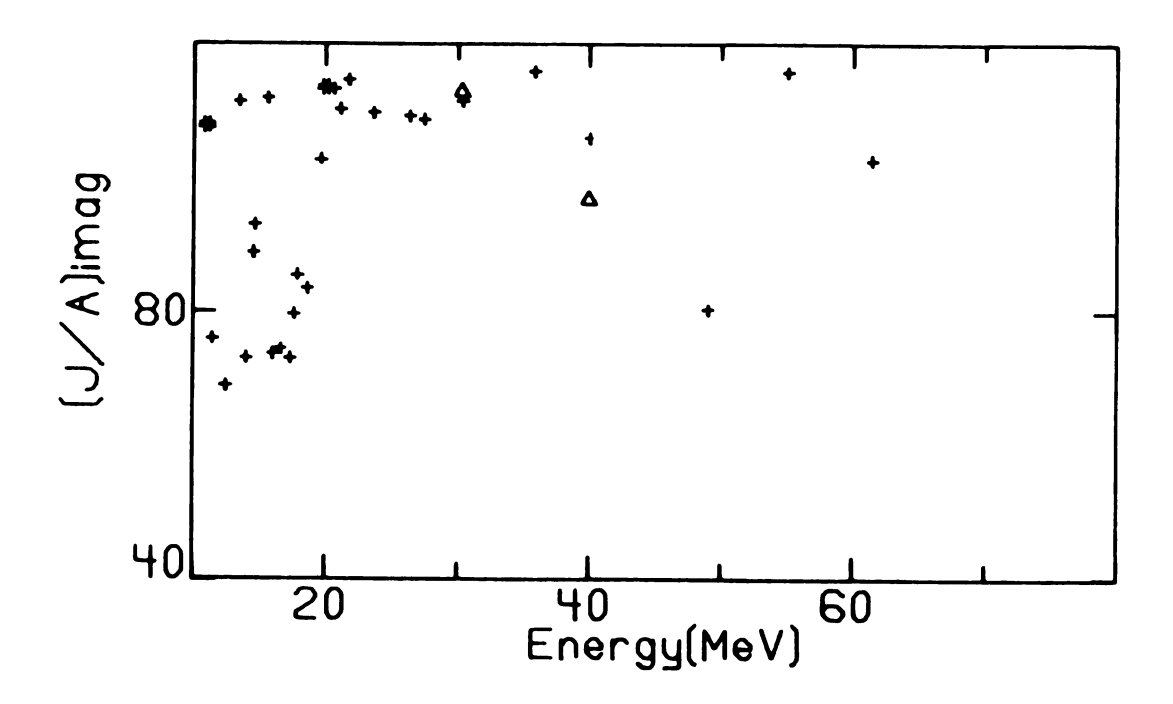
$$J_{\Delta}/A = (3.86 \pm 0.4) Z/A^{1/3} MeV fm^3$$
 . (V-20)

Jeukenne et al. (Je77) have calculated the Coulomb correction in the framework of the Brueckner-Hartree-Fock approximation. They conclude that the standard value (Pe63)

$$\Delta V_{c}^{st} = (0.4Z/A^{1/3}) f(r) MeV$$

is an underestimate. They calculate a 25% larger volume integral than the standard value for  $^{208}\text{Pb}$  at 25 MeV.

Rapaport et al. (Ra77) deduced the same value for  $V_{\rm C}$  as this analysis. They compared the proton data of van Oers to their neutron data, which is also used in the present analysis. Their data covered an energy range of only 15 MeV. The present analysis extends that range to 29 MeV



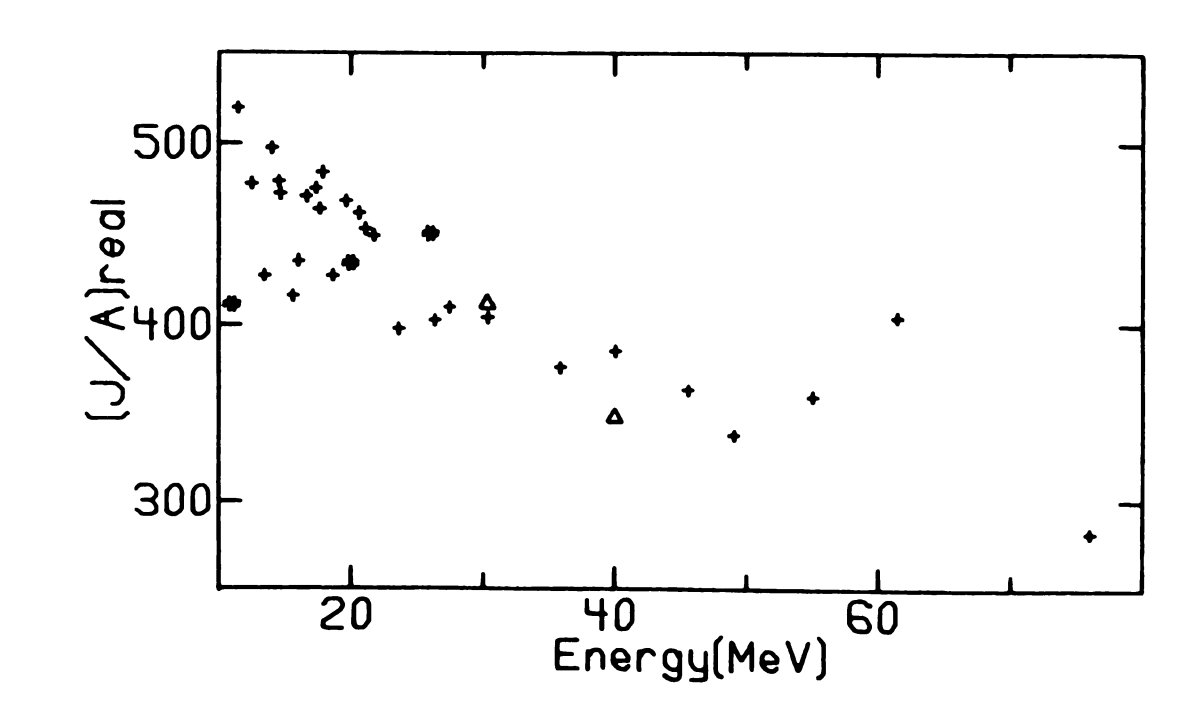
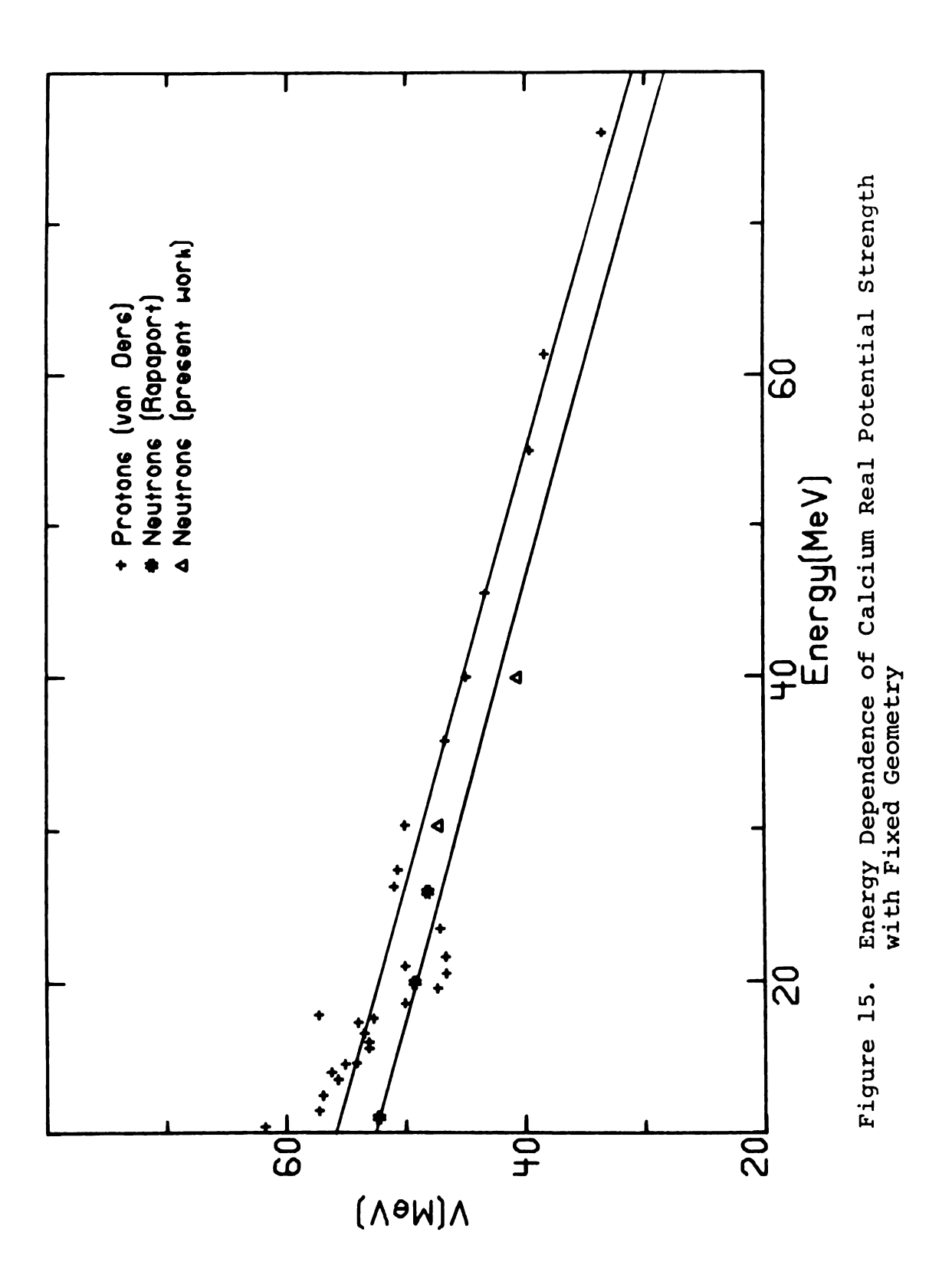


Figure 14. Energy Dependence of Calcium Volume Integrals, Best Fit Values



with the inclusion of higher energy data.

The determination of the Coulomb correction term from linear fits to neutron and proton potentials over a range of energies has certain inherent limitations. A linear energy dependence is assumed from the very start. This appears to be a good assumption, but as in the case for protons on 40 Ca large deviations from linearity are observed. These deviations must be treated individually thus introducing personal judgement errors or bias to the linear fit. All the potentials considered are not derived from data of comparable quality, quantity or content. Different angular ranges are measured for the various angular distributions. Some include polarization while some do not and the experimental uncertainties of the data are not consistant. Assigning errors to potentials based on the quality of the data and the quality of fit is not well understood. It is hoped however that the net effect of all fluctuations and errors will in some average way become small.

If neutron and protons potentials are compared at identical energies, no energy dependence needs to be assumed before extraction of specific terms in the potential. Thus we compared neutron data at 30.3 and 40.0 MeV to existing proton data at the same lab energies. The proton data is reanalysed restricting the angular range to match that of the neutron data. The data of Ridley and Turner (Ri64) for <sup>40</sup>Ca at 30.3 MeV and the data of Blumberg et al. (Bl66) at 40.0 MeV are used. A search procedure similiar

to that used to search on the center of mass neutron data is used to determine proton potentials. The proton data are analysed in terms of the average geometry of van Oers (Va71) and best fit parameters. The volume integrals of these potentials are then averaged and compared to the same averaged potential from the appropriate neutron data. These results are tabulated in Tables 10 and 11 for calcium.

The differences of the volume integrals for calcium are

$$\Delta \frac{J}{A}$$
 (30.3MeV)=10.7MeV fm<sup>3</sup>

$$\Delta \frac{J}{A}$$
 (40.0 MeV)=32.5MeV fm<sup>3</sup> .

In this case  $\Delta J = J_{\Delta}$ . From the theoretical considerations  $J_{\Delta}$  should be energy independent (Je74, Je77). Thus we take the average value of  $\Delta J$  from the above to give

$$\frac{J_{\Delta}}{A} = (21.6 \pm 7) \,\text{MeV fm}^3$$

for <sup>40</sup>Ca. Using the form of equation V-18

$$\frac{J_{\Delta}}{\Delta} = (3.69 \pm 1.2) Z/A^{1/3} MeV \text{ fm}^3.$$
 (V-21)

This value is in good agreement with the value extracted from the linear fits. The average of the two determinations yields

$$\frac{J_{\Delta}}{A}$$
 = (3.78±0.4)  $Z/A^{1/3}$ MeV fm<sup>3</sup> . (V-22)

Table 10.  $J/A^{(a)}$  for protons and neutrons on Calcium.

E<sub>nucleon</sub>=30.3 MeV

	Fixed geometry (b)	Best fit	Average
$\frac{J_p}{A}$ real	405.1	424.2	414.7
$\frac{J_n}{A}$ real	395.3	412.7	404.0
$\frac{J_p}{A} - \frac{J_n}{A}$ real	9.8	11.5	10.7
$\frac{J_p}{A}$ imag	104.3	103.0	103.7
$\frac{J_n}{A}$ imag	114.0	113.2	113.6
$\frac{J_p}{A} - \frac{J_n}{A}$ imag	-9.7	-10.2	-9.9

a) all J/A units are MeV  $fm^3$ 

b)  $r_R=1.152$  fm,  $a_R=0.692$  fm,  $r_I=1.309$  fm,  $a_I=0.549$  fm

Table 11.  $J/A^{(a)}$  for protons and neutrons for Calcium.

E<sub>nucleon</sub>=40. MeV

	Fixed Geometry (b)	Best fit	Average
$\frac{J_p}{A}$ real	374.0	379.4	376.7
$\frac{J_n}{A}$ real	340.3	348.0	344.2
$\frac{J_p}{A} - \frac{J_n}{A}$ real	33.7	31.4	32.5
$\frac{J_p}{A}$ imag	102.9	102.2	102.6
$\frac{J_n}{A}$ imag	94.5	97.2	95.9
$\frac{J_p}{A} - \frac{J_n}{A}$ imag	8.4	5.0	6.7

a) all J/A units are MeV  $fm^3$ 

b)  $r_R=1.152$  fm,  $a_R=0.692$  fm,  $r_I=1.309$  fm,  $a_I=0.549$  fm

In terms of the average calcium geometry of van Oers this term is

$$\Delta V_{C} = (.452 \pm 0.05) Z/A^{1/3} MeV$$
 . (V-23)

#### F. Isovector Term

We have already assumed a charge symmetric nucleon-nucleon interaction i.e.  $V^{\mathrm{pp}}=V^{\mathrm{nn}}$ . However the nucleon-nucleon interaction is not charge independent i.e.  $V^{\mathrm{pp}}\neq V^{\mathrm{pn}}$ . This effect is described by the isovector strength  $V_1$  of the Lane Model potential. This term is important not only in proton and neutron scattering in terms of a global OMP but also in charge exchange reactions.

If we consider the case for  $N\neq Z$  nuclei, such as  $^{208}\text{Pb}$ , we see from equation V-16 that for the same incident energy,

$$v^{(p)}(r,E)-v^{(n)}(r,E)=2\varepsilon V_1(E) f(r)+\Delta V_c(r)$$
. (V-24)

The nuclear asymmetry ( $\epsilon$ ) is roughly Z dependent. Since the Coulomb correction term is also Z dependent, even if we consider a wide range of nuclei, unless we have prior knowledge of  $\Delta V_{\rm C}$ , the isospin dependence  $V_{\rm 1}(E)$  can not be directly extracted.

In an analysis similar to the one for  $^{40}$ Ca, van Oers et al. have compiled and analysed proton scattering data for  $^{208}$ Pb(Va74). Again best fit and average geometry potentials are determined. In Figure 16 the real potential depth with fixed geometry ( $r_0$ =1.183fm,  $a_0$ =0.724fm) as well as the deduced linear fits are plotted for neutron and proton data.

In terms of volume integrals, the proton potential is (Ra78)

$$\frac{J_p}{A} = (485.7-2.52E) \text{MeV fm}^3$$
.

From a linear least squares fit to the neutron data we find the neutron potential to be

$$\frac{J_n}{A}$$
 = (380.2-1.88E)MeV fm<sup>3</sup>.

Writing equation V-24 in terms of volume integrals we have

$$\frac{J_p}{A} - \frac{J_n}{A} = 2\varepsilon \frac{J_1}{A} + \frac{J_{\Delta}}{A} \qquad (V-25)$$

From equation V-22 the volume integral of the Coulomb correction term for  $^{208}$ Pb is 52.3 MeV fm<sup>3</sup>. Thus

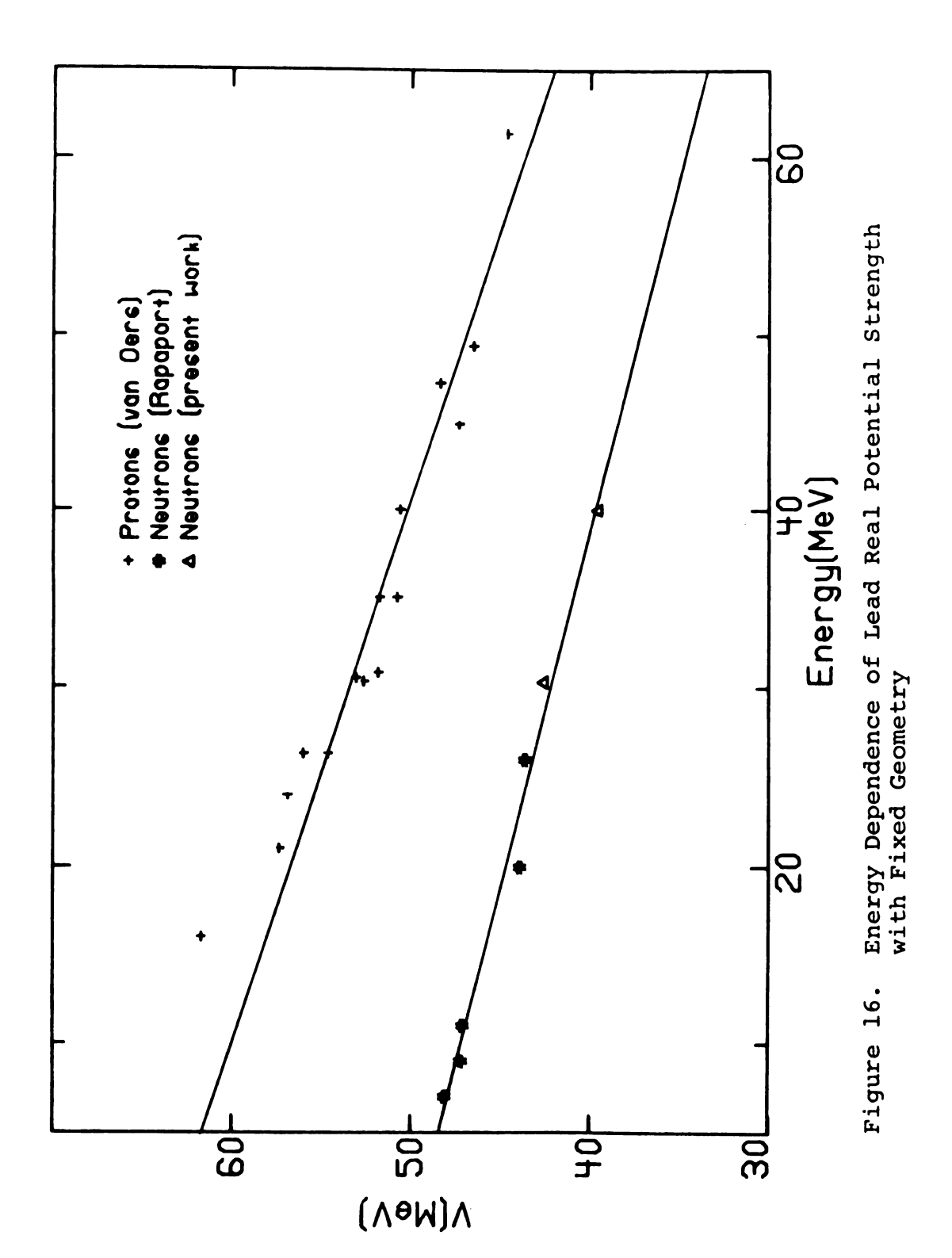
$$\frac{J_1}{A}$$
 = (125.8-1.51E) MeV fm<sup>3</sup> . (V-26)

In contrast to the calcium case the real volume integrals of the best fit potentials do show a well defined linear energy dependence as shown in Figure 17. A least squares fit to the proton data yields

$$\frac{J_p}{A}$$
 = (516.4-3.28E)MeV fm<sup>3</sup>.

The neutron volume integrals, which include the present measurements at 30.3 and 40 MeV, the data of Rapaport et al. (Ra78) at 7, 9, 11, 20, and 26 MeV and data from the tabulation of Perey (Pe76) are best fitted by

$$\frac{J_n}{A}$$
 = (407.5-2.85E) MeV fm<sup>3</sup>.



This yields for the isovector volume integral

$$\frac{J_1}{A}$$
 = (133.8-1.02E) MeV fm<sup>3</sup>. (V-27)

The density of neutron data points is not uniform but rather is concentrated at low energies. To make the neutron potential more dependent on the higher energy data, the data of Perey is left out. Then a least squares fit for the real neutron volume integral gives

$$\frac{J_n}{A}$$
 = (397.0-2.48E) MeV fm<sup>3</sup>.

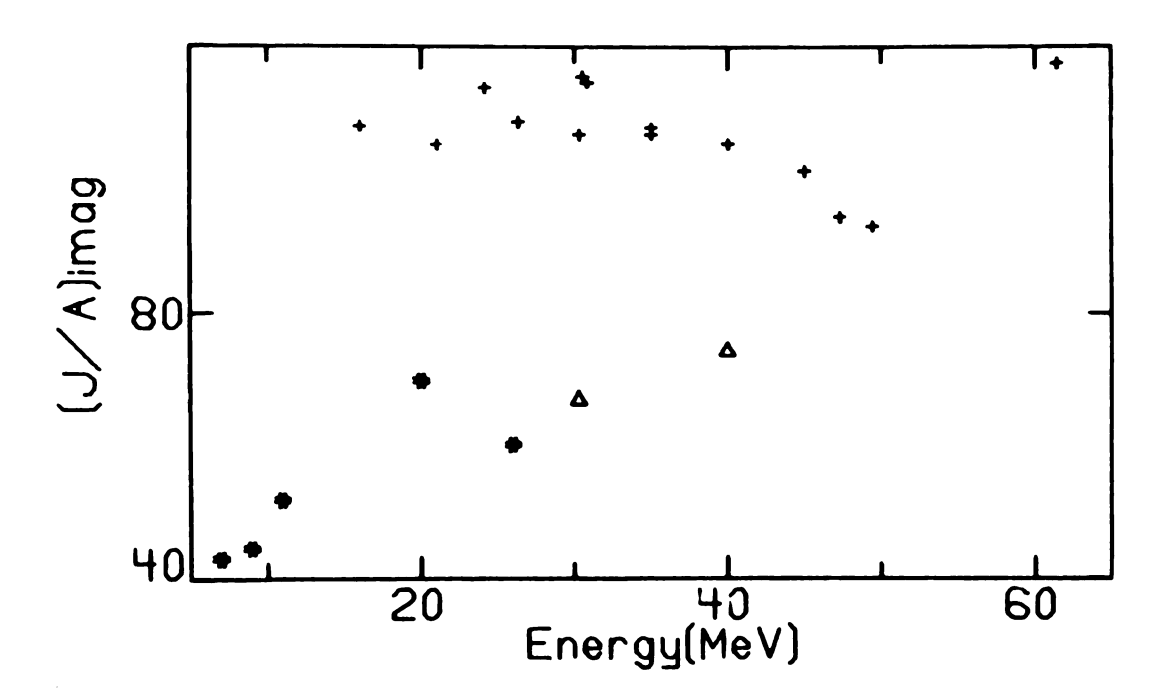
This neutron potential yields an isovector volume integral of

$$\frac{J_1}{A}$$
 = (158.6 -1.9E) MeV fm<sup>3</sup>. (V-28)

These three determinations of  $J_1/A$  yield different results. As a compromise we take the average value,

$$\langle J_1/A \rangle = (139.4-1.48E) \text{ MeV fm}^3$$
 (V-29)

The proton data on <sup>208</sup>Pb of Ridley and Turner (Ri64) at 30.3 MeV and the data of Blumberg et al. (Bl66) at 40 MeV were reanalysed restricting the angular range to match the neutron data as was done for calcium in section V-E. The results of the proton searches are tabulated in Table 12 for 30.3 MeV and in Table 13 for 40 MeV. From this analysis we find the isovector strength at 30.3 and 40 MeV to be



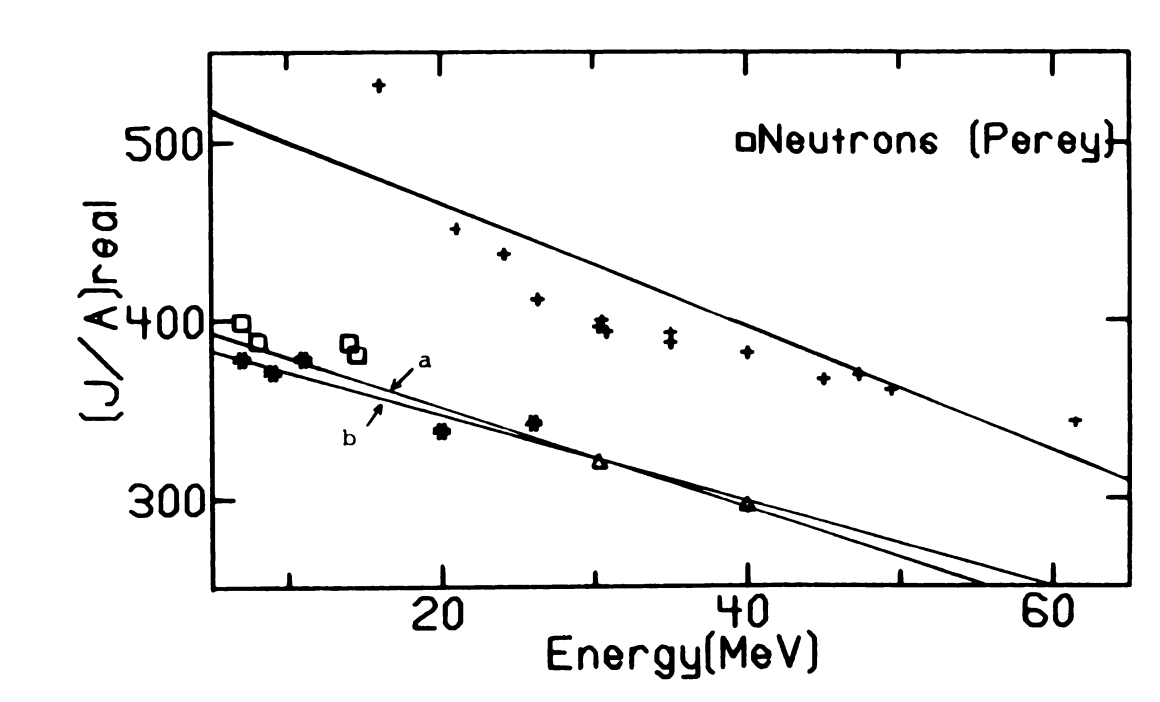


Figure 17. Energy Dependence of Lead Volume Integrals, Best Fit Values, symbols same as Figure 16 a)  $J_n/A=(407.5-2.85E)\,\text{MeV}$  fm 3 b)  $J_n/A=(397.0-2.48E)\,\text{MeV}$  fm

$$J_1/A(30.3 \text{ MeV}) = 86.9 \text{ MeV fm}^3$$
  
 $J_1/A(40.0 \text{ MeV}) = 73.2 \text{ MeV fm}^3$ .

Thus if we now assume a linear energy dependence we find that

$$J_1/A = (129.4-1.40E) \text{ MeV fm}^3$$
 . (V-30)

This value is in good agreement with the value (equation V-29) derived from the fitted potentials. Taking the average (V-29 and V-30) we find

$$J_1/A = (134.4\pm13) - (1.44\pm0.08) E \text{ MeV fm}^3$$
. (V-31)

The error is that due to the error in the Coulomb Correction.

In terms of the average geometry of van Oers, this isovector potential strength is

$$V_1 = (17.5-0.19E) \text{ MeV}$$
 (V-32)

The present determination yields a value about 20% smaller than the values reported by other authors (Ra79, Pa76, Be69, Ca75). However the energy dependence determined by Rapaport et al. (Ra79) and by Patterson et al. (Pa76) agrees very well with the energy dependence determined by the present work.

## G. Imaginary Potentials

The imaginary part of the OMP describes the effect of all the non-elastic interactions of the incident particle with the target nucleus. This potential requires a combination of volume and surface form factors as discussed in section I-B.

Table 12.  $(J/A)^{(a)}$  for protons and neutrons on Lead.  $E_{\text{nucleon}} = 30.3 \text{ MeV}$ 

	Fixed geometry (b)	Best fit	Average
$\frac{J_p}{A}$ real	411.4	412.6	412.0
$\frac{J_n}{A}$ real	326.6	320.6	323.6
$\frac{J_p}{A} - \frac{J_n}{A}$ real	84.8	92.0	88.4
$\frac{J_p}{A}$ imag	110.0	104.2	107.1
$\frac{J_n}{A}$ imag	68.6	67.3	68.0
$\frac{J_p}{A} - \frac{J_n}{A}$ imag	41.4	36.9	39.1

a) all J/A units are MeV  $fm^3$ 

b)  $r_R=1.183$  fm,  $a_R=0.724$  fm,  $r_I=1.273$  fm,  $a_I=0.699$  fm

Table 13. J/A (a) for protons and neutrons on Lead.

E<sub>nucleon</sub>=40. MeV

	Fixed geometry (b)	Best fit	Average
$\frac{J_p}{A}$ real	389.9	375.2	382.6
$\frac{J_n}{A}$ real	303.5	296.4	300.0
$\frac{J_p}{A} - \frac{J_n}{A}$ real	86.4	78.8	82.6
$\frac{J_p}{A}$ imag	107.8	104.8	106.3
$\frac{J_n}{A}$ imag	77.0	74.6	75.8
$\frac{J_p}{A} - \frac{J_n}{A}$ imag	30.8	30.2	30.5

a) all J/A units are MeV  $fm^3$ 

b)  $r_R=1.183$  fm,  $a_R=0.724$  fm,  $r_I=1.273$  fm,  $a_I=0.699$  fm

The total imaginary volume integrals for scattering from <sup>40</sup>Ca are shown in Figure 14 and the surface and volume potentials of the fixed geometry for <sup>40</sup>Ca are shown in Figure 18. We notice in both Figures that there is no systematic difference between the proton and neutron potentials.

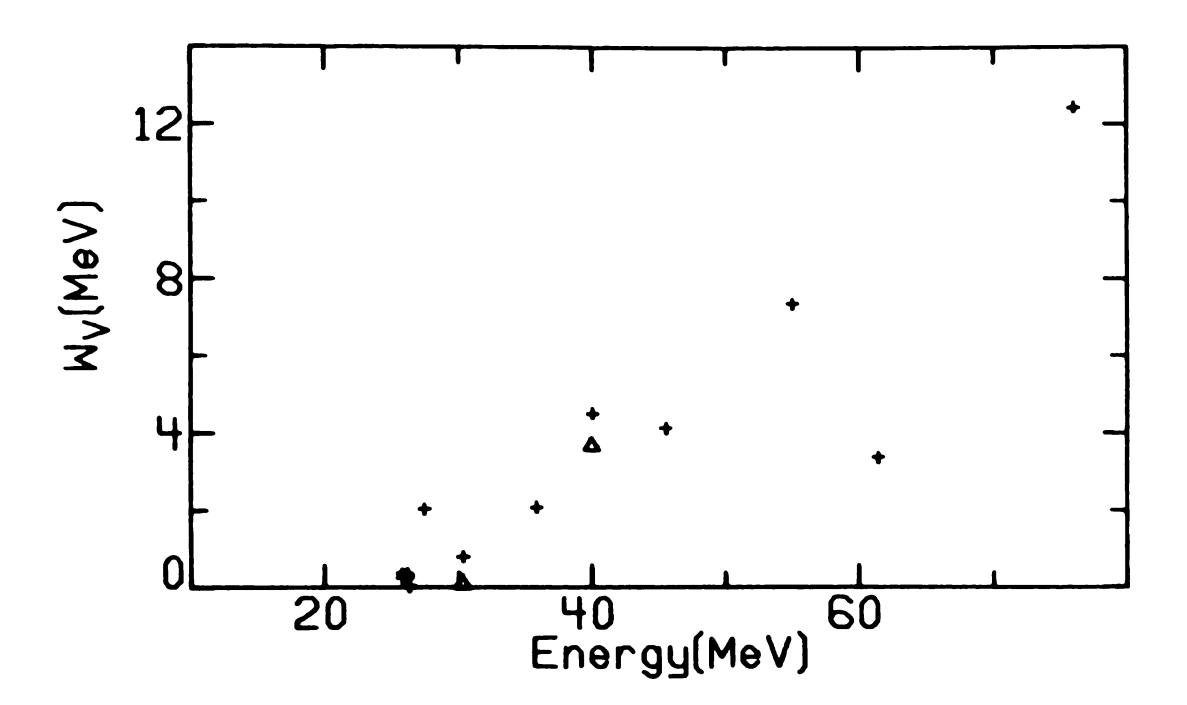
The reanalysed proton data yield a negative value for  $\Delta J_{imag}(\Delta J = J_p - J_n)$  at 30 MeV (Table 10) and a positive value for  $\Delta J_{imag}$  at 40 MeV (Table 11). We conclude that the imaginary Coulomb correction is very small for Ca.

The van Oers proton data was analysed using a Gaussian form factor for the imaginary surface term while the neutron data were analysed using a Woods-Saxon derivative form factor. The derivative Woods Saxon is chosen to have the same width at half maximum as the Gaussian. Results obtained with the Gaussian surface potential replaced by a derivative Woods-Saxon were determined by van Oers to be very similiar (Va71). Rapaport et al. find the two potentials to be not very different (Ra77 and reference therein).

In the analysis by van Oers et al. for protons on lead (Va74) a derivative Woods-Saxon form factor is used instead of a Gaussian. Figure 17 shows the imaginary volume integral for protons and neutrons. The neutron volume integral is increasing approximately linearly with increasing energy. The proton volume integrals are decreasing slightly with energy. Jeukenne et al. (Je77) have calculated the

imaginary Coulomb correction for <sup>208</sup>Pb in the energy range up to 75 MeV. They find this term to be negative, nonlinear with its magnitude approaching zero with increasing energy. If this term were to be subtracted from the proton volume integral the trend would be more nearly linear and decreasing with increasing energy. However untill the imaginary Coulomb correction is better known for 208Pb an accurate determination of the imaginary isovector strength will not be possible. Shown in Figure 19 are the surface and volume components of the imaginary potential using the fixed geometry of van Oers (Va74). Here we see that the strength of the volume term is nearly the same for protons and neutrons. The major difference between the proton and neutron potentials is in the surface contribution. energies above 20 MeV there is a linear decrease in surface strength with protons and neutrons having approximately the same slope.

For protons and neutrons of the same bombarding energy incident on <sup>208</sup>Pb there is additional surface absorption of the protons, perhaps due to the additional reaction mechanism (Coulomb excitation) available to protons.



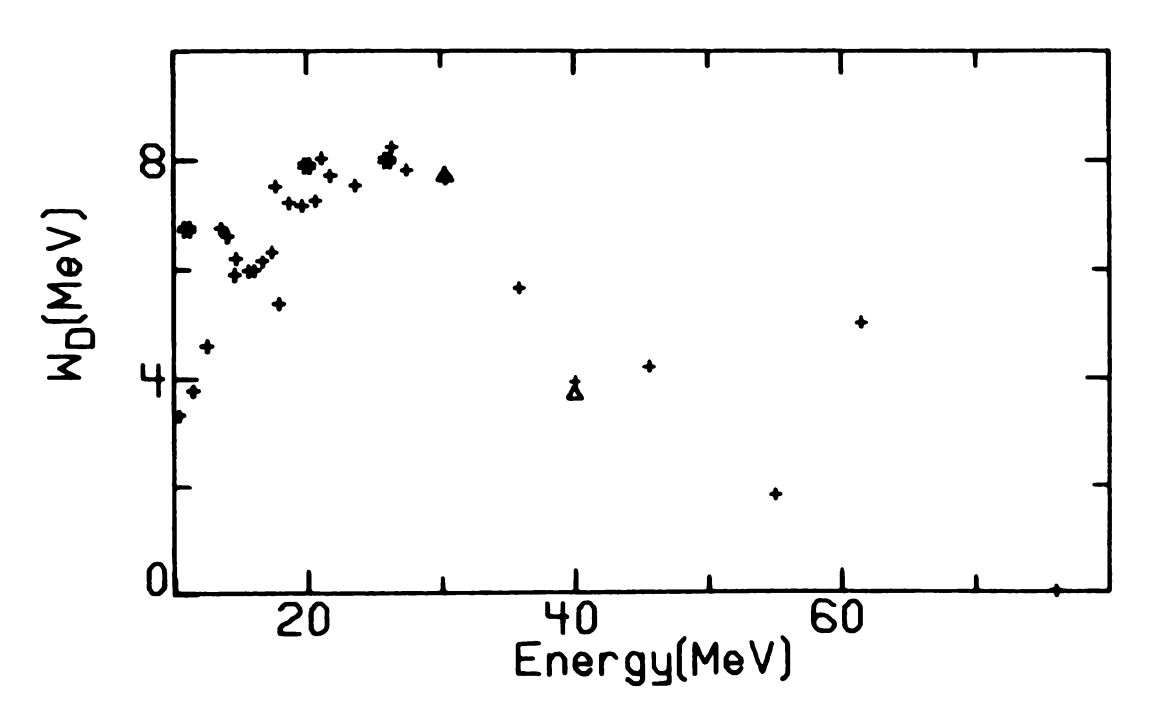
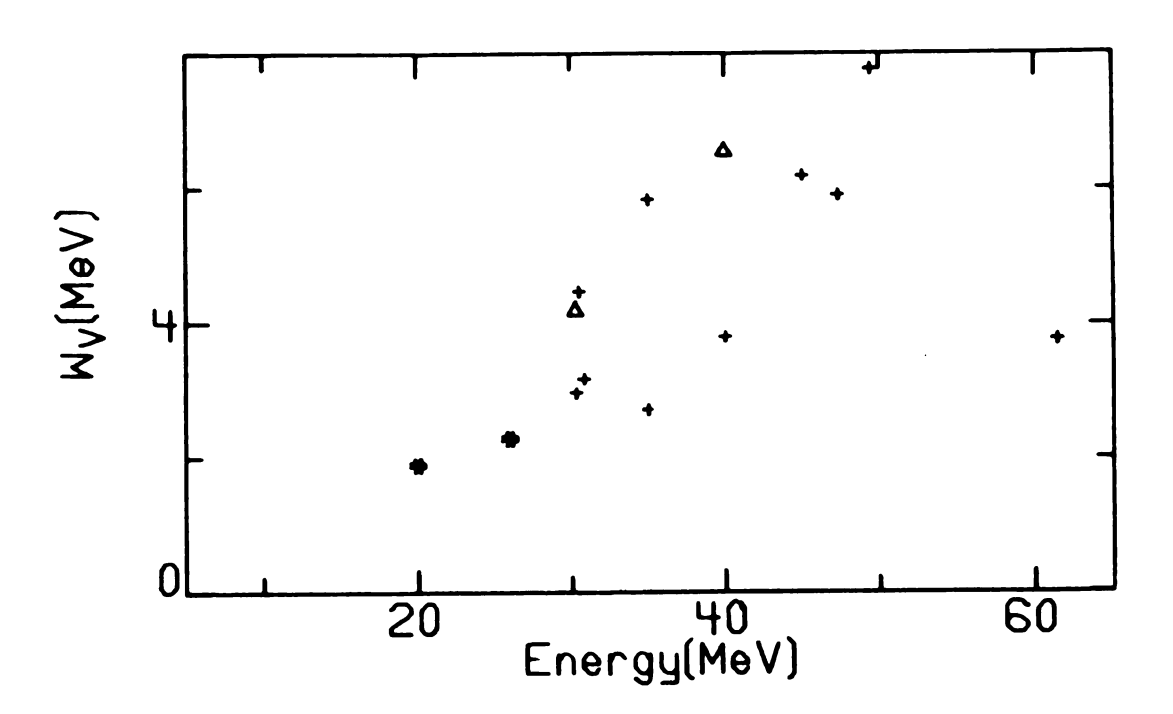


Figure 18. Energy Dependence of Calcium Imaginary Potential Strength with Fixed Geometry



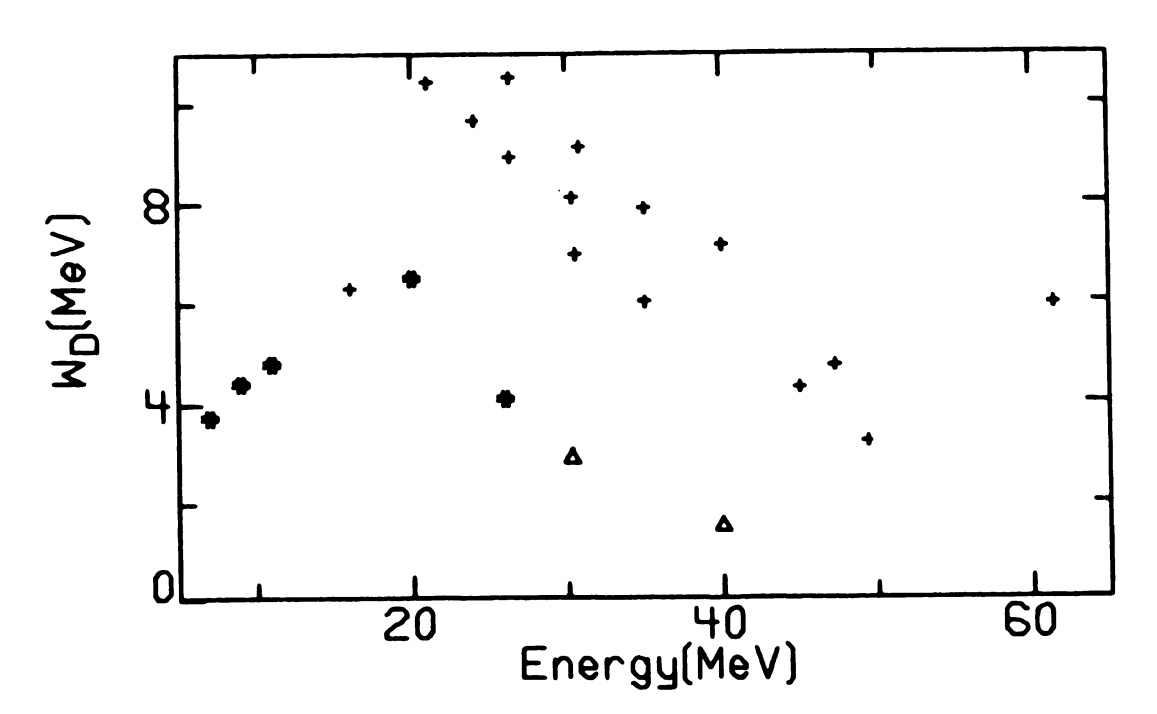


Figure 19. Energy Dependence of Lead Imaginary Potential Strength with Fixed Geometry

## VI. Summary

Apparatus to accurately measure elastic scattering angular distributions for 24-42 MeV neutrons is developed. A monoenergetic neutron beam is produced using the reaction  $^{7}$ Li(p,n) $^{7}$ Be(g.s.+0.429 MeV). The neutrons are scattered from targets of  $^{12}$ C,  $^{28}$ Si,  $^{32}$ S,  $^{40}$ Ca, and  $^{208}$ Pb. The scattering angle is varied using the MSU beam swinger, thus allowing production target and beam dump to be in a different room than the neutron detectors. The scattered neutrons are detected by liquid organic scintillator detectors and energy analysed by the time-of-flight technique. Detector gain is monitored during each run by feeding a constant photon source directly to each detector. A monitor detector measures the direct neutron flux from the <sup>7</sup>Li(p,n) <sup>7</sup>Be reaction. Relative cross section errors range from 2% to 5% over most of the angular range. Absolute normalization errors are <3%.

The data are analysed using a standard Optical Model potential. Calculated cross sections are smeared by a Monte Carlo routine to account for multiple scattering, finite angle and attenuation effects and then compared to the experimental cross sections. For  $^{40}$ Ca and  $^{208}$ Pb both best fit and fixed geometry potentials are deduced. Already existing proton data on  $^{40}$ Ca and  $^{208}$ Pb at 30.3 and

40 MeV are reanalysed using the same procedure as was used for the neutron data. The angular range of the proton data was restricted to match that of the neutron data.

Comparison of proton and neutron potentials for <sup>40</sup>Ca, with the neutron energy dependence constrained to match that of the proton data, yields the volume integral of the Coulomb correction term. Comparison of the reanalysed proton potential to the deduced neutron potentials at 30.3 MeV and at 40 MeV yields an average Coulomb correction term for <sup>40</sup>Ca. Taking the average of these two determinations of the Coulomb correction term and parameterizing in the standard way we find

$$J_{\Lambda}/A = (3.78 \pm 0.4) Z/A^{1/3} \text{ MeV fm}^3$$
.

In terms of the average geometry of the proton potential for  $^{40}$ Ca (r<sub>R</sub>=1.152 fm, a<sub>R</sub>=0.692 fm) we find

$$\Delta V_{C} = (0.45 \pm 0.05) Z/A^{1/3} MeV.$$

Both the fixed geometry and best fit volume integrals of the proton and neutron potentials for <sup>208</sup>Pb are compared, each fit with an independent energy dependence. Using the Coulomb correction term determined above, the isovector term is deduced. Comparison of the reanalysed proton and neutron potentials at 30.3 MeV and at 40 MeV yield an energy dependent isovector strength. The average value of the volume integral is deduced to be

$$J_1/A = (134.4\pm13) - (1.44\pm0.08) E \text{ MeV fm}^3$$
.

In terms of the average geometry for lead ( $r_R$ =1.183 fm,  $a_R$ =0.724 fm) we find the isovector strength to be

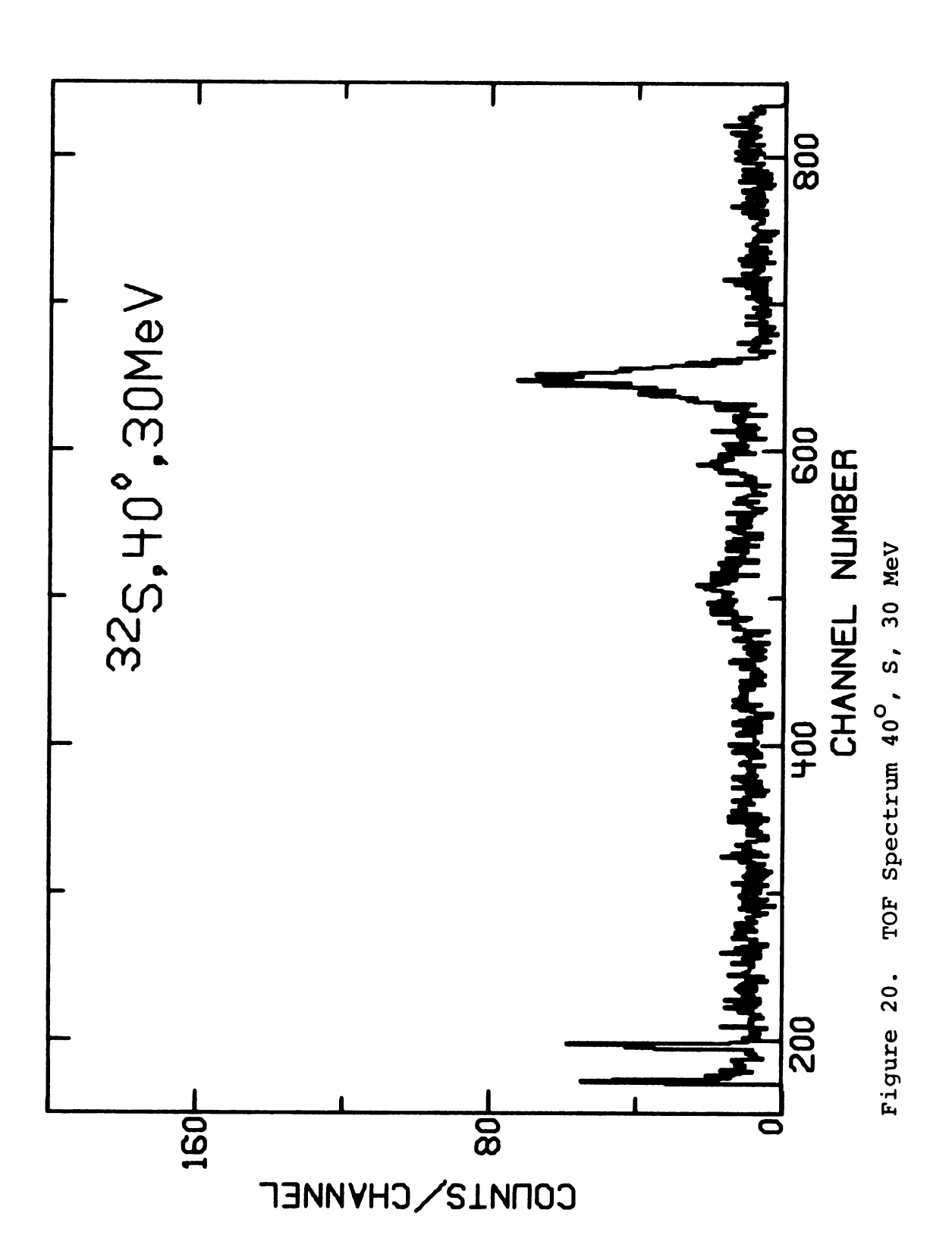
$$V_1 = (17.5 \pm 1.7) - (0.19 \pm 0.02) E \text{ MeV}.$$

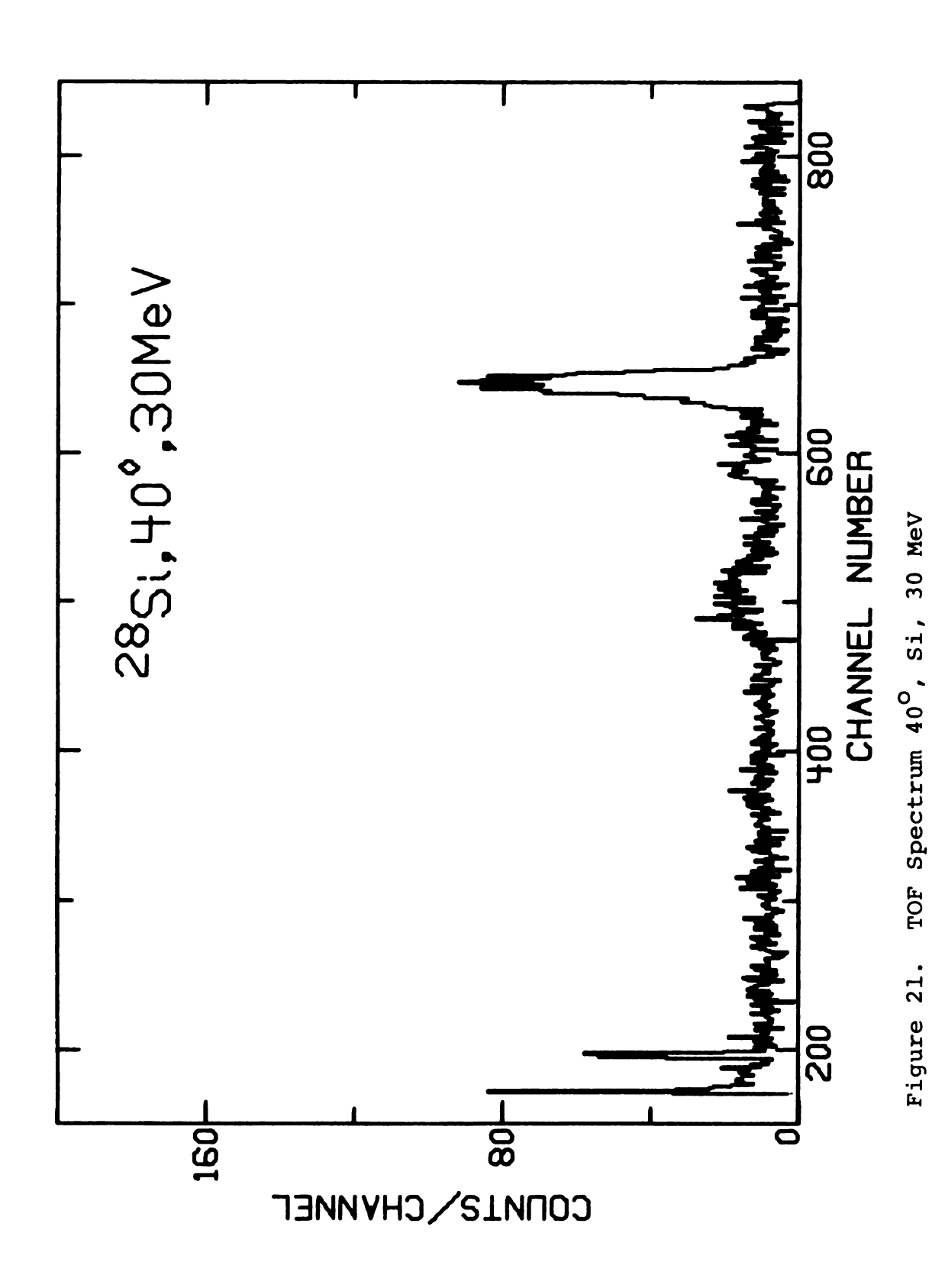
#### APPENDIX

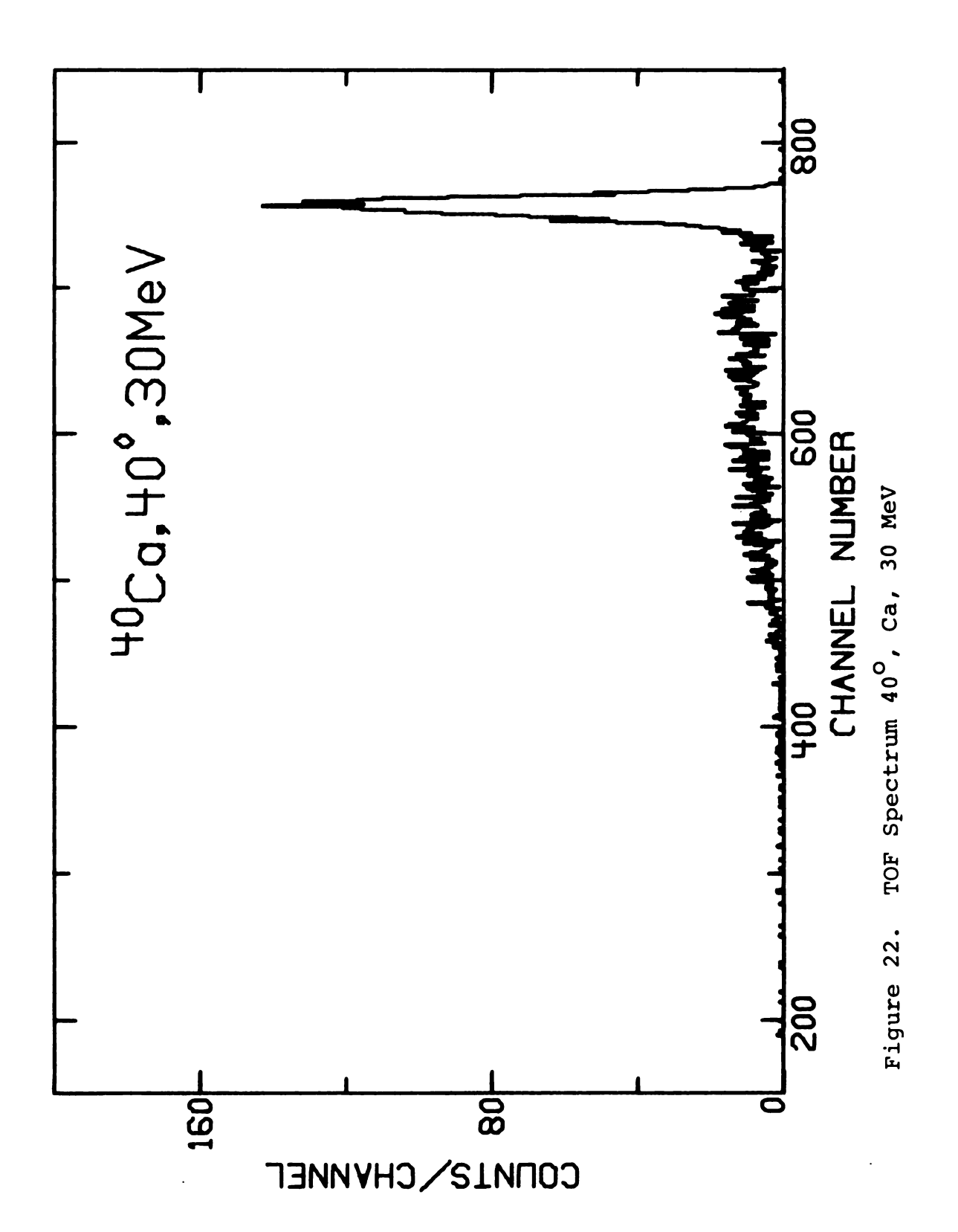
# Tabulated and plotted data

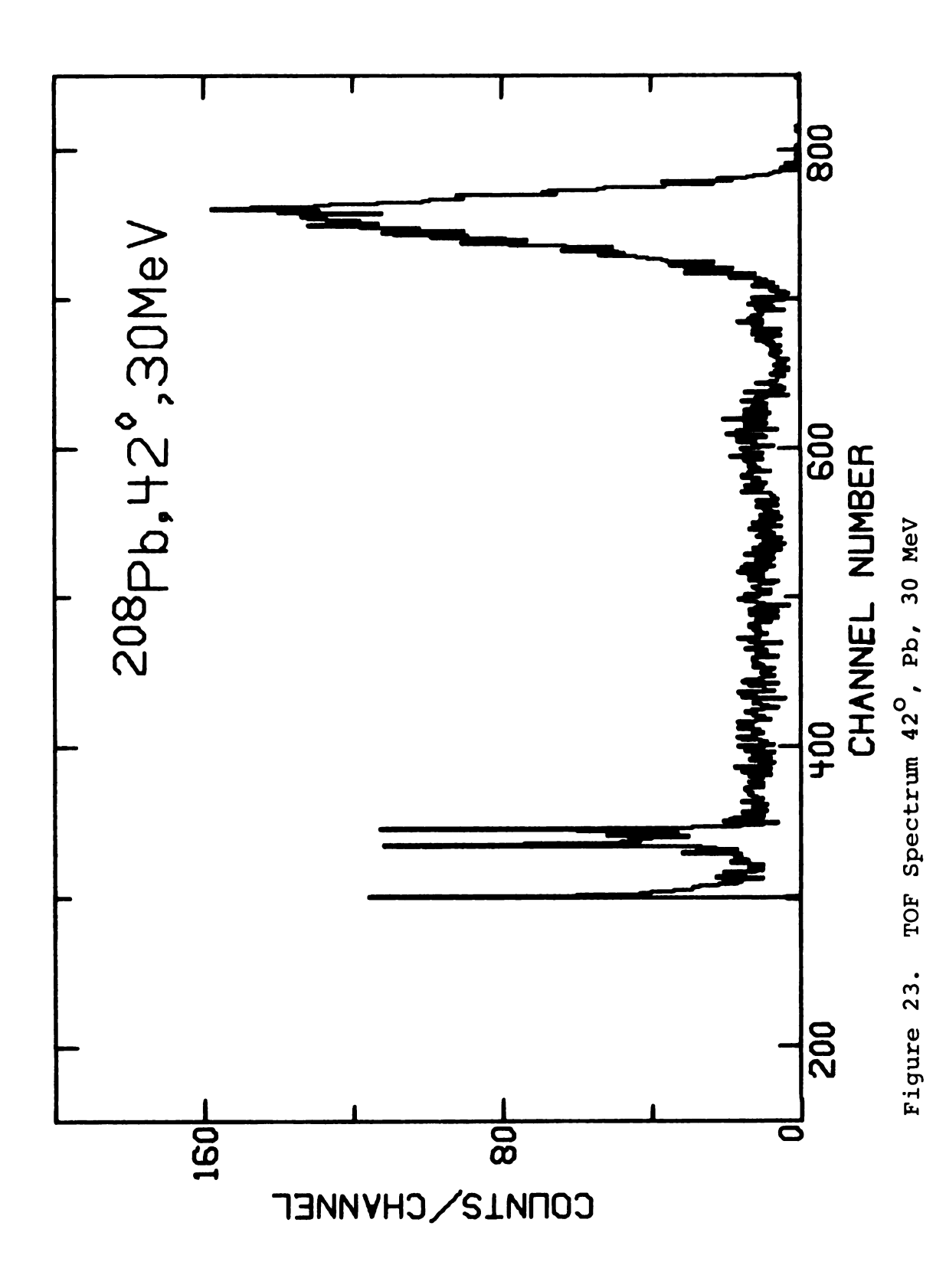
TOF spectra are target in spectra only. Experimental cross sections are deduced using equation IV-5 and are uncorrected for multiple scattering, attenuation and finite angle effects. These are tabulated under the heading Uncorrected Laboratory in Table 14. Errors for the experimental cross sections are relative errors only as listed in Table 5. Center of Mass cross sections are corrected for multiple scattering, attenuation and finite angle effects. These are tabulated under the heading Corrected Center of Mass in Table 14. Errors for corrected center of mass cross sections include relative errors and unfolding errors.

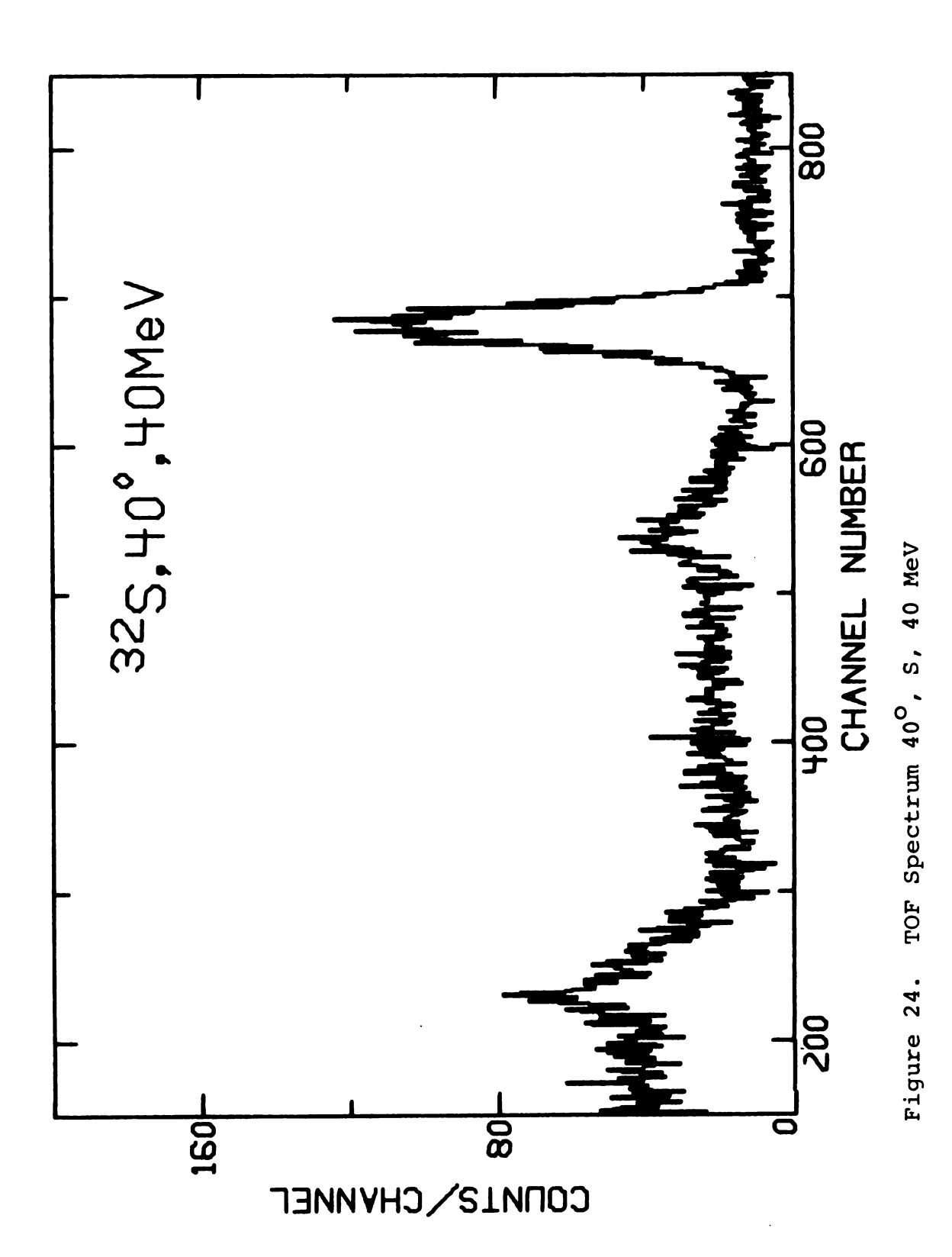
C.M. cross sections for <sup>40</sup>Ca and <sup>208</sup>Pb are deduced from "best fit" parameters. There is an additional normalization error for Experimental and Center of Mass cross sections of 2.6%.

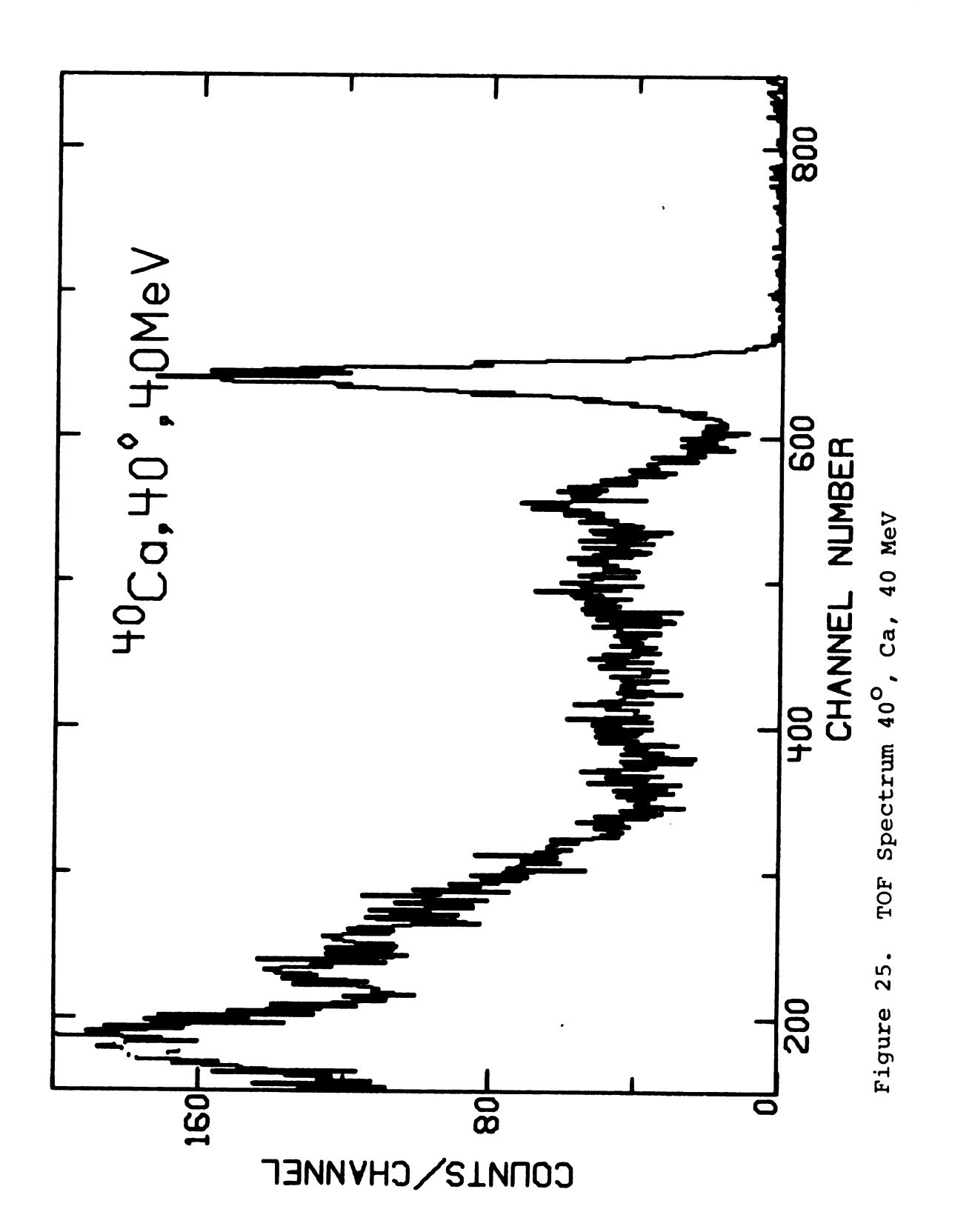


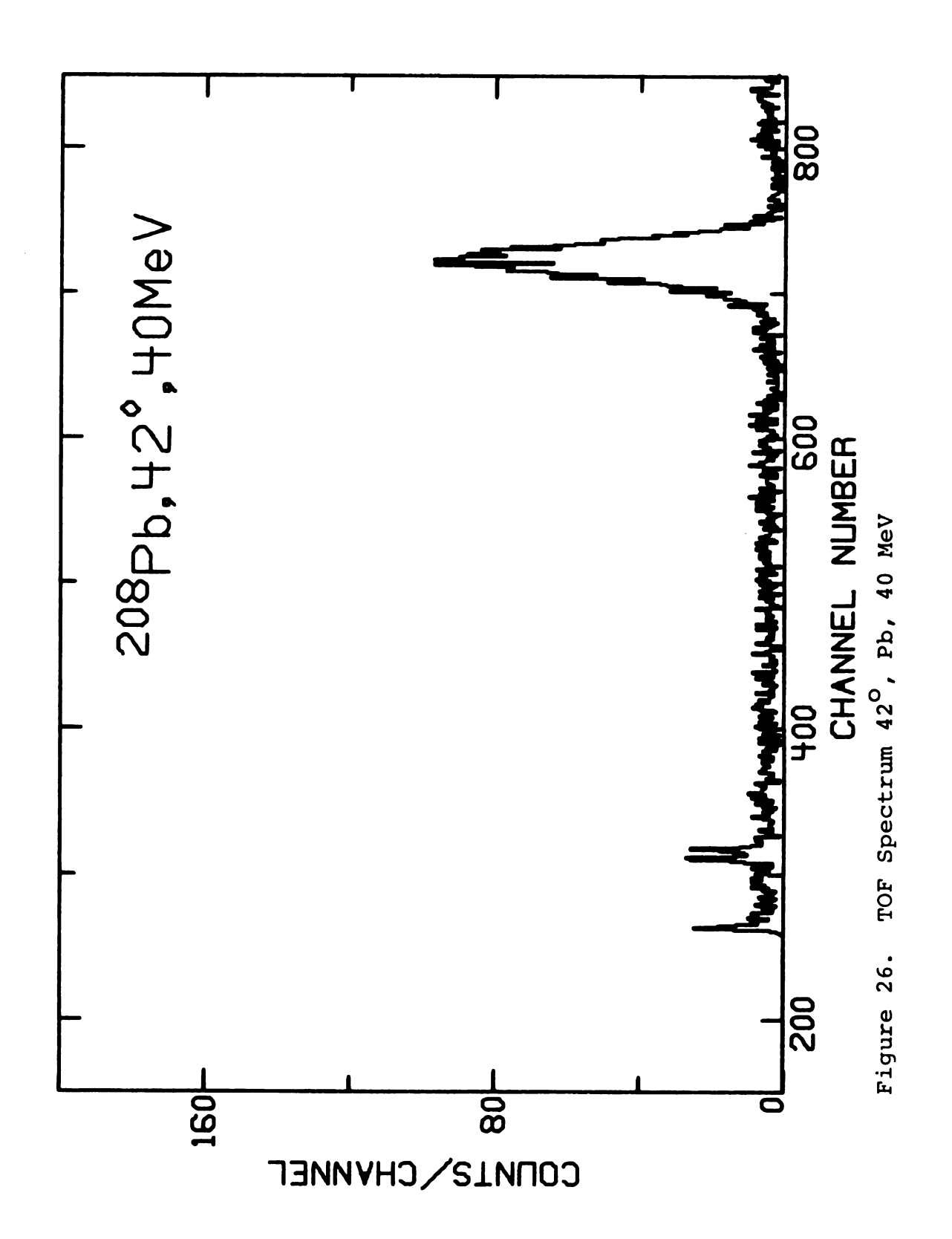


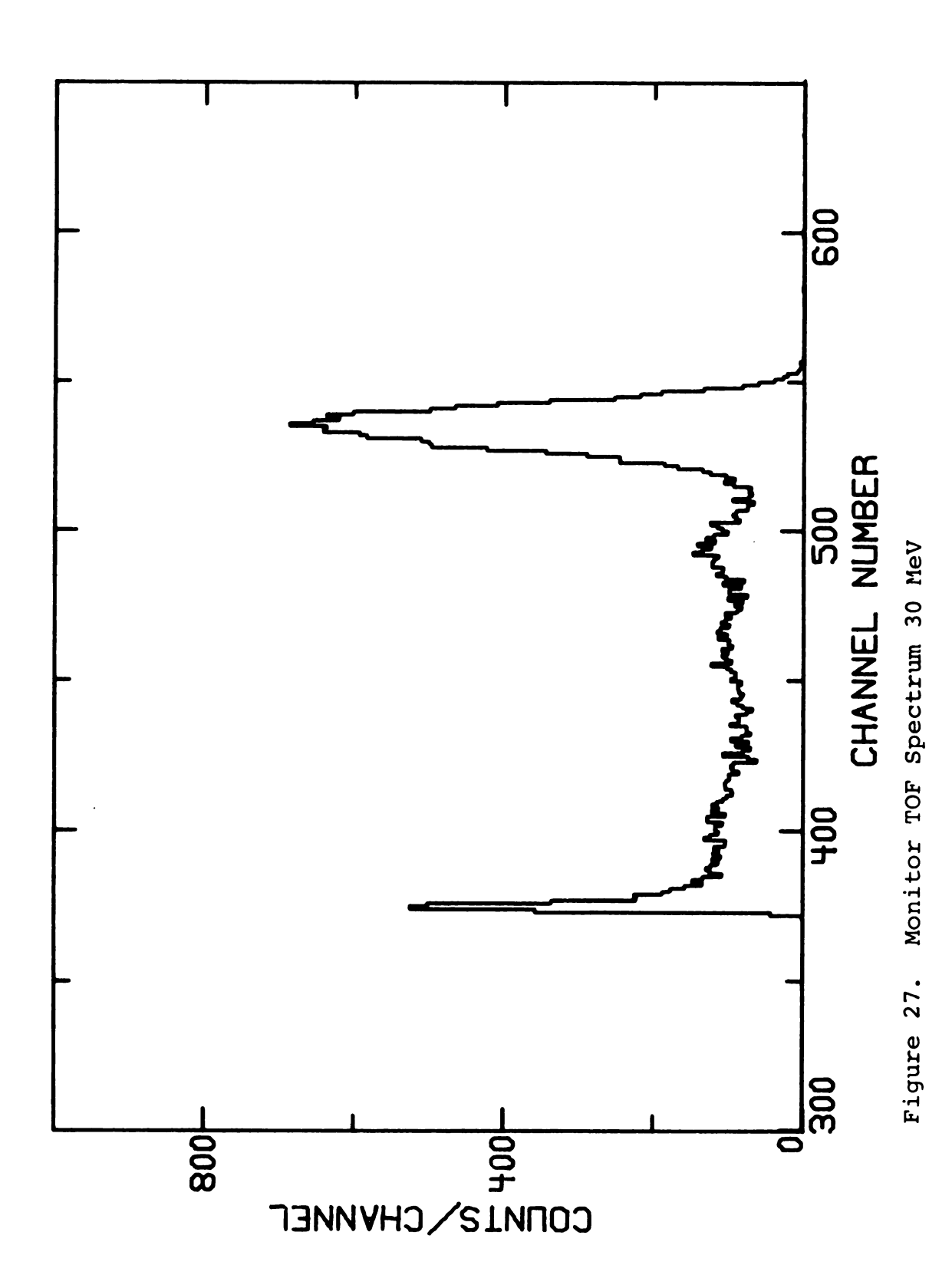


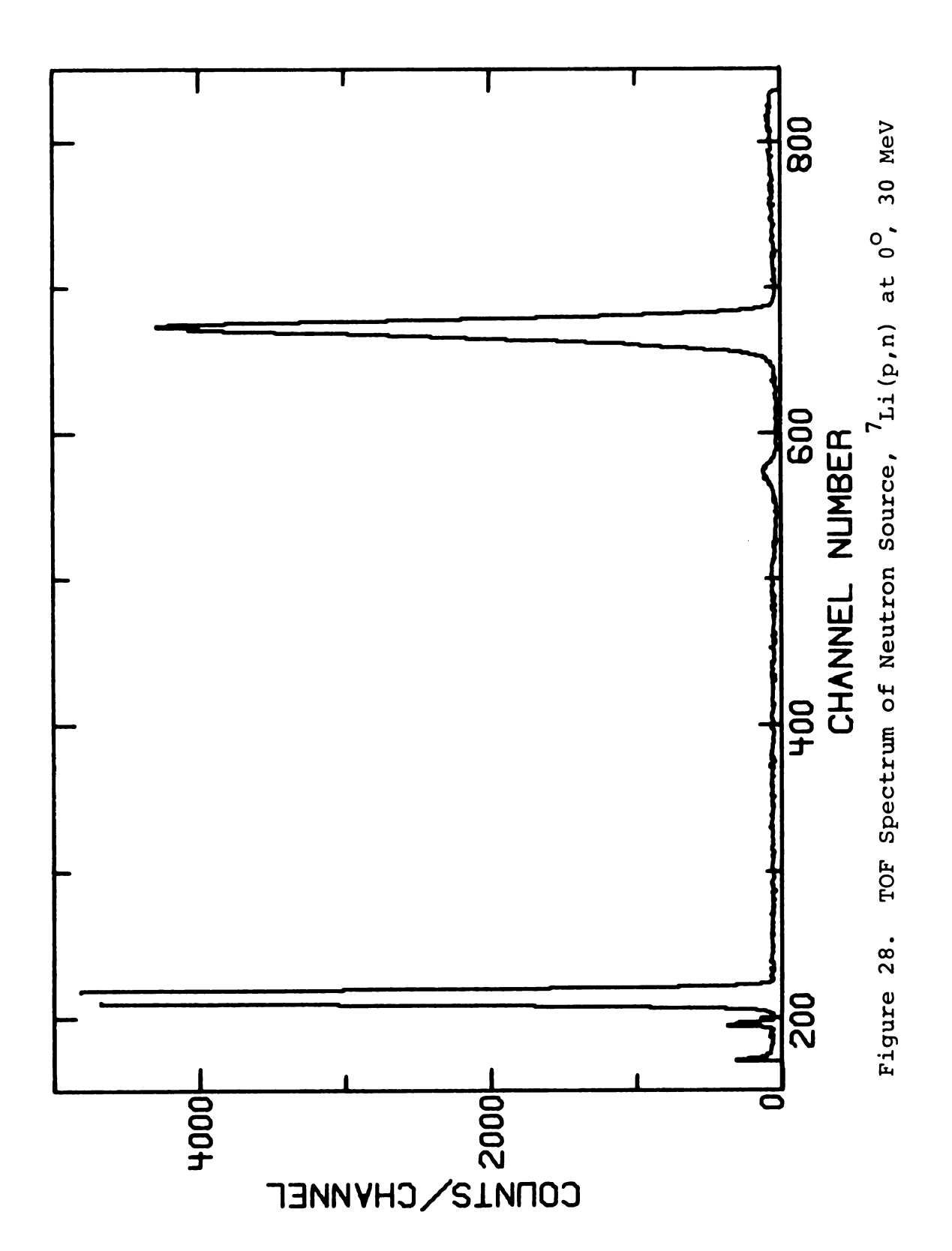












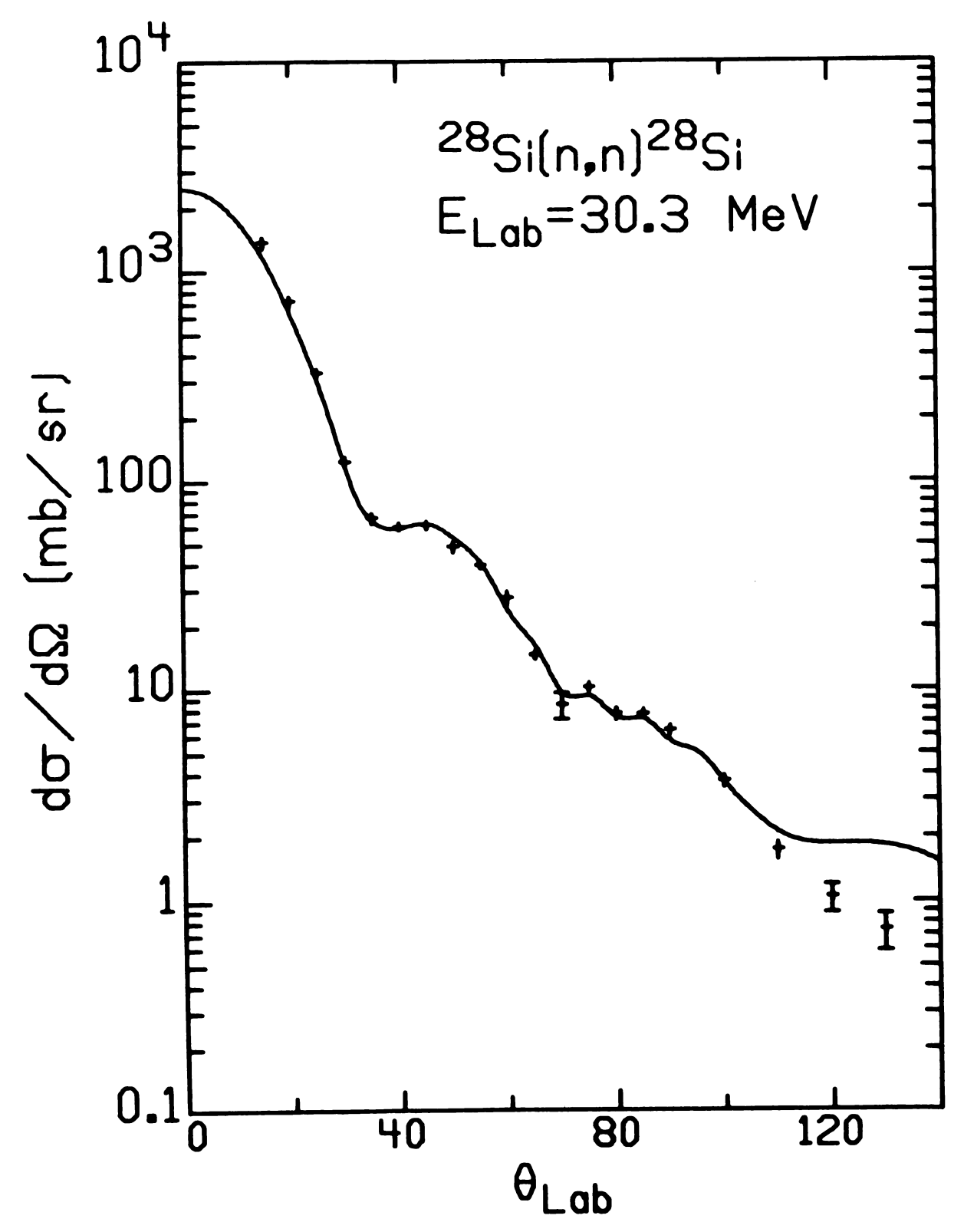


Figure 29. Laboratory Cross Section, <sup>28</sup>Si, 30 MeV

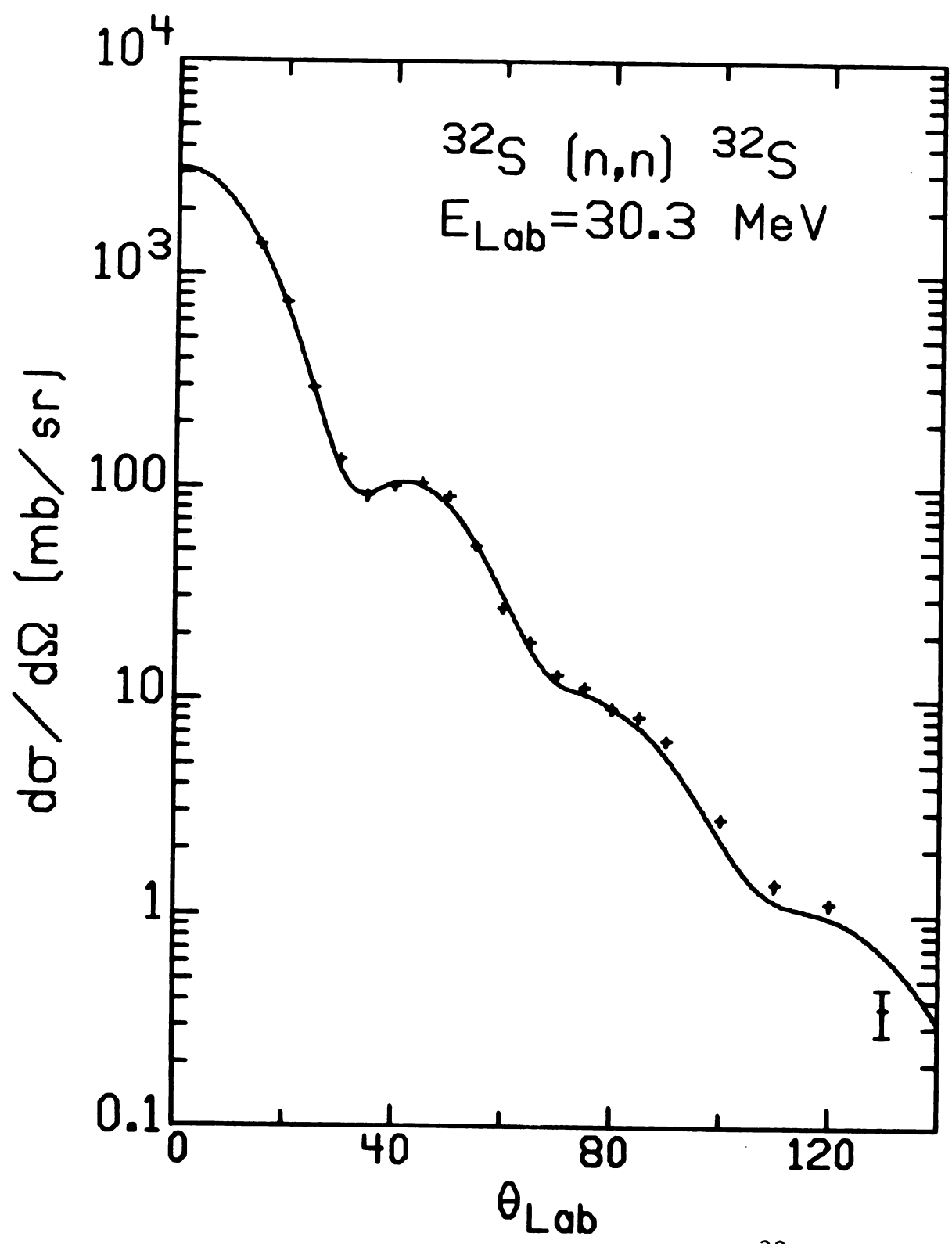


Figure 30. Laboratory Cross Section, <sup>32</sup>S, 30 MeV

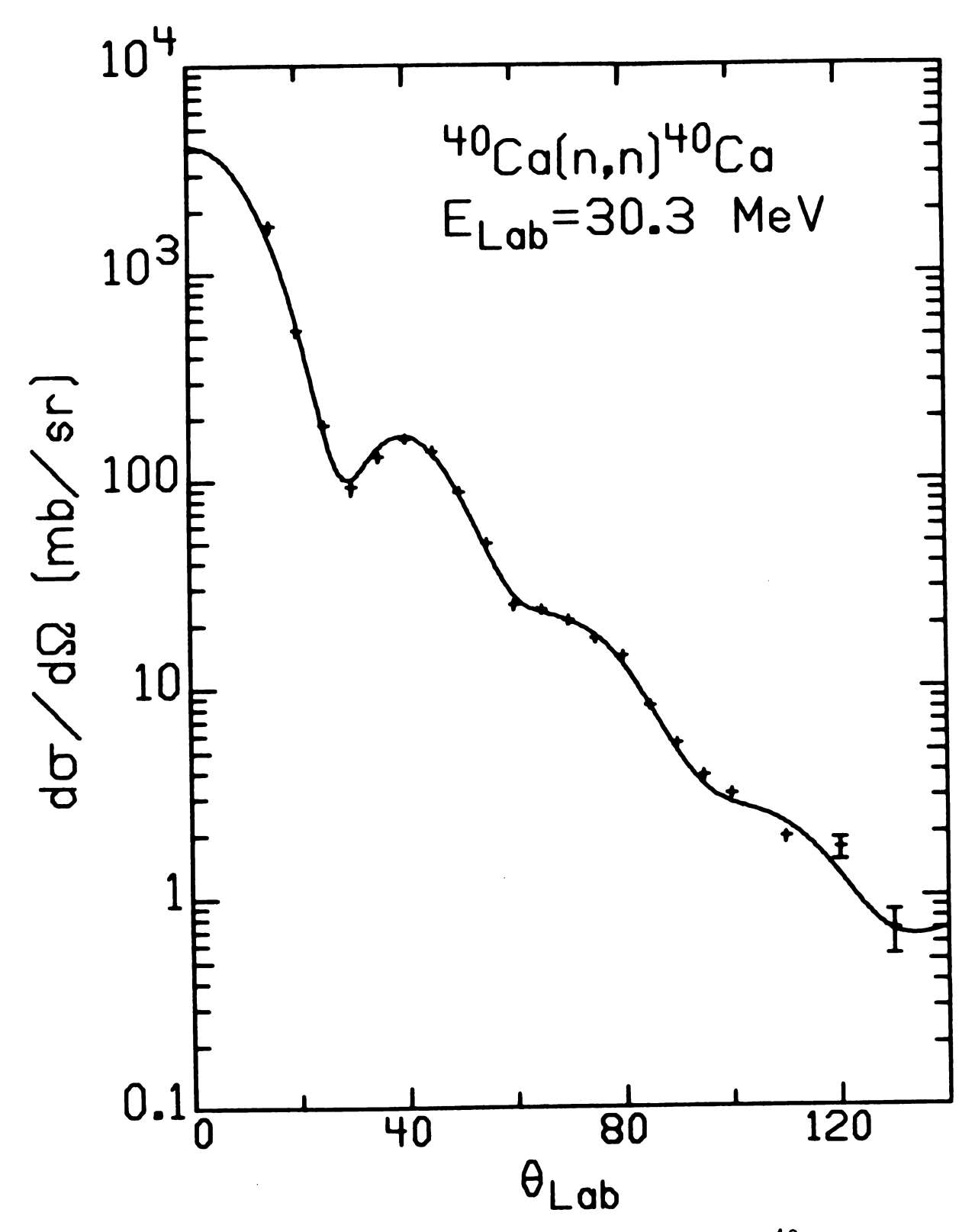


Figure 31. Laboratory Cross Section,  $^{40}$ Ca, 30 MeV

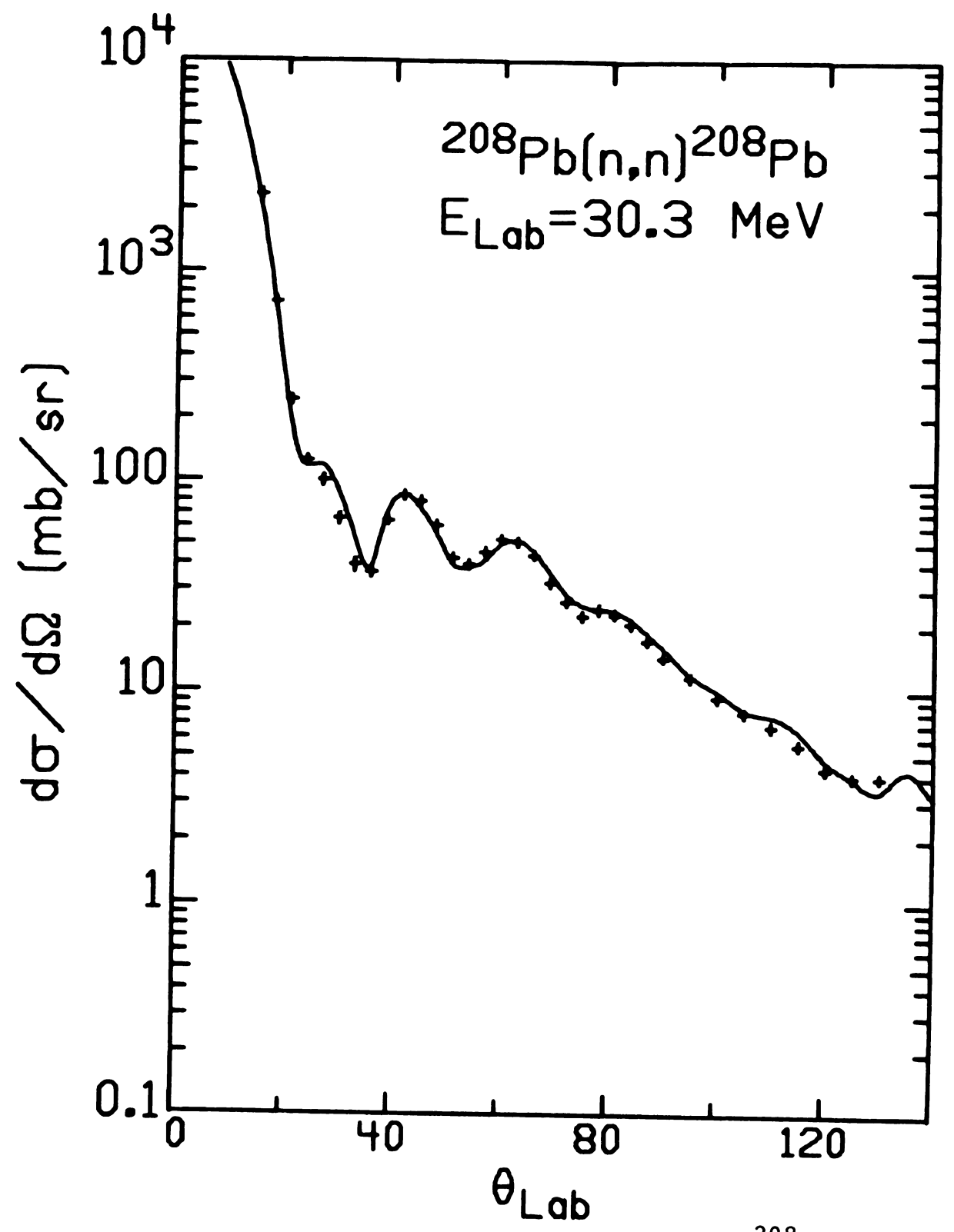


Figure 32. Laboratory Cross Section, <sup>208</sup>Pb, 30 MeV

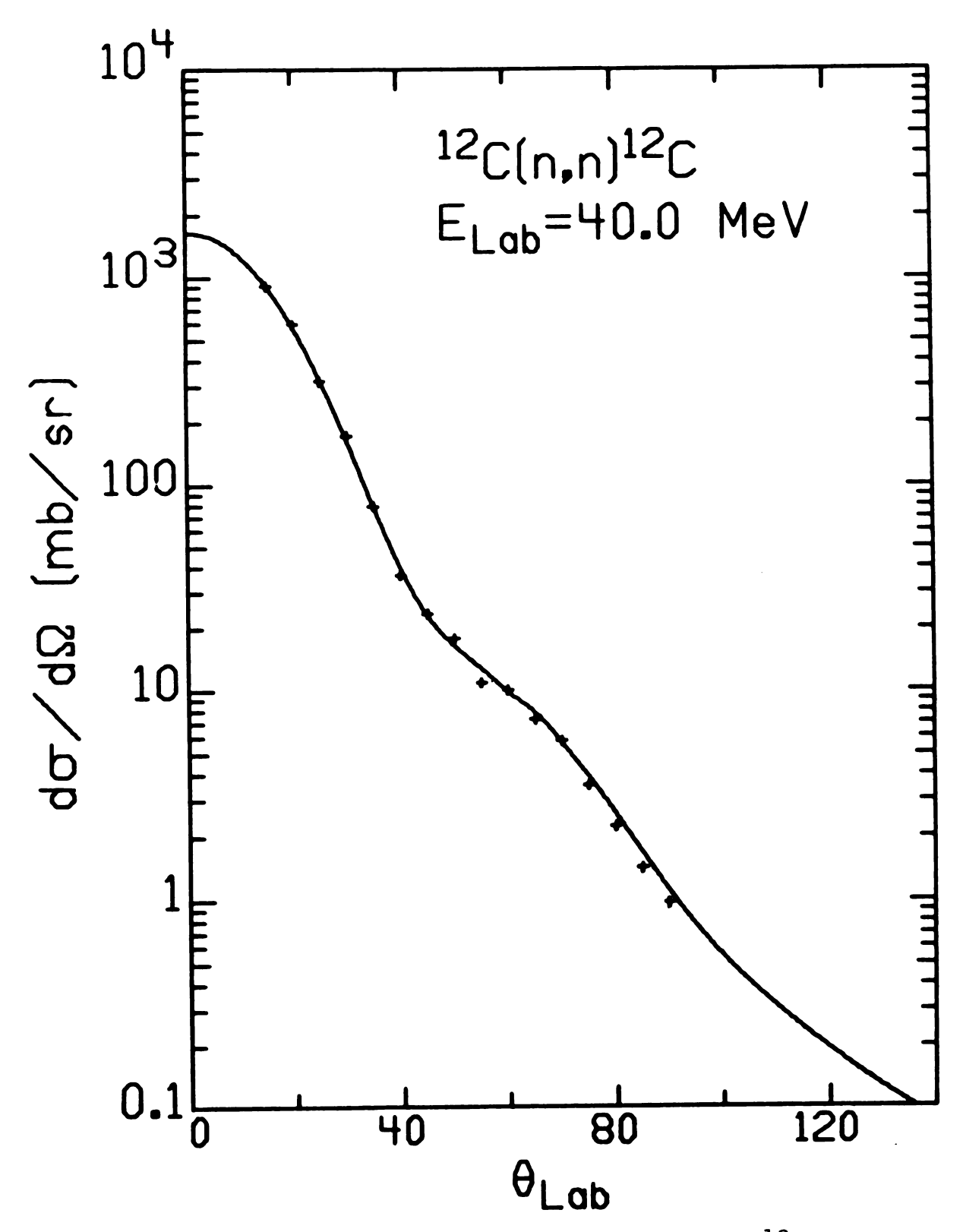


Figure 33. Laboratory Cross Section, <sup>12</sup>C, 40 MeV

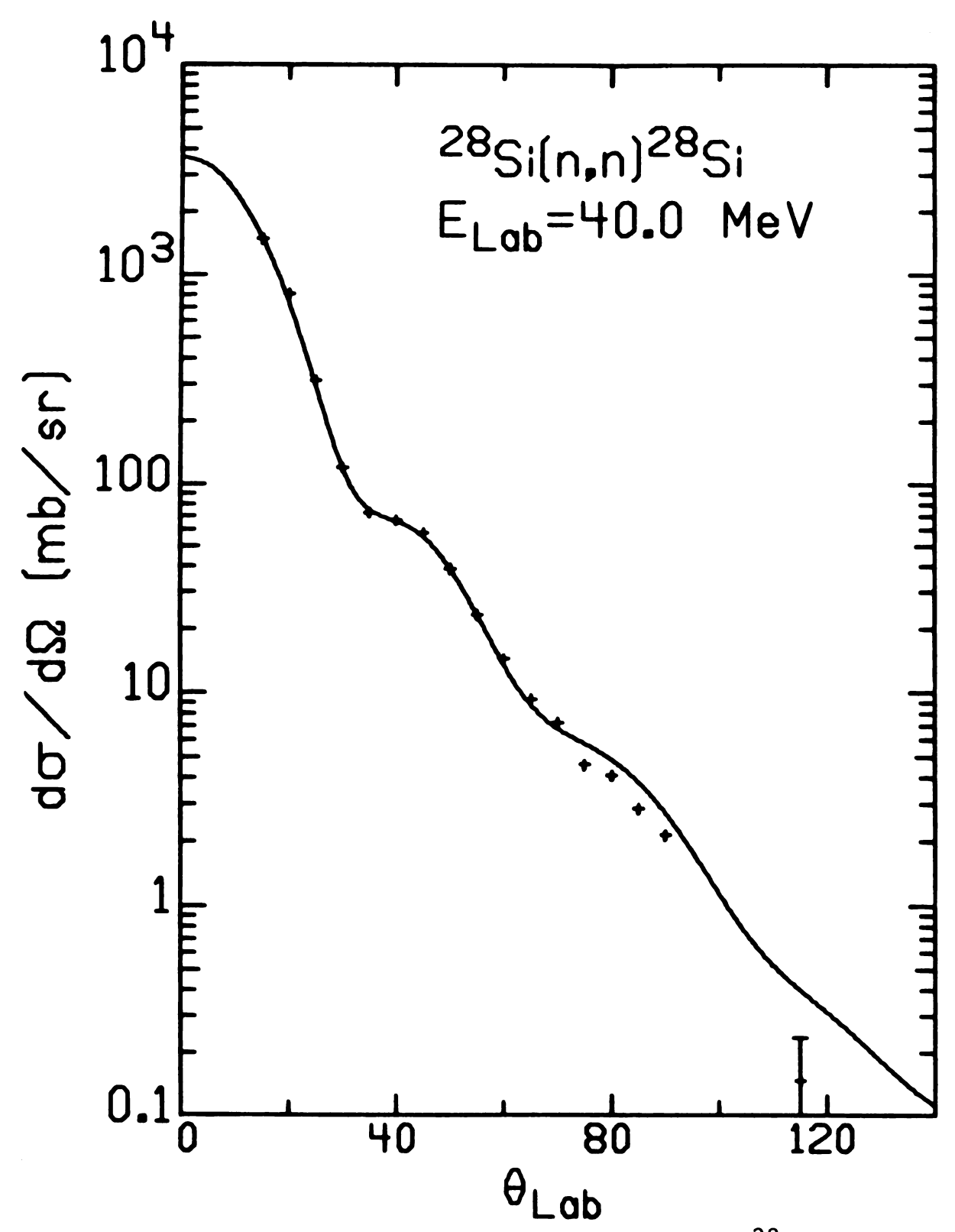


Figure 34. Laboratory Cross Section, <sup>28</sup>Si, 40 MeV

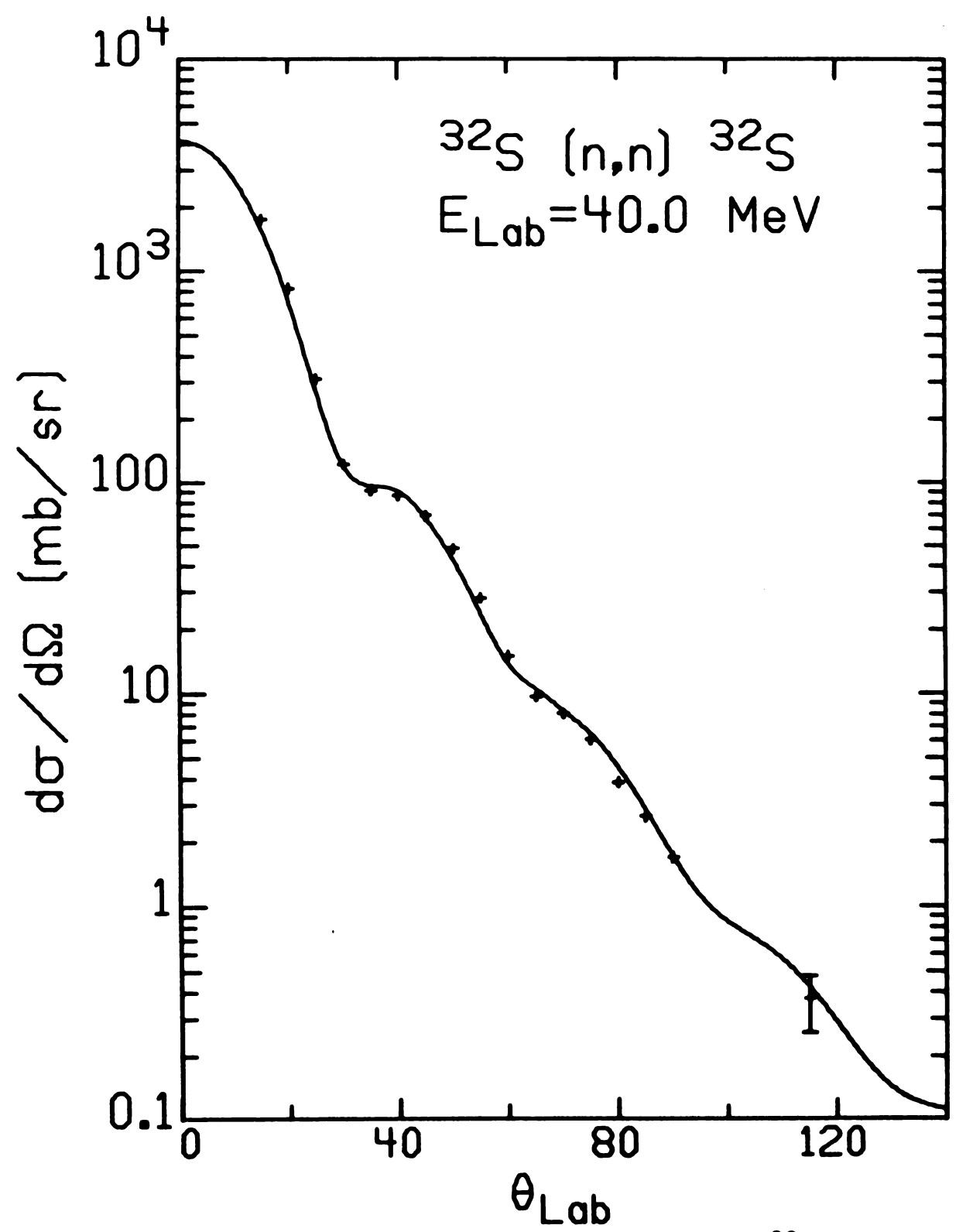


Figure 35. Laboratory Cross Section, <sup>32</sup>S, 40 MeV

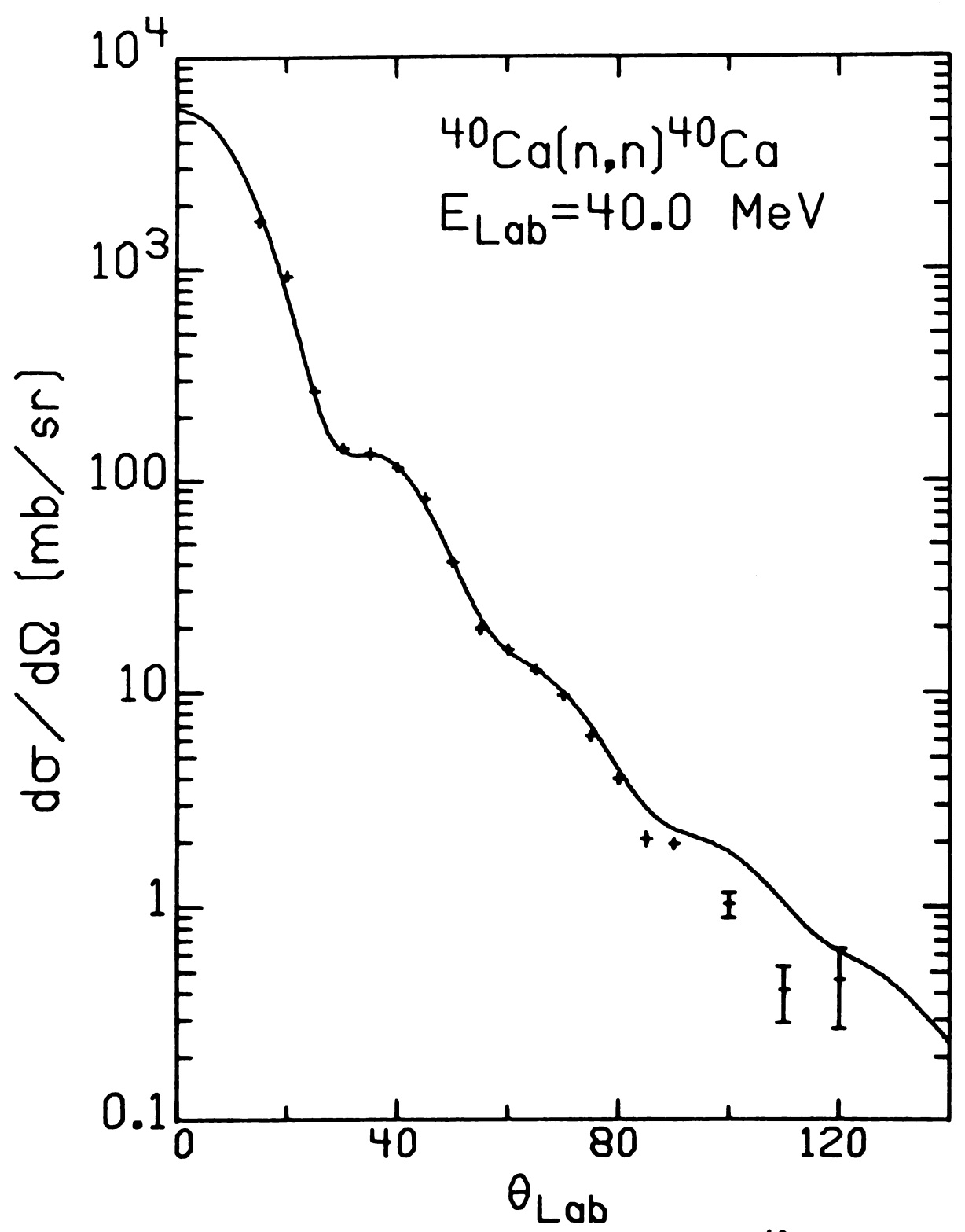


Figure 36. Laboratory Cross Section, 40 Ca, 40 MeV

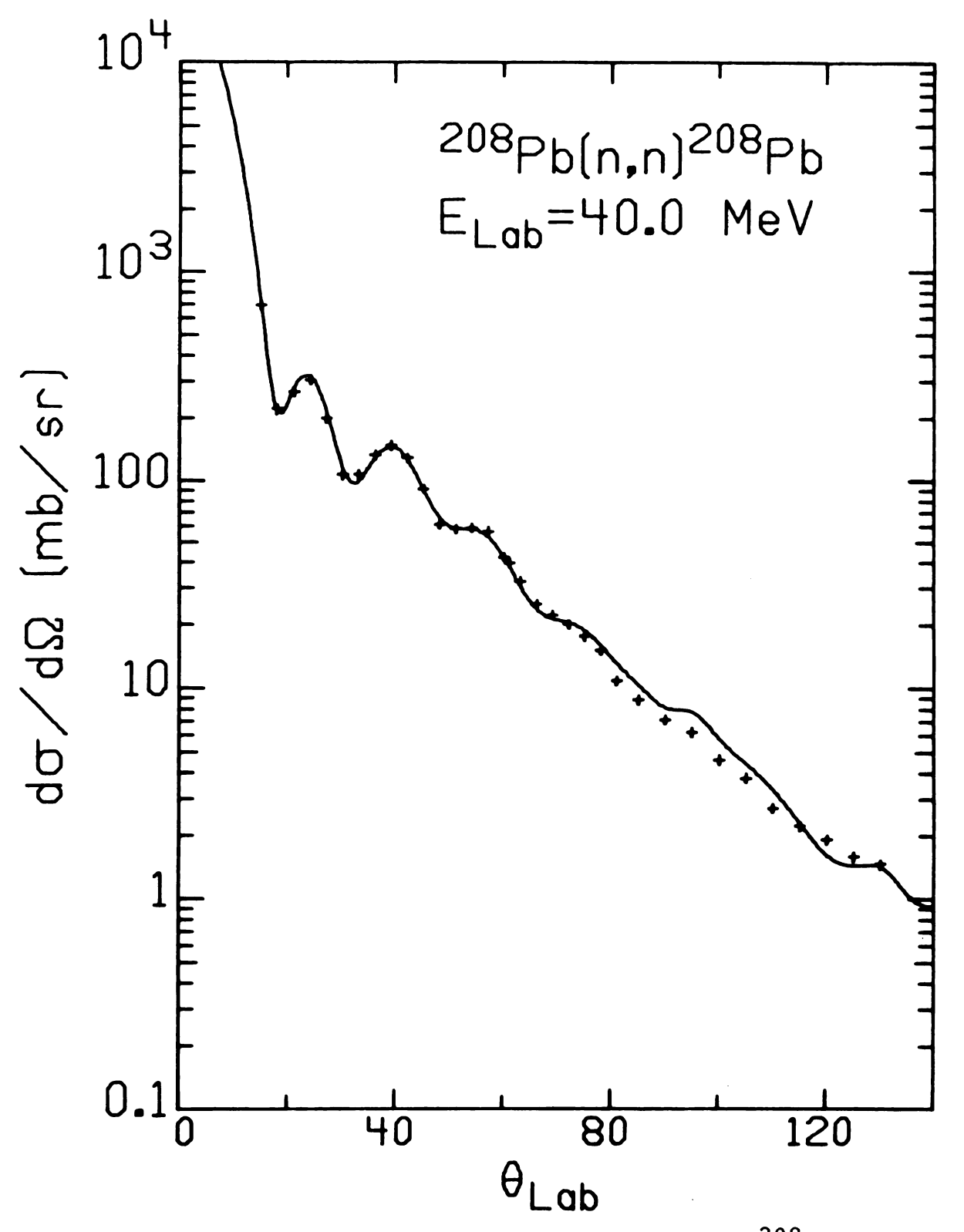


Figure 37. Laboratory Cross Section, 208<sub>Pb</sub>, 40 MeV

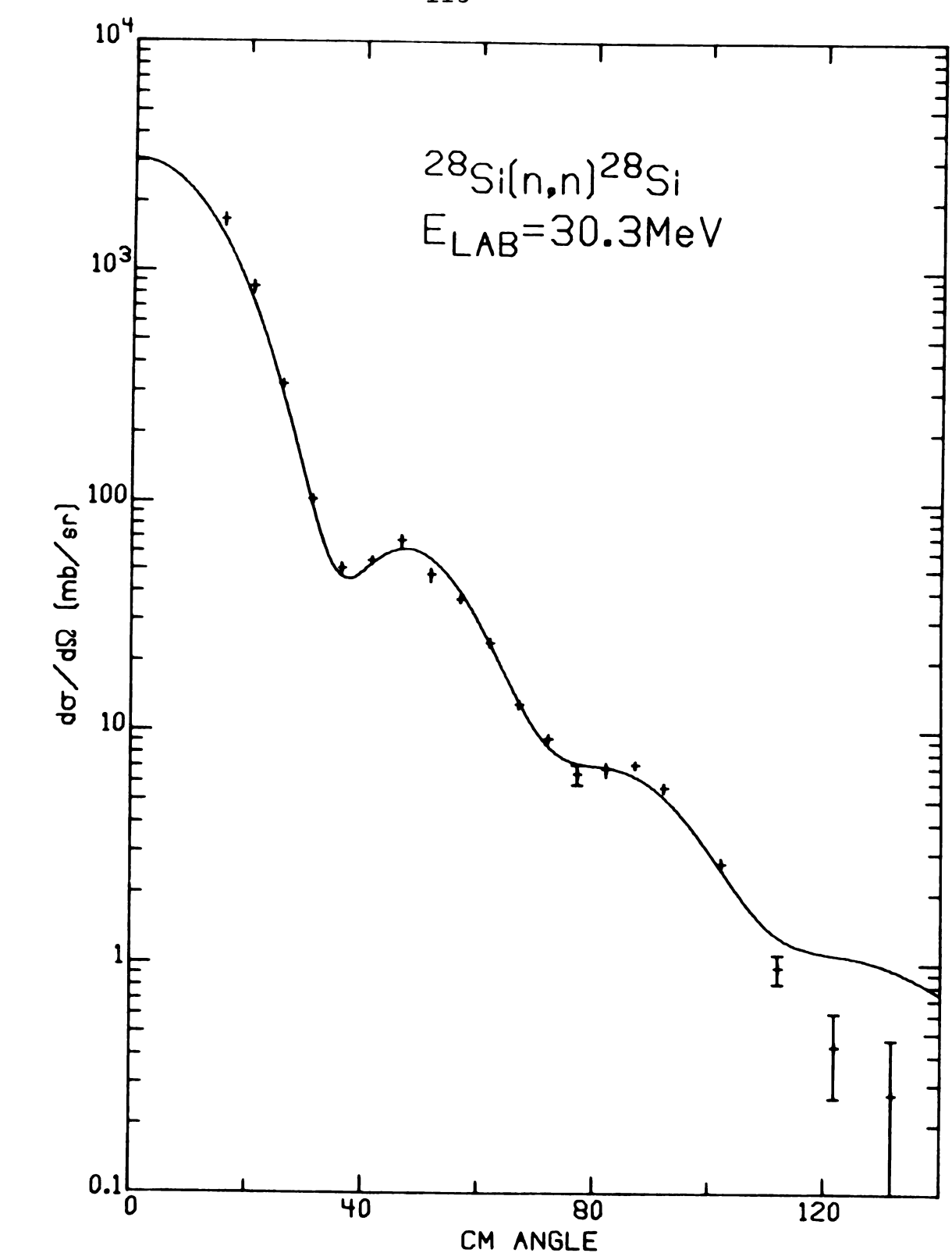


Figure 38. Center of Mass Cross Section, <sup>28</sup>Si, 30 MeV

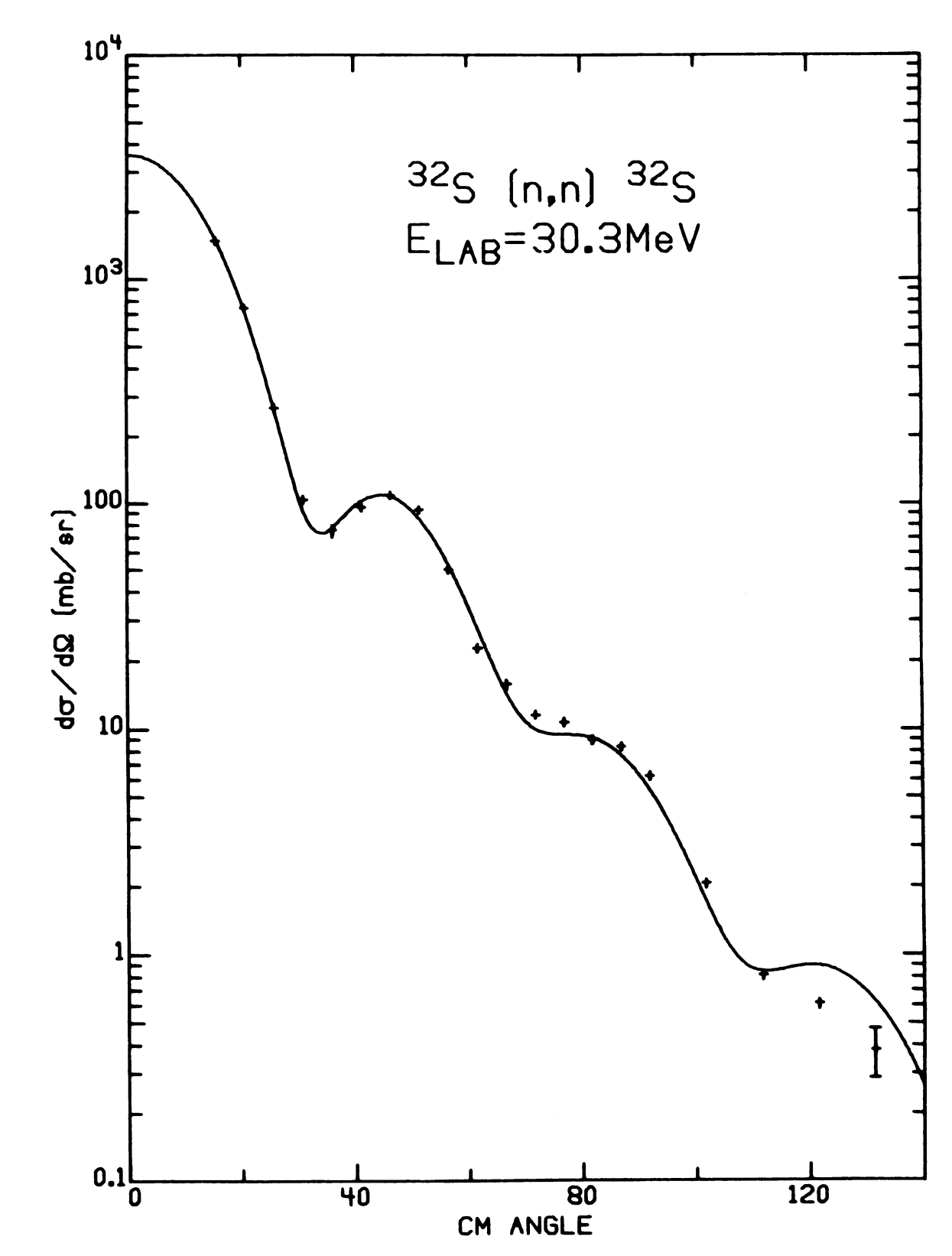


Figure 39. Center of Mass Cross Section,  $^{32}$ S, 30 MeV

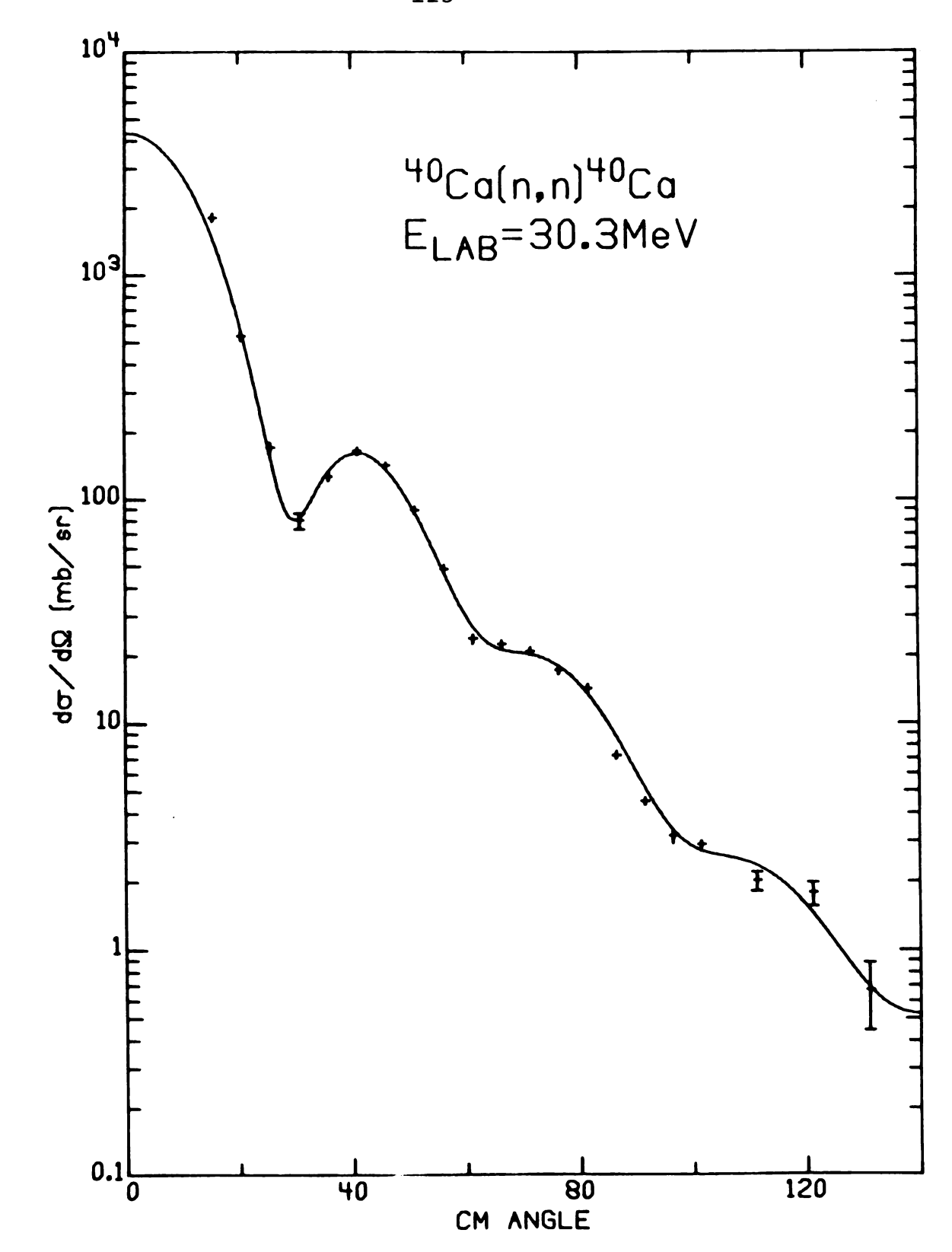


Figure 40. Center of Mass Cross Section, Best Fit  $^{40}\text{Ca}$ , 30 MeV

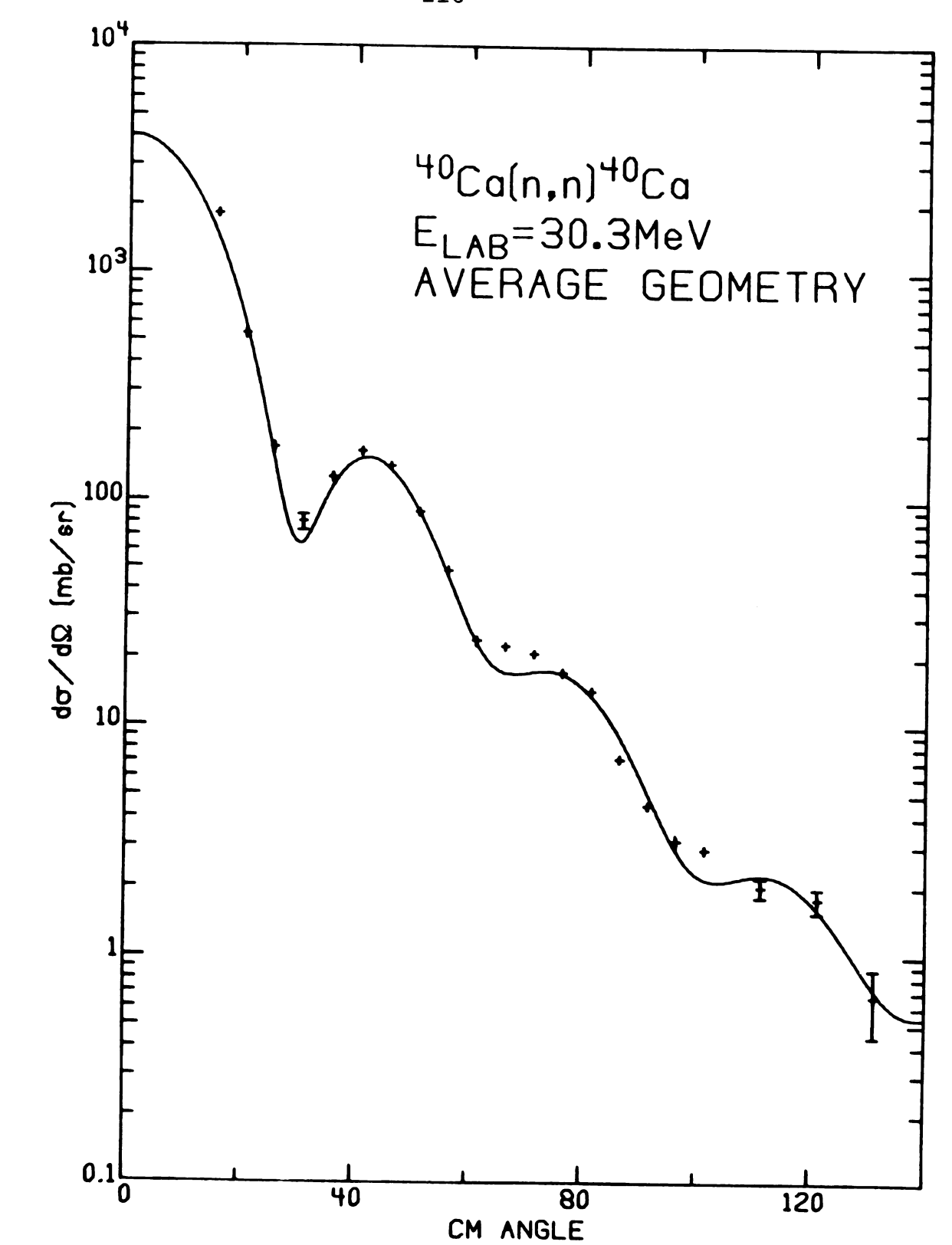


Figure 41. Center of Mass Cross Section, Fixed Geometry  $^{40}\text{Ca}$ , 30 MeV

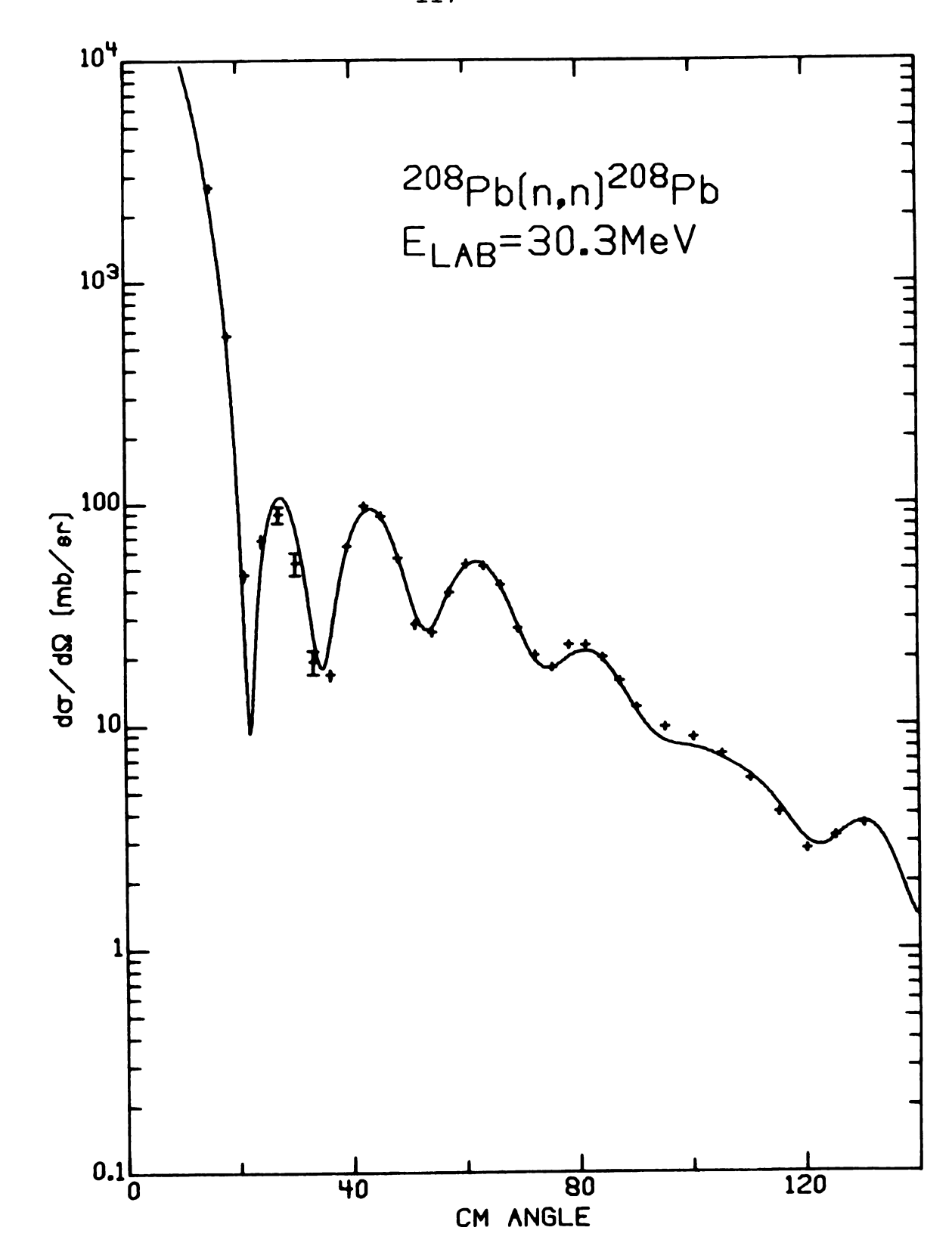


Figure 42. Center of Mass Cross Section, Best Fit 208<sub>Pb</sub>, 30 MeV

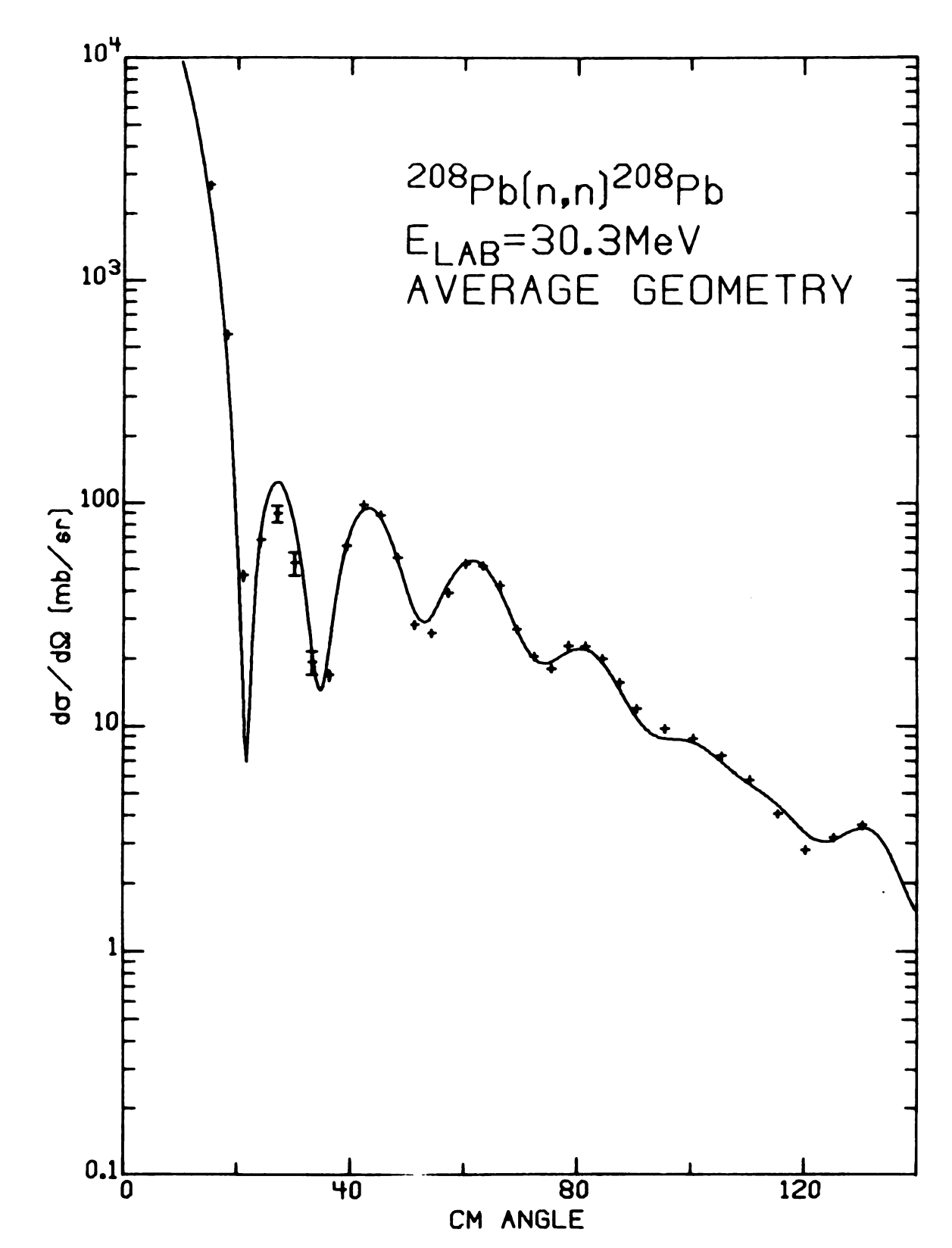


Figure 43. Center of Mass Cross Section, Fixed Geometry  $^{208}\mathrm{Pb},~30~\mathrm{MeV}$ 

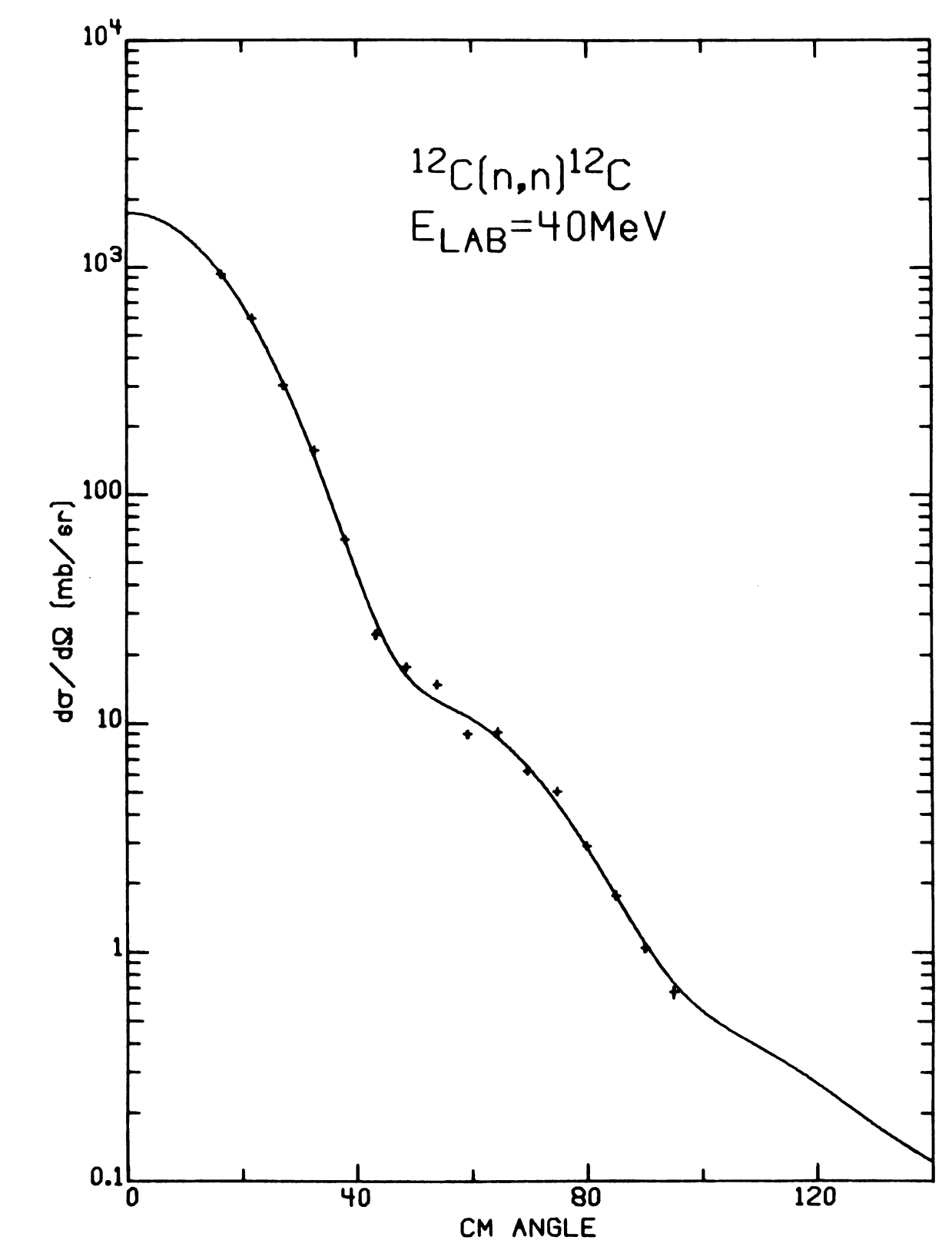


Figure 44. Center of Mass Cross Section, <sup>12</sup>C, 40 MeV

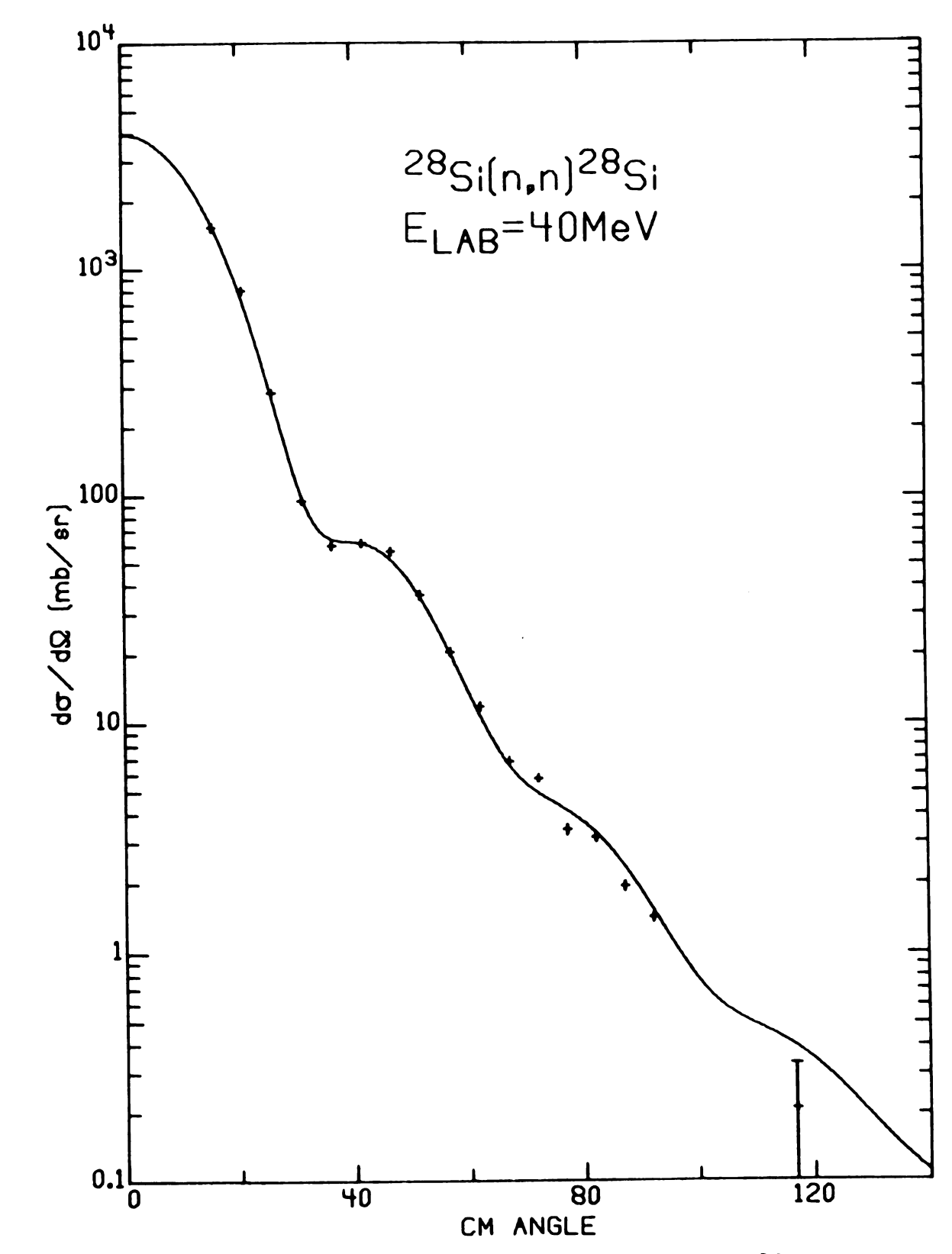


Figure 45. Center of Mass Cross Section, <sup>28</sup>Si, 40 MeV

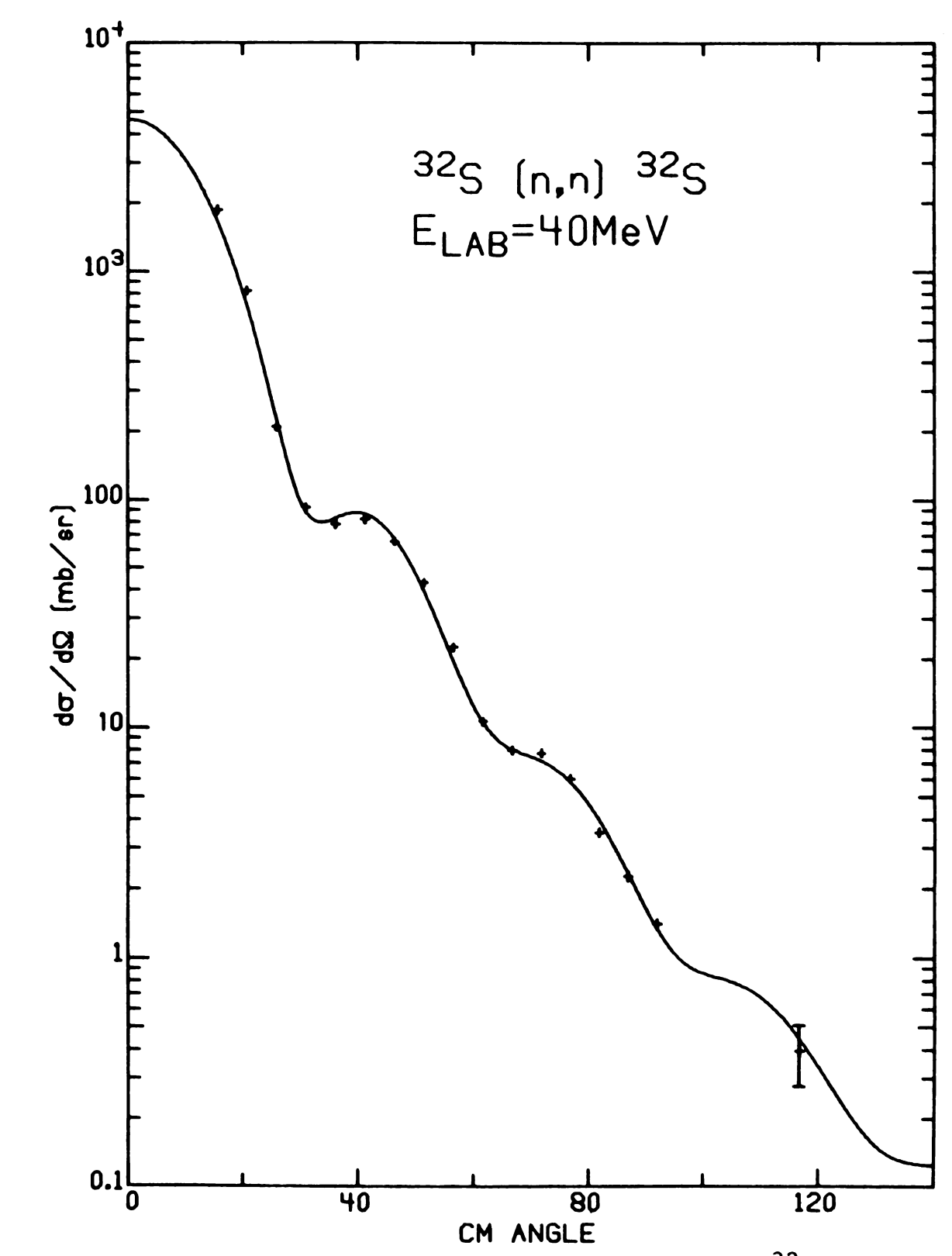


Figure 46. Center of Mass Cross Section, <sup>32</sup>S, 40 MeV

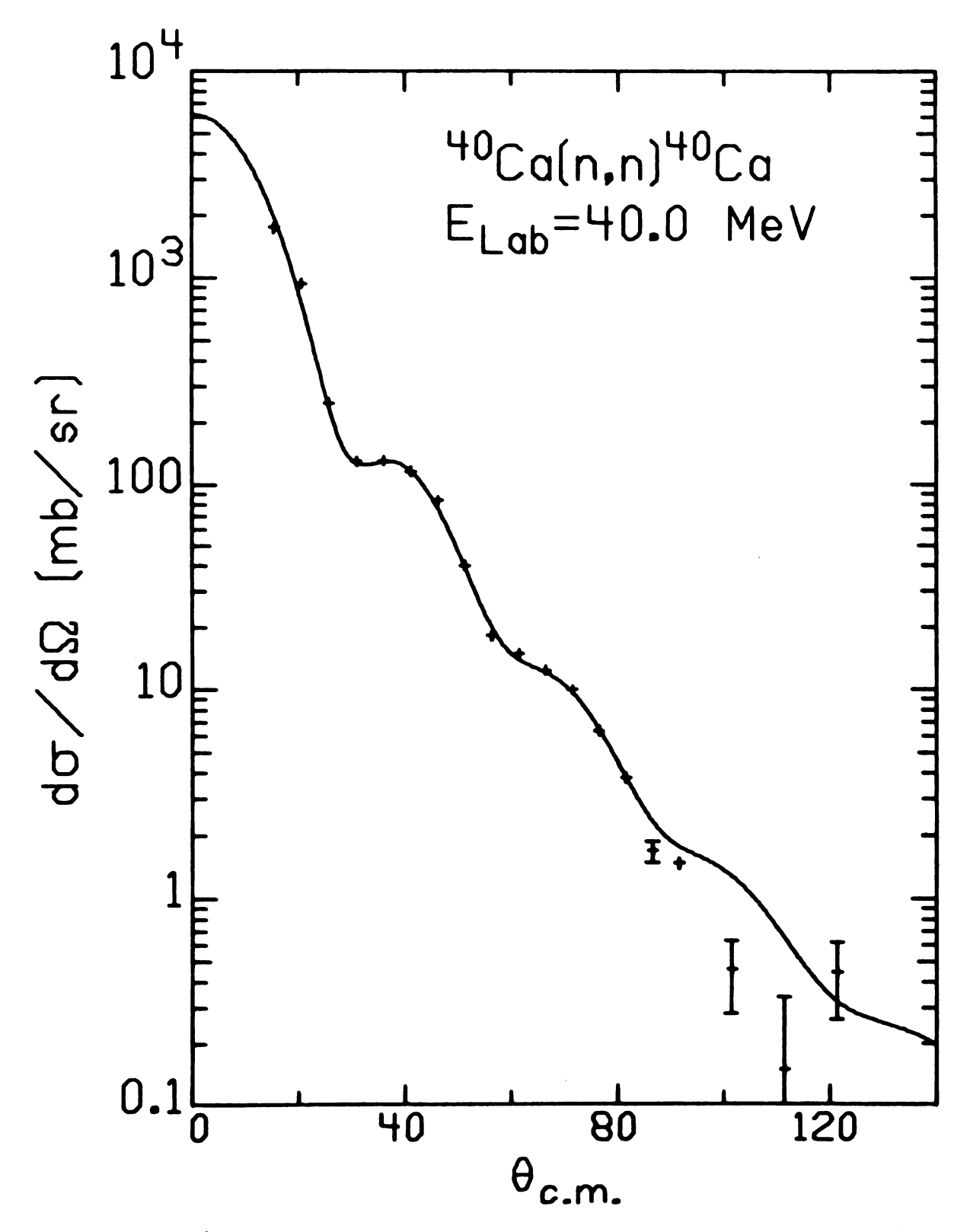


Figure 47. Center of Mass Cross Section, Best Fit  $^{40}$ Ca, 40 MeV

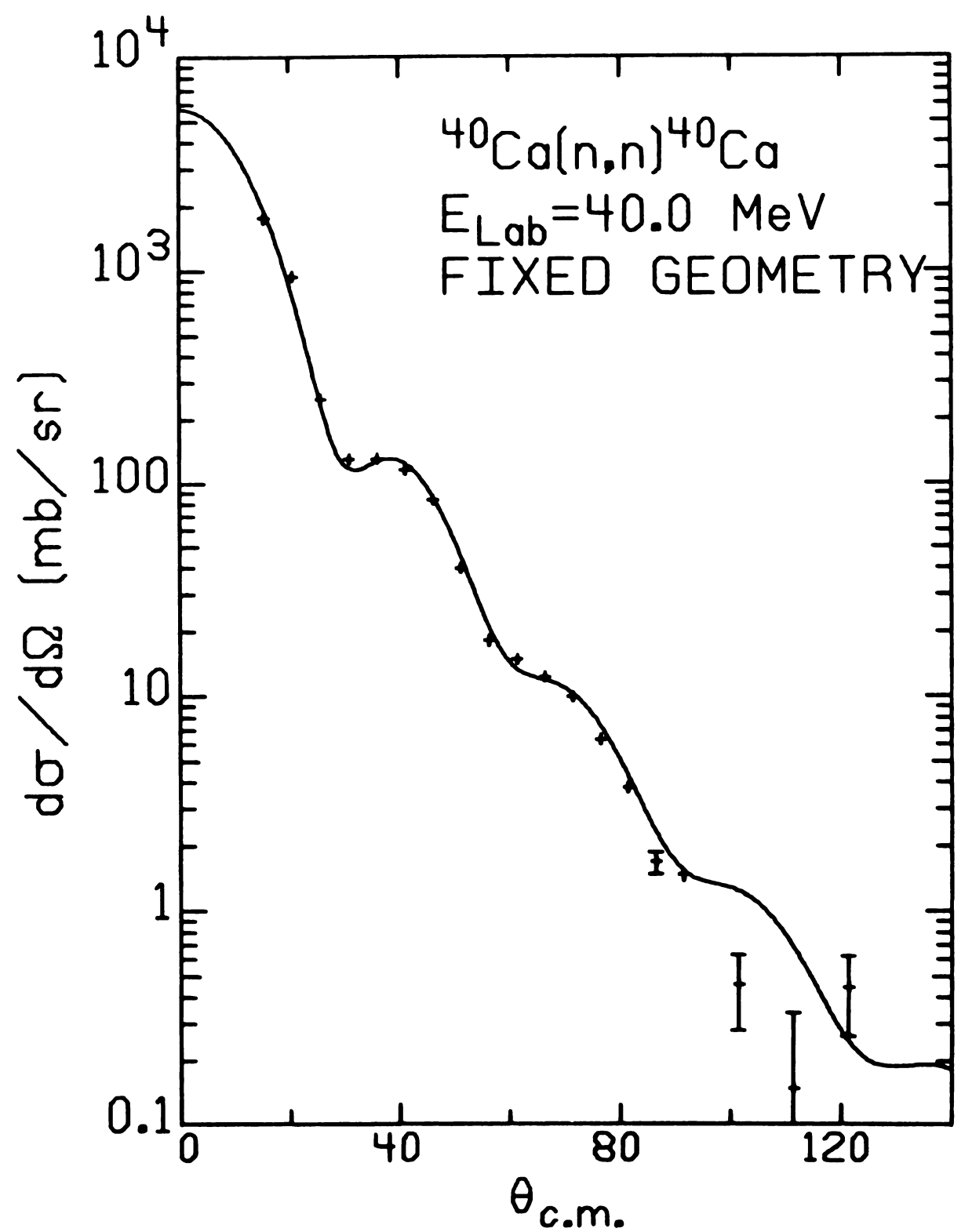


Figure 48. Center of Mass Cross Section, Fixed Geometry  $^{40}$ Ca, 40 MeV

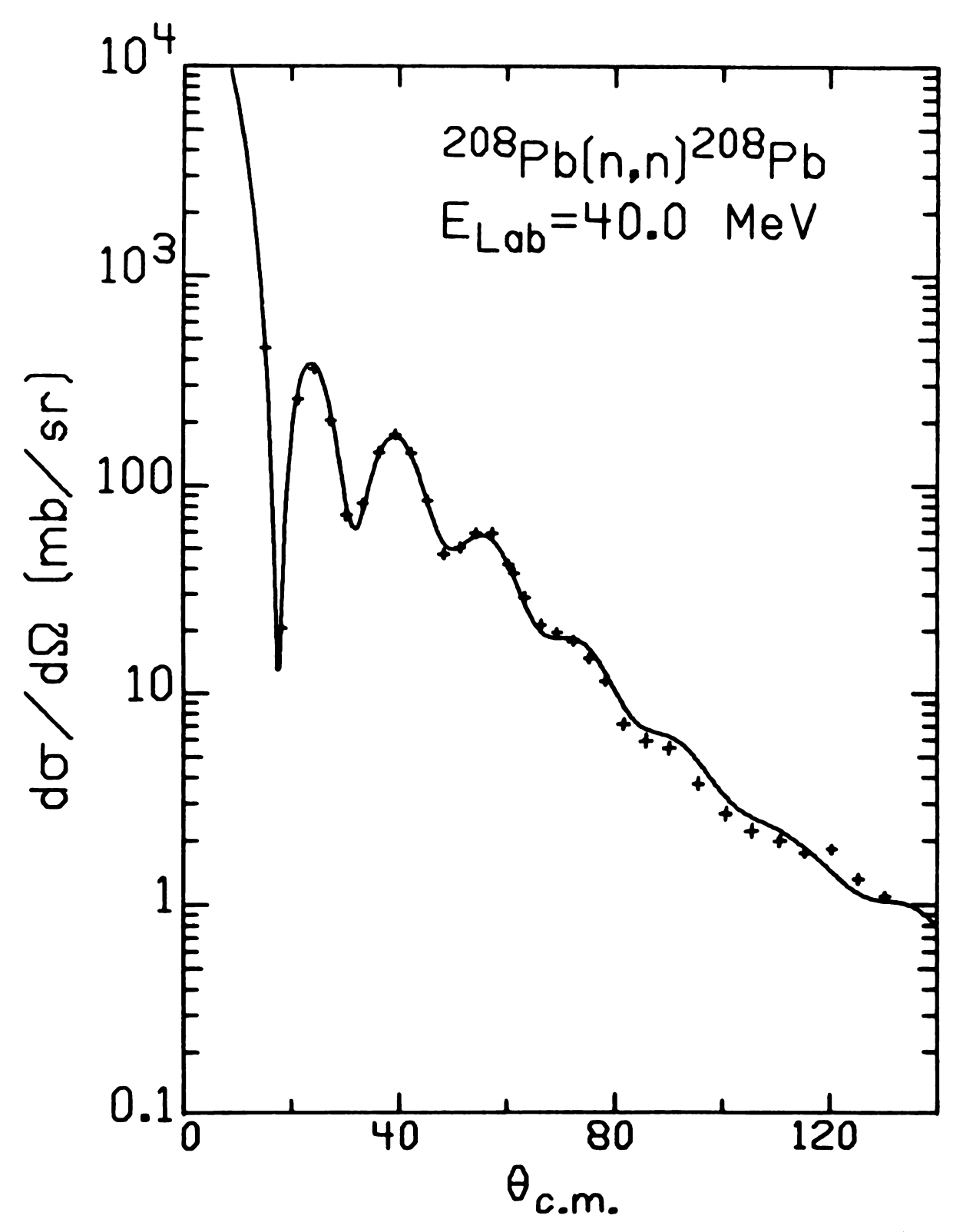


Figure 49. Center of Mass Cross Section, Best Fit  $^{208}\text{Pb}$ , 40 MeV

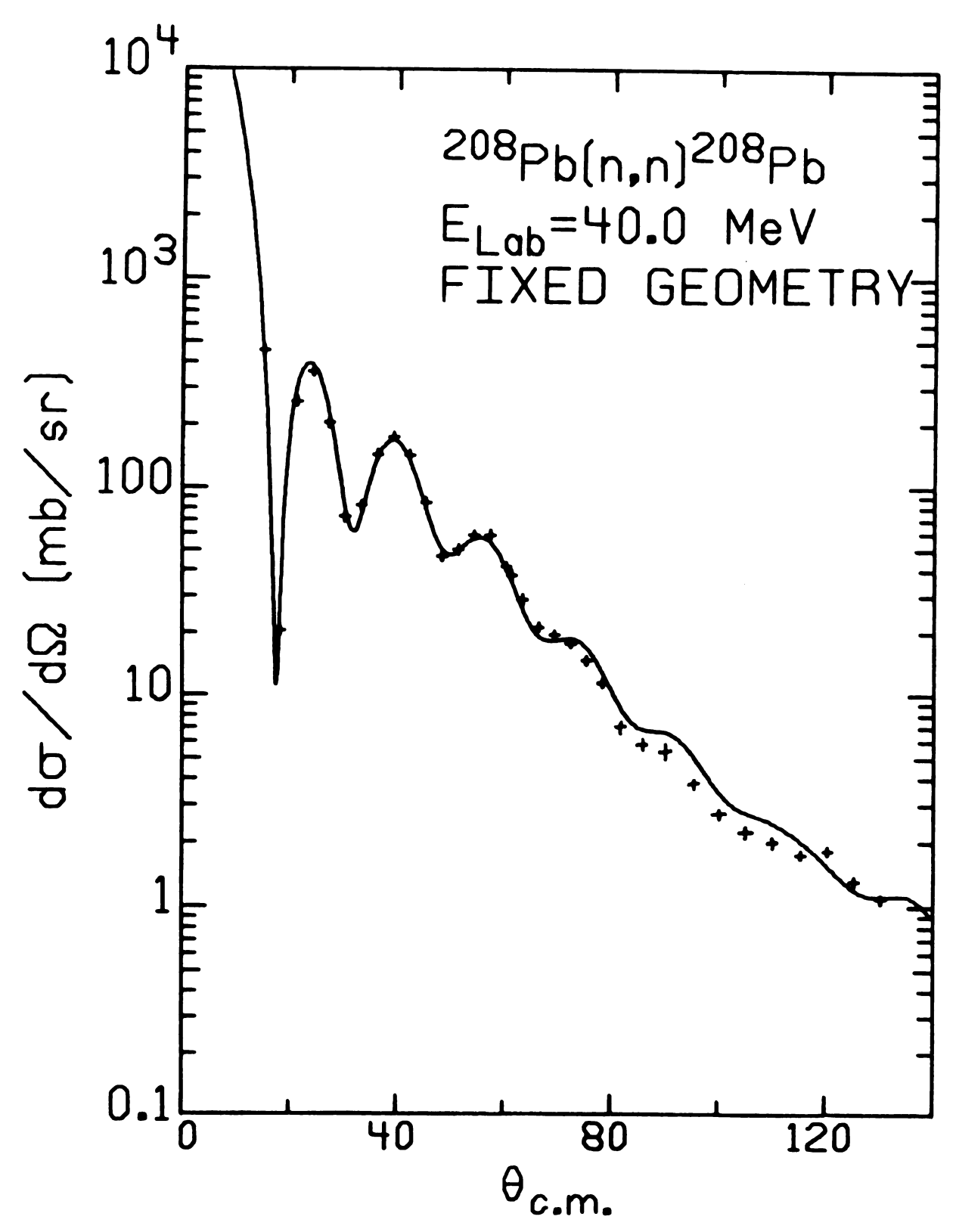


Figure 50. Center of Mass Cross Section, Fixed Geometry  $^{208}\text{Pb}$ , 40 MeV

Table 14. Measured Differential Cross Section

28SI(N,N) 30.3 MEV

UNCONNECTED LAEGRATORY			CORRECTED CENTER-OF-MASS		
ANGLE (DEG)	DIFFERENTIAL CROSS-SECTION (MB/SR)	RELATIVE ERROR (MB/Sh)	ANGLE (DEG)	DIFFERENTIAL CROSS-SECTION (NB/SR)	RELATIVE ERROR (MB/SR)
150.0 15	.1370E 04 .7191E 03 .3279E 03 .6051E 02 .5987E 02 .6110E 02 .4813E 02 .3913E 02 .39735E 02 .1454E 02 .1454E 01 .1017E 01 .7560E 01 .7560E 01 .3630E 01 .1720E 01 .1030E 01	.959E 02 .503E 01 .432E 01 .446E 01 .180E 01 .180E 01 .234E 00 .534E 00 .536E 00 .341E 00 .354E 00 .355E 00 .355E 00 .155E 00	15.55 20.596 21.002 31.00 336.371 46.51 561.84 556.84 662.00 87.77.887.10 92.10 121.80 131.60	.1664E 04 .8477E 033 .1016E 022 .1016E 022 .5443E 022 .5443E 022 .66916E 022 .12841E 01 .6797E 01 .7081E 01 .7081E 001 .7081E 001 .7082E 000 .4353E 000	.966E 02 .577E 01 .454E 01 .454E 01 .2088E 01 .286E 001 .236E 001 .577E 000 .377E 000 .377E 000 .3259E 000 .3259E 000

325(N,N) 30.3 MEV

UNCOHRI LAFORA	ECTED TORY		COHRECT CENTER-	ED OF-MASS	
ANGLE (DEG)	DIFFERENTIAL CROSS-SECTION (MB/SR)	RELATIVE ERROR (ME/SR)	ANGLE (DEG)	DIFFERENTIAL CHOSS-SECTION (ME/SIA)	RELATIVE ERHOR (ME/SH)
150.000.000.000.000.000.000.000.000.000.	.1370E 04 .7296E 03 .2923E 03 .1339E 03 .9060E 03 .1005E 02 .1035E 02 .5238E 02 .5238E 02 .1841E 02 .1284E 02 .1117E 01 .8150E 01 .8150E 01 .2750E 01 .2750E 01 .3620E 00	260E 02 7304E 01 .375E 01 .6070E 01 .243E 01 .243E 01 .153E 00 .1099E 00 .4499E 00 .4499E 00 .4499E 00 .4495E 00 .4495E 00 .4495E 00 .4495E 00 .495E 00 .495E 00	15.48 484937002233341.561950.233341.561.6950.8866001111.866001211.4660013111.4660013111.4660013111111111111111111111111111111111	.1478E 04 .7409E 03 .2665E 03 .1033EE 02 .10538E 02 .95538E 02 .9581E 02 .9268E 02 .5018E 02 .1566E 02 .1144E 02 .1062E 01 .8892E 01 .8267E 01 .8267E 01 .8267E 01 .831E 00 .7995E 00 .3794E	290E 02 1092E 01 1092E 01 1092E 01 1092E 01 1092E 01 108E 01 108E 01 111E 01 111E 00 111E 00

Table 14. (cont'd)

40CA(N,N) 30.3 MEV

UNCOHRI LAEGRA:			CORRECT CENTER-	'ED OF-Mass	
ANGLE (DEG)	DIFFERENTIAL CROSS-SECTION (MB/SK)	RELATIVE ERROR (MB/SH)	ANGLE (DEG)	DIFFERENTIAL CROSS-SECTION (MB/Sh)	RELATIVE EKROR (MF/SK)
1223334455667778899500000000000000000000000000000000	.1684E 04 .5307E 03 .1846E 02 .1846E 03 .9276E 03 .1566E 03 .1371E 02 .2443E 02 .2343E 02 .2443E 01 .2405E 01 .53750E 01 .53750E 01 .1680E 01 .1680E 00 .1680E 00 .1680E 01	.115E 03 .318E 02 .770E 02 .770E 01 .637E 01 .476E 01 .357E 01 .281E 01 .136E 00 .751E 00 .751E 00 .548E 00 .548E 00 .145E 00 .145E 00 .126E 00 .126E 00 .126E 00 .120E 00 .120E 00	150.5666.5429504478950.333466.12950447886.44980011.31.31.31.31.31.31.31.31.31.31.31.31.3	.1805E 04 .5361E 03 .1702E 03 .8002E 03 .1638E 03 .1418E 02 .2356E 02 .2227E 02 .2227E 02 .1711E 02 .1415E 01 .4147E 01 .4147E 01 .2875E 01 .1957E 01 .1957E 01	.116E 03 .323E 02 .777E 01 .651E 01 .500E 01 .381E 01 .298E 00 .779E 00 .779E 00 .779E 00 .299E 00 .1592E 00 .1292E 00 .1293E 00 .1293E 00 .1293E 00

Table 14. (cont'd) 208PB(N,N) 30.3 MEV

### UNCORRECTED LABORATORY

			0223	0	
ANGLE (DEG)	DIFFERENTIAL CROSS-SECTION (MB/SR)	RELATIVE ERROR (MB/SR)	ANGLE (DEG)	DIFFERENTIAL CROSS-SECTION (MB/SR)	RELATIVE ERROR (ME/SR)
1122223333444555566667777888899050000000000000000000000000000	043333222222222222222222222222222222222	8100E 001 8120E 000 8120E 000	15.1234 15.1234 15.124 167.1234 167.12	2685EE 002 2685EE 002 2685EE 002 2685EE 002 2685EE 002 2795EE 002 2895EE 002 2975EE 002 2975EE 002 2975EE 002 2975EE 002 2975EE 001 201 201 201 201 201 201 201	022 034 045 057 057 057 057 057 057 057 05

Table 14. (cont'd) 12C(N,N) 40.0 MEV

UN	CORRECTED	
LA	ECHATORY	

#### CORRECTED CENTER-CF-MASS

ANGLE (DEG)	DIFFERENTIAL CHOSS-SECTION (ME/SR)	RELATIVE ERROR (ME/SR)	ANGLE (DEG)	DIFFEHENTIAL CROSS-SECTION (ME/SR)	RELATIVE ERHOR (ME/SR)
15000000000000000000000000000000000000	.9057E 03 .5923E 03 .3163E 03 .7832E 02 .3604E 02 .3604E 02 .1765E 02 .1074E 01 .7140E 01 .5660E 01 .2210E 01 .1400E 01 .2400E 01 .3700E-01	.172E 02 .829E 01 .411E 01 .258E 01 .180E 01 .123E 00 .547E 00 .316E 00 .171E 00 .130E 00 .751E-01 .632E-01 .129E-01	16.30 371 16.30 17.10 17.20 17	.9283E 03 .5937E 03 .3017E 03 .3017E 02 .24480E 02 .1452E 02 .1468E 01 .8858E 01 .9051E 01 .4957E 01 .2857E 01 .1732E 01 .2857E 01	.193E 02 .193E 02 .525E 01 .205E 01 .205E 01 .134E 01 .809E 00 .368E 00 .334E 00 .191E 00 .803E-01 .658E-01

#### 28SI(N,N) 40.0 MEV

## UNCORRECTED LAFORATORY

ANGLE (DEG)	DIFFERENTIAL CROSS-SECTION (ME/SR)	RELATIVE ERROR (MB/SR)	ANGLE (DEG)	DIFFERENTIAL CROSS-SECTION (MB/SR)	RELATIVE ERROR (MB/SR)
15000000000000000000000000000000000000	.1473E 04 .8004E 03 .3106E 03 .1187E 02 .6569E 02 .5732E 02 .5732E 02 .2298E 02 .1418E 02 .9180E 01 .71523E 01 .4523E 01 .2805E 01 .2110E 01	.648E 02 .184E 02 .621E 01 .285E 01 .215E 01 .171E 01 .195E 01 .180E 00 .525E 00 .248E 00 .192E 00 .148E 00 .148E 00	15.79 25.79 25.67 25.67 25.67 25.67 25.67 25.67 25.67 25.67 25.67 27 27 27 27 27 27 28 27 28 27 28 27 28 29 29 29 29 29 29 29 29 29 29 29 29 29	.1536E 04 .802E 03 .2830E 02 .9474E 02 .6124E 02 .5618E 02 .3619E 02 .1169E 01 .56739E 01 .56734E 01 .3374E 01 .3111E 01 .1909E 01 .1401E 01	.663E 02 .201E 01 .321E 01 .321E 01 .185E 01 .184E 01 .845E 00 .552E 00 .278E 00 .278E 00 .230E 00 .157E 00 .981E-01

Table 14. (cont'd) 32S(N,N) 40.0 MEV

UNCORRECTED LABORATORY			CORRECTED CENTER-OF-MASS		
ANGLE (DEG)	DIFFERENTIAL CROSS-SECTION (MB/SR)	RELATIVE ERROR (ME/SR)	ANGLE (DEG)	CIFFERENTIAL CROSS-SECTION (ME/SR)	RELATIVE ERROR (MB/SR)
150.0 205.0 350.0 450.0 550.0 670.0 850.0 115.0	.1735E 04 .8183E 03 .3074E 03 .1202E 03 .9031E 02 .8550E 02 .6574E 02 .4762E 02 .27781E 02 .1480E 01 .7930E 01 .7980E 01 .3770E 01 .3600E 01 .3650E 00	.694E 02 .237E 01 .409E 01 .325E 01 .3265E 01 .2138E 00 .2138E 00 .548E 00 .167E 00 .132E 00 .167E 00 .132E 00 .169E 00	15.49 46.79 15.49 15.69 10.22 15.69 116.77 116.70 116.70	.1858E 04 .8194E 03 .2074E 02 .7778E 02 .7778E 02 .8189E 02 .6520E 02 .4263E 02 .10542E 01 .7651E 01 .7651E 01 .5933E 01 .3458E 01 .391E 01 .3902E 00	.713E 02 .251E 02 .103E 01 .342E 01 .280E 01 .225E 01 .148E 00 .5786E 00 .214E 00 .178E 00 .138E 00 .116E 00 .843E-01

40CA(N,N) 40.0 MEV

UNCORRECTED LAFGRATORY

			OBIVEDIA	OI -IIADD	
ANGLE (DEG)	DIFFERENTIAL CROSS-SECTION (MB/SH)	RELATIVE ERROR (MB/SR)	ANGLE (DEG)	DIFFERENTIAL CROSS-SECTION (MB/SR)	RELATIVE ERRCR (ME/SR)
150.00.00.00.00.00.00.00.00.00.00.00.00.0	.1676E 04 .2643E 03 .1413E 03 .1413E 02 .1413E 02 .1148E 02 .1150E 02 .19563E 01 .19563E 01 .19563E 01 .19560E 01 .19500E 01 .19600E 00 .19600E 00 .19600E 00 .19600E 00	.805E 02 .3740E 01 .3746E 01 .3796E 01 .3794E 00 .3794E 00 .4839E 00 .4839E 00 .4374E 00 .1152E 00 .1152E 00 .1437E	15.39 15.45 15.67 15.67 10.10	.1751E 04 .93475E 03 .2475E 03 .1295E 03 .1355E 02 .1355E 02 .13598E 02 .1472E 02 .1478E 01 .3746E 01 .3746E 01 .3746E 00 .1465E 00 .1472E 00 .1473E 00	.821E 02 .363E 01 .425E 01 .396E 01 .396E 01 .186E 01 .186E 00 .458E 00 .458E 00 .458E 00 .236EE 00 .178E 00 .144E 00 .141E 00 .187E

Table 14. (cont'd) 205PE(N,N) 40.0 MEV

UNCORRECTED LABORATORY

ANGLE (DEG)	DIFFERENTIAL CROSS-SECTION (MB/SR)	RELATIVE ERROR (ME/SR)	ANGLE (DEG)	DIFFERENTIAL Choss-Section (MB/Sh)	RELATIVE ERROR (ME/SH)
00000000000000000000000000000000000000	.666E 00333333333333333333333333333333333	222011092E 001 1092E 001 11079E 000 11079E 000 110	79002346789023345556678888999990000000001111111111122222222222	03233322 03233322 03233322 002333322 002333322 002333322 002333322 002333322 002333322 002333322 00233332 00233332 00233332 00233332 00233332 00233332 00233332 003332 003332 003332 003332 003332 003332 003332 003332 003332 003332 003332 003332 003332 003332 003332 003332 003332 003332 00	02222102220100000000000000000000000000

#### LIST OF REFERENCES

- Al 61 K. Alexander & F. Goulding, Nucl. Inst. Meth. 13, 244(1961).
- Au 70 N. Austern, "Direct Nuclear Reaction Theories", Wiley, N.Y. (1970).
- Be 69 F.D. Becchetti, Jr. & G.E. Greenlees, Phys. Rev., 182(1969)1190.
- Bh 77 R.K. Bhowmik, R.R. Doring, L.E. Young, Sam M. Austin, A. Galonsky & S.D. Schery, Nucl. Inst. Meth., 143 (1977) 63.
- Bl 66 L.N. Blumberg, E.E. Gross, A. van der Woude, & A. Zucker, Phys. Rev., 147(1966)812.
- Br 77 F.A. Brieva & J.R. Rook, Nucl. Phys. A291(1977)317.
- Br 78 F.A. Brieva & J.R. Rook, Nucl. Phys. A297(1978) 206.
- Ca 75 J.D. Carlson, C.D. Zafiratos, & D.A. Lind, Nucl. Phys. A249(1975)29.
- Do 74 R.R. Doering, Ph.D. Thesis, MSU, 1974.
- Fe 49 S. Fernback, R. Serber & T.B. Taylor, Phys. Rev. 75(1949)1352.
- Fe 76 J.C. Ferrer, et al., Phys. Lett. 62B(1976)399.
- Fe 77 J.C. Ferrer, J.D. Carlson and J. Rapaport, Nucl. Phys. A275(1977)325.
- Fe 54 H. Feshback, C.E. Portor, & V.F. Weisskopf, Phys. Rev. 96(1954)448.
- Fe 58a H. Feshback, Ann. Rev. Nucl. Sci., 8(1958)49.
- Fe 58b H. Feshback, Ann. Phys. 5(1958)357.
- Fe 62 H. Feshback, Ann. Phys. 19(1962)287.
- Ga 78 A. Galonsky, Private Communication.
- Ha 76 E.C. Hagen & P.C. Eklund, Rev. Sci. Instr. <u>47</u> (1976)1144.

- Ha 62 T. Hamada & D. Johnston, Nucl. Phys. 34(1962)382.
- Je 74 J. -P. Jeukenne, A. Lejeune, and C. Hahaux,
  Phys. Rev. C10(1974)1391.
- Je 76 J. -P. Jeukenne, A. Lejeune, and C. Mahaux, Phys. Lett. 62B(1976)256.
- Je 77 J. -P. Jeukenne, A. Lejeune, and C. Mahaux, Phys. Rev. C15(1977)10.
- Ki 70 W.E. Kinney, Nucl. Inst. Meth. 83(1970)15.
- Le 52 R.E. LeLevier & D.S. Saxon, Phys. Rev. 87(1952)40.
- Ma 79 C. Mahaux in "Microscopic Optical Potentials" edited by H.V. von Geramb p.1, Springer-Verlag, N.Y. (1979)
- Me 71 J.J.M. Menet, E.E. Gross, J.J. Malanify & A. Zucker, Phys. Rev. C4(1971)1114.
- Ne 70 J.W. Negele, Phys. Rev. C1(1970)1260.
- Pa 76 D.M. Patterson, R.R. Doering & Aaron Galonsky, Nucl. Phys. A263(1976)26.
- Pe 63 F.G. Perey, Phys. Rev. 131(1963)745.
- Pe 66 Written by F.G. Perey and Modified by R.M. Haybron.
- Pe 74 F.G. Perey in "Nuclear Spectroscopy and reactions, Part B" Edited by Joseph Cerny p. 137, Academic Press, N.Y.
- Pe 76 C.M. Perey and F.G. Perey, Atomic Data and Nuclear Data Tables 17(1976)1.
- Ra 77 J. Rapaport, J.D. Carlson, D. Bainum, T.S. Cheema, & R.W. Finlay, Nucl. Phys. <u>A286</u>(1977)232.
- Ra 78 J. Rapaport, T.S. Cheema, D. Bainum, R.W. Finlay, J.D. Carlson, Nucl. Phys. A296(1978)95.
- Ra 79 J. Rapaport, V. Kulkarni, R.W. Finlay, preprint.
- Ra 79 J. Rapaport, T.S. Cheema, D. Bainum, R.W. Finlay, & J.D. Carlson, Nucl. Phys. A313(1979)1.
- Ri 64 B.W. Ridley & J.F. Turner, Nucl. Phys. 58(1964)509.

St 65 P.H. Stelson and L. Grodzins, Nucl. Data  $\underline{1}$ (1965)29.

Va 71 W.T.H. van Oers, Phys. Rev. C3(1971)1550.

Va 74 W.T.H. van Oers et al., Phys. Rev. Cl0(1974)307.

